Charles University in Prague
Faculty of Mathematics and Physics

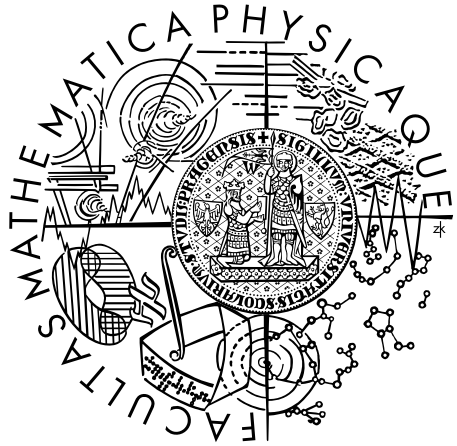

Numerical modeling of present-day mantle convection

Nicola Tosi

Prague, 2007

Numerical modeling of present-day mantle convection

Nicola Tosi

Ph.D. Thesis

Supervisor: Prof. Zdeněk Martinec

Charles University in Prague
Faculty of
Mathematics and Physics

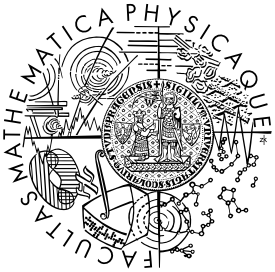

Department of Geophysics
V Holešovičkách 2
180 00 Praha 8
Czech Republic

GeoForschungsZentrum
Potsdam

GFZ
POTSDAM

Earth System Modeling
Telegrafenberg
14473 Potsdam
Germany

Contents

Summary

Since the establishment of the theory of plate tectonics in the late 1960s, mantle convection has been the mechanism accepted to explain the dynamics of the Earth's interior. Its theoretical understanding is largely based on the simple concept of convecting motion experienced by a fluid enclosed in an internally heated spherical shell whose boundaries are kept at different temperatures (*Rayleigh-Bénard convection*). Decay of radioactive isotopes provides the primary source for the internal heating of the mantle, while long-term secular cooling and heat from the core determine the temperature difference between its outer and inner boundaries. On geological time-scales, mantle material flows like a viscous fluid as a consequence of the buoyancy forces arising from thermal expansion.

To model this phenomenon, two complementary approaches are possible. On the one hand, one can solve self-consistently the equations of thermal convection, including parameters and employing physical relationships derived from mineral physics. Our understanding of mantle convection depends ultimately upon the success of such fully self-consistent dynamic models in explaining observable features of the flow. Although the rapid growth in available computer power allows us to construct increasingly complex and realistic models, they are presently unable to predict the actual convection pattern of the Earth. Nevertheless, they are extremely useful to investigate general characteristics of given physical systems. On the other hand, to permit comparison with specific observables associated with the flow, one can consider a more restricted problem. Instead of focusing on the time evolution of mantle flow, if we know *a priori* the temperature - and hence presumably the density - anomalies that drive the convection, we can try to build a snapshot of the present-day flow pattern, consistent with those anomalies, that can successfully predict the observables. Our work is largely motivated by the latter approach.

In Chapter 1 several fundamental concepts necessary to understand a mathematical model of present-day mantle convection are presented. In Chapter 2 we introduce the partial differential equations that we aim to solve. Then, we review the technique of the matrix propagator that, over the last twenty years, has been the principal mathematical tool upon which models of present-day mantle convection with radially symmetric viscosity distributions have been built. In Chapter 3 we describe in detail what we term the spectral finite element (SFE) method. After converting the classical differential form of the problem to an

equivalent integral form (*weak formulation*), we introduce a combined parameterization consisting of finite elements and spherical harmonics that allows us to treat models with lateral variations of viscosity. In Chapter 4, for laterally homogeneous viscosity models, the SFE method is benchmarked by comparison against the matrix propagator solution. Hence, the formalism of mantle Green's functions is described along with a simple inversion of the long-wavelength geoid in terms of a three-layer mantle viscosity. In Chapter 5 we start dealing with lateral viscosity variations. We derive a semi-analytical solution of the Stokes problem in the presence of an axisymmetric distribution of viscosity, that allows us to validate the SFE method. Finally, in Chapter 6, we show some results concerning the long-wavelength geoid associated with axisymmetric models of subduction. Three appendices containing a few technical details of the derivations presented throughout the chapters complete this work.

CHAPTER 1

Introductory concepts

We briefly review the fundamental features of the geophysical quantities that will be needed to develop and understand a model of present-day mantle convection. We describe the non-hydrostatic geoid, as it is the principal surface observable that we must be able to model and global seismic tomography, as it is a unique source that provides us with important information concerning the current dynamic configuration of the mantle. The chapter is completed by a qualitative description of the physical mechanism that allows us to build a mathematical model that uses the data of seismic tomography to predict the non-hydrostatic geoid.

1.1 Non-hydrostatic geoid

The *geoid* is commonly defined as the surface of constant gravity potential that roughly coincides with mean sea level over oceans. Because of the effects due to waves, tides and all other dynamical processes within the ocean, mean sea level is not an exact equipotential. Moreover, wherever there are continents, the geoid lies beneath the Earth's surface, with the consequence that the equipotential surface is deformed by the attraction of the overlying masses. Nevertheless, geodesists define the geoid as though the mass were always underneath the geoid itself instead of above.

In the definition of geoid we refer to the 'gravity potential'. With this, we refer here to the gravitational plus rotational potential. The potential of a rotating body having the shape of an ellipsoid of revolution is well approximated by the following relation (e.g. Heiskanen & Moritz, 1967)

$$W(r,\vartheta) = \frac{GM}{r}\left[1 - J_2\left(\frac{a}{r}\right)^2 P_2(\cos\vartheta)\right] + \frac{1}{2}r^2\omega^2\sin^2\vartheta, \tag{1.1}$$

where r and ϑ are the radius and the latitude of a spherical coordinate system, G is the constant of gravitation, M the mass of the body, a its mean radius,

$J_2 \equiv (C - A)/Ma^2$, where C and A are the moment of inertia about polar and equatorial rotational axes, respectively, P_2 is the Legendre polynomial of the second order and ω is the angular velocity. The first term of eq. (1.1) accounts for the gravitational potential, while the second for the rotational potential of the ellipsoid. However, the Earth is definitely a more complicated body than a simple rotating ellipse, and so is its potential. Choosing a coordinate system whose origin coincides with the center of mass, the gravity potential for a realistic Earth can be expressed by means of an infinite series of spherical harmonic functions Y_{jm} (see Appendix A) as follows:

$$U(r,\Omega) = \frac{GM}{r}\left[1 + \sum_{j=2}^{\infty}\sum_{m=-j}^{j}\left(\frac{a}{r}\right)^j U_{jm}Y_{jm}(\Omega)\right] + \frac{1}{2}r^2\omega^2\sin^2\vartheta, \qquad (1.2)$$

where $\Omega \equiv (\vartheta, \varphi)$ denotes the latitude and longitude and U_{jm} are constant coefficients. Using eq. (1.1), it can be shown that eq. (1.2) can be written as

$$U(r,\Omega) = W(r,\Omega) + V(r,\Omega), \qquad (1.3)$$

where V represents the so called *disturbing gravitational potential*.

The surface for which the reference potential (1.1) is constant represents the *reference ellipsoid* or *reference geoid*, while the surface with constant potential (1.3) represents the actual geoid of the Earth. It is clear that deviations between these two surfaces are connected to the disturbing potential V. The *non-hydrostatic geoid* (also called *geoid undulation* or *geoid anomaly*) is the difference in height between these two surfaces which, according to the Bruns theorem (e.g. Heiskanen & Moritz, 1967), has the simple expression

$$N(\Omega) = \frac{V(a,\Omega)}{g_0(a)}, \qquad (1.4)$$

where the reference gravitational acceleration g_0 and the disturbing potential are both computed at the mean radius $r = a$. From now on, for simplicity, we will use without distinction either the terms *geoid* or *geoid anomaly* or *non-hydrostatic geoid*, meaning the quantity of eq. (1.4).

1.2 Geoid and gravity maps

In the past, geoid determination was based exclusively on gravity measurements on the ground. Nowadays is it much easier to determine the global geoid from satellite observations. In general, the global large-scale features of the geoid are expressed by a spherical harmonic expansion:

$$N(\Omega) = \sum_{j=2}^{j_{\max}}\sum_{m=-j}^{j} N_{jm}Y_{jm}(\Omega), \qquad (1.5)$$

where $j_{\max}$ is the cutoff degree of such expansion. The higher-degree terms are well defined by ground gravity data, while the lower-degree terms, that describe

the long-wavelength part of the signal, by satellite-tracking data. Recent satellite missions, such as the Gravity Recovery and Climate Experiment (GRACE) (Tapley et al., 2004), provide the most accurate measurements currently available of the geoid and its temporal variations. Figure 1.1 shows the geoid map based on the recent GRACE gravity field solution of Förste et al. (2006).

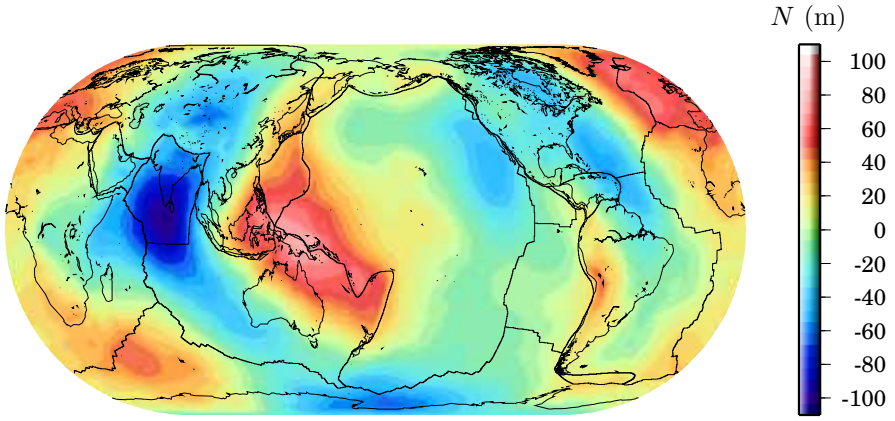

Figure 1.1: Geoid map from GRACE ($j_{\max} = 360$).

As we see from this figure, geoid heights are relatively small. They range from a minimum of about -105 m located over the Indian Ocean to a maximum of approximately 100 m over New Guinea. The largest amplitude features are at the largest scale. We observe broad highs over the western Pacific Ocean and Africa, separated by a band of lows that follow roughly a great circle passing through western Atlantic Ocean, the poles, Central Asia, India and Indian Ocean. A distinctive positive signal shows up over the Andes in South America. If we consider these elementary observations from the point of view of plate tectonics and mantle convection, the geoid presents some apparent paradoxes. As plate tectonics the surface manifestation of mantle convection, we might expect the geoid to be dominated by features related to plate boundaries or to continents. But this is clearly not the case. As pointed out by many authors (Runcorn, 1967; McKenzie, 1977; Davies, 1981; Hager, 1984), subduction zones are always associated with relative highs of the long-wavelength geoid. However, there is no such a clear correlation between geoid and ridges. In fact, the Mid-Atlantic and Atlantic-Indian ridges are mainly associated with relative geoid highs, while the South Indian ridge and the East Pacific Rise exhibit relative geoid lows. According to these simple observations, it is clear that, although geoid (and gravity anomalies) are caused by variations in the density of the Earth's interior, their distribution is not simply correlated with the distribution of the density itself. Beneath subduction zones, the mantle contains positive density anomalies and therefore the observed geoid highs are expected, but beneath oceanic ridges, the mantle is characterized by light hot upwellings that should be associated with negative geoid anomalies. In Sec. 1.5, we will clarify the mechanism that allows

us to build a mathematical model of the geoid that can be reconciled with the observations.

The geoid is actually a measure of the strength of the gravity field. Thus we can also look at gravity instead of geoid-anomalies. There is a fundamental difference between these two quantities. Gravitational attraction is proportional to r^{-2}, where r is the distance from the attracting mass, while the gravitational potential is proportional to r^{-1}. Since the geoid is a measure of the latter, it is sensitive to mass over greater distances and hence to deeper or larger-scale density variations. Figure 1.2 shows the degree power spectrum of the geoid and gravity anomaly. From the figure it is clear that power of gravity decreases with the harmonic degree much more slowly than the geoid power, with the consequence that shorter wavelengths are amplified and more easily visible in the gravity field than in the geoid. This explains the reason why, looking at

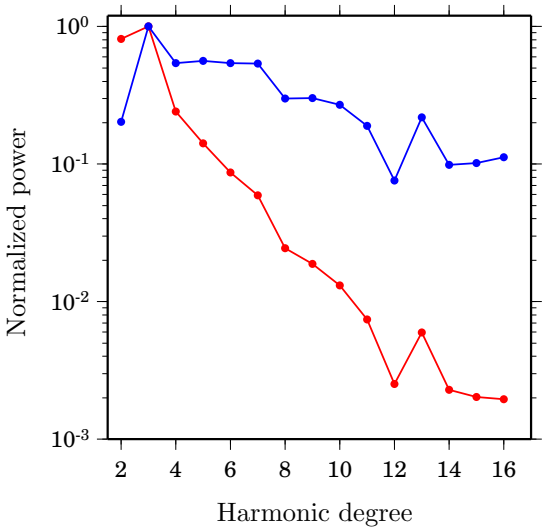

Figure 1.2: Normalized degree power spectrum from GRACE of geoid (red line) and gravity (blue line) anomalies.

a map of gravity anomalies (Fig. 1.3), features with shorter wavelengths with respect to those of the geoid are emphasized. Gravity and geoid anomalies are globally well correlated. Gravity highs are clear over subduction and convergence zones, whereby the geoid exhibits there stronger long-wavelength components. The main band of geoid lows also appears in the gravity map, although it is less pronounced.

Geoid and gravity are a direct expression of the density distribution of the mantle. We now turn our attention to the method that allows us to image the current density configuration of the Earth's interior.

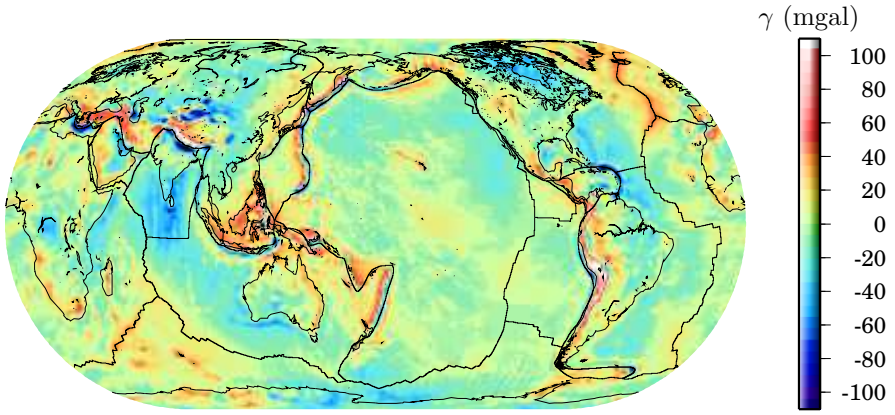

Figure 1.3: Map of gravity anomalies from GRACE ($j_{\max} = 360$).

1.3 Seismic tomography

If we want to make inferences about the observed geoid, it is necessary to know first the current density distribution of the Earth's mantle, or, equivalently, assuming that density anomalies are of thermal and not of chemical origin, the three-dimensional distribution of the temperature. Among different approaches used by geophysicists to investigate the Earth's interior, *seismic tomography* is the only one capable to visualize, at the same time, temperature, petrological anomalies and flow directions from seismic velocity and anisotropy heterogeneities (Montagner, 1994).

The first three-dimensional seismic models of the Earth's mantle were proposed by the end of the 1970s (Dziewonski et al., 1977). Starting from the mid-1980s, the number and degree of sophistication of tomographic models has increased steadily. Since then, numerous models have been derived from different types of seismological measurements and using different techniques (e.g. Woodhouse & Dziewonski, 1984; Nataf et al., 1986; Su & Dziewonski, 1997; van der Hilst et al., 1997; Boschi & Dziewonski, 1999; Ritsema & van Heijst, 2000). The value of tomography originates from the large variety of seismic waves that 'illuminate' the Earth's interior from different angles. Earthquakes act as a source emitting seismic waves over a large frequency range that can travel within the Earth. Body waves (P or S waves) can travel deeply in the mantle and this is the reason why they are employed in tomographies that involve the whole mantle. Surface waves (Love and Rayleigh waves), on the other hand, travel only more superficially, and are the basis of tomographic studies of the upper mantle.

The data upon which tomographic models are built are the three component seismograms that reproduce the movement of particles induced by the passage of seismic waves and that are provided by seismological networks. The construction of a tomographic model is based essentially on the solution of a non-linear inverse problem (see for example Kennett (2001)). The data $\boldsymbol{d}$, are related to a model of

the laterally heterogeneous Earth structure perturbation $\delta\boldsymbol{m}(\boldsymbol{r})$ by a non-linear functional extended to the Earth's whole volume. By linearization and assuming that waves travel along rays, the functional relation between model and data can be simply written as a path integral between the source S (the earthquake) and the receiver R (the seismograph):

$$\boldsymbol{d} = \int_S^R G(s)\, \delta\boldsymbol{m}(\boldsymbol{r})\, ds(\boldsymbol{r}), \tag{1.6}$$

where $ds(\boldsymbol{r})$ is the infinitesimal arc length at point $\boldsymbol{r} = (r, \Omega)$ along the propagation path between R and S, and $G(s)$ is a kernel calculated from a reference radially symmetric model. For body waves, the data are delay times δt_i measured at seismic station i and eq. (1.6) takes the following form:

$$\delta t_i = \int_{S_i}^{R_i} \delta\left[\frac{1}{v(\boldsymbol{r})}\right] ds(\boldsymbol{r}), \tag{1.7}$$

where $\delta[1/v]$ is the perturbation along the path due to the slowness distribution. Upon inversion of the travel times δt_i we can retrieve the slowness $\delta[1/v]$ and hence velocity perturbations. The scheme described above is valid for the propagation of body-waves under the assumption that they travel along rays, so that the volume integration can be reduced to a path integration. As it is usually the case, a tomographic model is built not only from body waves but also from surface waves and/or free-oscillations. We will limit ourselves to mentioning that, for the latter types of waves, the problem is more complex, being two-dimensional and frequency dependent.

In the following, we will be dealing mostly with tomographic models based on the inversion of travel-time data of body waves. Such models provide us with the three-dimensional distribution of velocity perturbations $\delta v(r, \Omega)$, with respect to the average radially symmetric Preliminary Reference Earth Model (PREM) (Dziewonski & Anderson, 1981). When the effects of heterogeneity in the chemical composition of the mantle can be neglected, the main sources for lateral variations δv in velocity are lateral variations in temperature. Velocity perturbations, in this case, are proportional to temperature anomalies and hence to density anomalies $\delta\rho(r, \Omega)$. Slow regions should then represent hot, buoyant upwellings, while fast regions cold downwellings. According to this picture, tomographic models can be seen as a snapshot of the convecting mantle. Thus, in order to map the three-dimensional velocity structures δv delivered by tomographic models into a corresponding three-dimensional density field $\delta\rho$, it has become common practice to employ the following standard linear relation

$$\frac{\delta\rho(r, \Omega)}{\rho_0(r)} = \frac{\partial \ln \rho}{\partial \ln v}(r) \frac{\delta v(r, \Omega)}{v_0(r)}, \tag{1.8}$$

where ρ_0 and v_0 are depth-dependent average density and velocity profiles, respectively, as described by PREM, and $\partial \ln \rho / \partial \ln v$ is a dimensionless depth-dependent velocity to density scaling factor. Relationship (1.8) is most probably

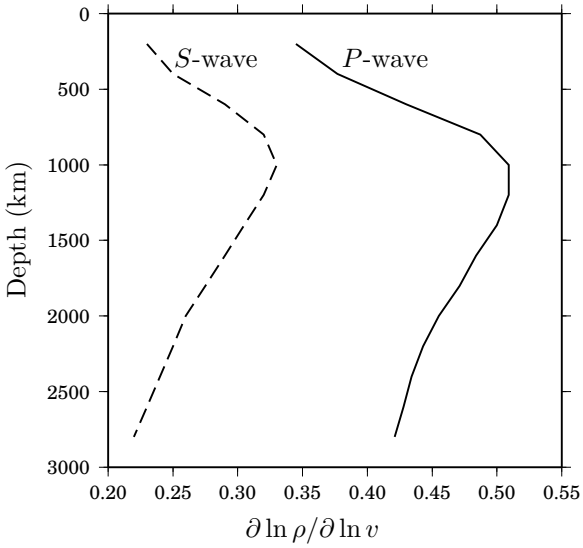

Figure 1.4: Depth variation of the velocity to density scaling factor $\partial \ln \rho / \partial \ln v$ for P- and S-waves according to Karato (1993).

adequate to describe well-mixed adiabatic regions of the mantle (Pari & Peltier, 1998). In Fig. 1.4, the depth-dependence of the scaling factor $\partial \ln \rho / \partial \ln v$ for P- and S-waves is shown in the form that has been proposed by Karato (1993).

Tomographic models based on seismic data are not the only available source from which a snapshot of the present-day mantle density configuration can be obtained. Another possibility is to make use of the so-called *geodynamic tomographies*. Using Cenozoic and Mesozoic plate motions reconstructions and assuming that subducted slabs are the primary source of thermal buoyancy in the mantle, Ricard et al. (1993) were the first to build a geodynamical model of present-day mantle density heterogeneity that, at least at long-wavelength scales, correlated well with seismic tomographies and can thus be considered as a valuable alternative to models based on seismic data. Recently, using a similar methodology, Steinberger (2000) developed another geodynamic model of mantle densities that incorporates a more realistic treatment of the convective flow.

1.4 Average tomographic models

Nowadays, there are many different tomographic models of the entire mantle available and a choice of a particular one can be quite arbitrary. Becker & Boschi (2002) have conducted a comprehensive analysis of similarities and differences between several recent models and described very rigorously their correlation at different wavelengths. Upon comparing the most recent global models available at this time, including P-waves models, S-waves models combined with data

of surface wave propagation and geodynamic models, Becker & Boschi (2002) concluded that the long-wavelength components of most tomographic models considered are well correlated with each other, especially in the lowermost mantle where the coverage of travel-time data is most uniform. From these results, they also built two average models: *pmean* based on P-waves and *smean* based on S-waves. These two models are derived from weighted averages of well-correlated P- and S wave models, respectively, and can be considered to be reference models that contain the most robust features that different tomographic techniques are able to reveal. Fig. 1.5 shows models *pmean* and *smean* at different depths in terms of velocity perturbations expressed in percentage with respect to PREM. The shallow upper mantle reveals the characteristic high velocity signal due to the presence of thick and cold lithospheric roots of continents (e.g. Nataf & Ricard, 1996). Most of the positive anomalies that are clearly visible in the mid mantle, such as those beneath Chile and Peru, Tonga and Japan, for instance, are due to subducted slabs. On the other hand, it is more difficult to relate negative anomalies that denote slower seismic wave velocities to convective features. Morgan (1970) first hypothesized the existence in a convective mantle of upwellings having the form of narrow plumes and, since then, numerous studies have been devoted to mantle plumes (e.g. Griffiths & Campbell, 1990; Hill, 1991; Farnetani & Richards, 1994). However, global tomography is currently unable to image such structures (Ritsema et al., 1999), although recent (and controversial) results (Montelli et al., 2003) seem to claim the opposite. Moreover, from Fig. 1.5, no clear correlation between hot spot locations (Duncan & Richards, 1991) and negative tomographic signal is observed. However, at large depths (1510 km and below), two marked positive anomalies centered around south-west Africa and central Pacific, likely imaging super-plumes, are easily recognizable (e.g. Lithgow-Bertelloni & Silver, 1998; To et al., 2005).

1.5 Fluid-dynamical model of the geoid

The key problem is now how to make use of the density anomalies inferred from seismic tomography and compute the associated geoid. We can explain this with a simple argument. As first relatively simple attempt, we can build a *static* model of the geoid. Newton's law can be used to relate directly the tomographic density anomalies $\delta\rho$ to the corresponding gravity potential V (and hence, through eq. (1.4), to the corresponding geoid) as follows:

$$V(\boldsymbol{r}) = G \int_{\mathcal{B}} \frac{\delta\rho(\boldsymbol{r}')}{L}\, d^3\boldsymbol{r}', \tag{1.9}$$

where G is the constant of gravitation, $\mathcal{B}$ is the mantle volume and L is the angular distance between the point $\boldsymbol{r}$ at which the potential is computed (for the geoid, the Earth's surface) and the point $\boldsymbol{r}'$ where the density anomaly is located. As shown for, instance, by Hager & Clayton (1989), by simply applying eq. (1.9), we would find that the geoid is about a factor of 4 larger in peak to peak amplitude with respect to the observed one and is essentially anti-correlated

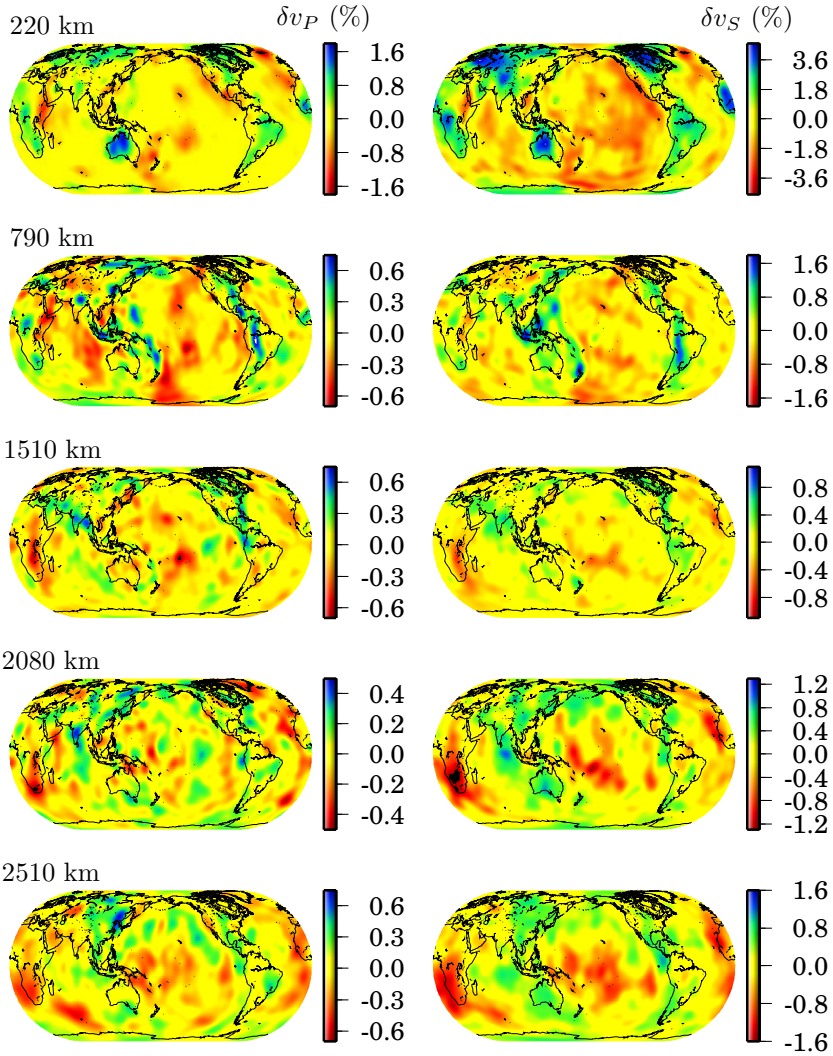

Figure 1.5: Velocity perturbations (with respect to PREM) at different depths of the P-waves model *pmean* (left panel) and S-wave model *smean* (right panel) derived by Becker & Boschi (2002).

with it. One interpretation of the anti-correlation is that seismic and density anomalies are not simply related through eq. (1.8) if they result from variations in chemical composition, which can lead to a negative value in their ratio (e.g. Dziewonski et al., 1977). This interpretation is now not considered valid because it would require the existence of long-lived chemical heterogeneities that would have led to far more profound chemical differentiation than now exist (Hager & Clayton, 1989).

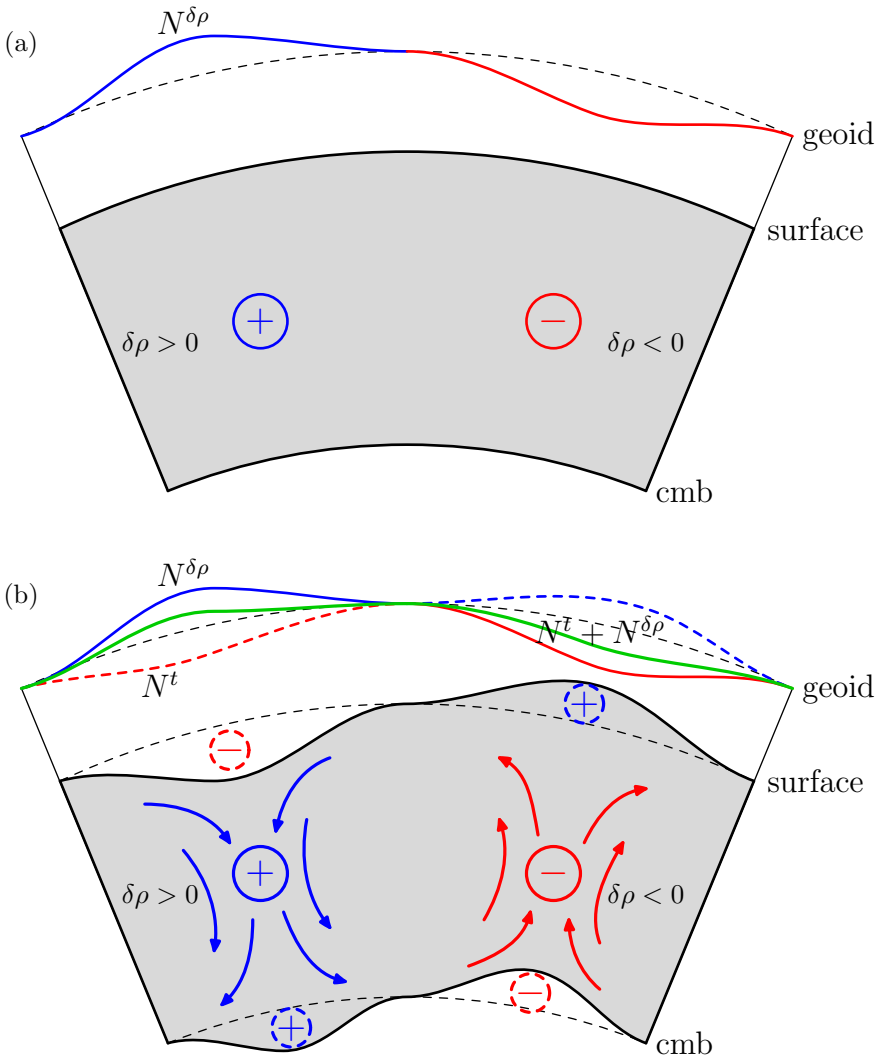

Figure 1.6: A cartoon illustrating the basic physical mechanism that explains geoid anomalies. (a) Static geoid anomaly $N^{\delta\rho}$ due to the primary contribution of internal density anomalies $\delta\rho$: a positive (negative) geoid anomaly corresponds to a positive (negative) density anomaly. (b) Mantle flow associated with primary density anomalies induces boundary deformations and hence additional density anomalies, with which the geoid N^t (dashed line) is associated. The total geoid (green line) is the sum of the two contributions.

According to the model of convecting mantle, a more likely reason for the discrepancy is the lack of a proper treatment of the deformation of the chemical boundaries of the mantle. The upper surface of the Earth does not exhibit significant traction (Busse, 1989). This requires that convection in the mantle

must generate a dynamic deformation (*dynamic topography*) of this surface that is maintained away from its equilibrium position. A similar consideration applies to the core-mantle boundary (CMB) and any discontinuity in chemical composition that might exist in the mantle. In one of the first studies where thermal mantle convection was hypothesized, Pekeris (1935) observed:'*The general nature of the distortion of the crust can be seen at once. Over the rising current it will be pushed upwards and it will be pulled downwards over the sinking current'.* Since Pekeris pioneering work, this argument has been later addressed and expanded upon by several authors, among them Runcorn (1964, 1967); McKenzie (1977); Ricard et al. (1984). Pekeris' words contain a simple, yet clear description of the physical mechanism that allows us to reconcile model and observations. In Fig. 1.6a, we show a sketch of the mantle containing a positive and a negative density heterogeneity depicted in blue and red, respectively. According to the static model described above, a positive and a negative geoid anomaly must be present over the positive and negative density anomaly, respectively. In Fig. 1.6b, according to the Pekeris *dynamic* picture, mantle flow associated with the positive anomaly (sinking material that is colder and heavier than the surrounding) tends to drag the surface and push the CMB downward, thereby creating two additional density anomalies that contribute to the geoid signal. The flow associated with the negative anomaly (rising material that is hotter and lighter than the surrounding) produces the opposite effect. It turns out that the static and dynamic contributions have similar amplitudes and opposite signs. The total geoid (depicted by the green line in Fig. 1.6) is then the result of these two different (and opposing) contributions. Thus, even if we were completely sure about the present knowledge of density heterogeneities, the geoid depends strongly upon the rheology of our planet and a careful modeling of a snapshot of present-day mantle flow is necessary.

Although the dynamic topography represents a basic ingredient for geoid computation, on the real Earth it is a quantity which cannot be easily observed. On the one hand, most of the Earth's topography that we are familiar with is related to crustal thickness variations or to thermal cooling of the lithosphere, so the main contribution to the observed topography is due to mechanisms of isostatic compensation that account for the density variations in the crust and lithosphere. On the other hand, as explained above, mantle flow produces boundary deflections and hence a dynamic topography. Observing the present-day dynamic topography consists of stripping off the effects of the isostatic components from the total surface topography (Le Stunff & Ricard, 1997). What is certainly clear, however, is that the amplitude of the dynamic topography is definitely smaller than that of the 'isostatic' topography. Over the oceans, it is estimated that it has a peak to peak amplitude of approximately 400 m (Kido & Seno, 1994). Over continents the amplitude of the long-wavelength dynamic topography is probably smaller then 1 km (Gurnis, 1990; Panasyuk & Hager, 2000). Here, however, the problem is seriously complicated by the fact that a very good knowledge of lithospheric density variations is required. These values are somehow at odd with those estimated using flow models. The latter,

though successful in fitting the geoid, generally predict too large peak to peak amplitudes of dynamic topography by the order of several kilometers (Hager & Clayton, 1989; Forte et al., 1993; Ricard et al., 1993) and some form of mantle layering (e.g. Le Stunff & Ricard, 1997; Čadek & Fleitout, 1999) must be invoked to reduce it (see also Section 3.10).

CHAPTER 2

Matrix propagator technique

After introducing the partial differential equations that govern the flow in the mantle and the gravitational potential, we briefly review the technique of the matrix propagator which is generally employed to solve such equations in a spherical geometry under the approximation of laterally homogeneous viscosity. The method allows us to obtain an analytical solution in terms of the spherical harmonic expansion of the field quantities. In the presence of lateral viscosity variations, this method is no longer applicable and a numerical approach, such as that presented in Chapter 3, is required. Nevertheless, since it provides analytical solutions, the matrix propagator represents an extremely useful tool for validating numerical codes for the case of radially symmetric viscosity distributions.

2.1 Basic equations and approximations

In order to describe quantitatively the concepts outlined in Section 1.5, we will assume that the mantle can be modeled, as a reasonable approximation, as an incompressible Newtonian viscous fluid. The assumption of incompressibility is usually justified by the fact that hydrodynamic stresses involved in mantle convection are much smaller than hydrostatic pressure changes (Busse, 1989). Nonetheless, this remains a somewhat crude approximation since a parcel that flows from the uppermost mantle to the core-mantle boundary almost doubles in density. The effect of compressibility has been extensively studied in general models of thermal convection (e.g. Jarvis & McKenzie, 1980) and in flow models devoted to the prediction of surface observables (Forte & Peltier, 1991; Dehant & Wahr, 1991; Thoraval et al., 1994; Corrieu et al., 1995; Defraigne et al., 1996). As far as the latter type of studies is concerned, the consensus is that a compressible mantle can lead to changes that, for instance, are not large enough to notably impact on viscosity estimates obtained by comparison with the observed geoid (Defraigne et al., 1996). Therefore, in the following, compressibility will be

neglected and mantle flow will be considered incompressible.

To model such a flow, the accompanying boundary deformations and the gravitational potential, we need to choose an appropriate constitutive equation and solve the linear momentum equation, the equation of mass conservation and the Poisson equation, subject to suitable boundary conditions. The general form of the equation of mass conservation (*continuity equation*) reads as

$$\frac{\partial \rho}{\partial t} + \operatorname{div}(\rho \boldsymbol{u}) = 0, \tag{2.1}$$

where ρ is the density and $\boldsymbol{u}$ the Eulerian flow velocity. The linear momentum equation for viscous flow is the Navier-Stokes equation, i.e.

$$\rho \frac{D\boldsymbol{u}}{Dt} = \operatorname{div} \boldsymbol{\tau} + \rho \operatorname{grad} V, \tag{2.2}$$

where $D/Dt \equiv \partial/\partial t + \boldsymbol{u} \cdot \operatorname{grad}$ is the material time derivative and $\rho \operatorname{grad} V$ is the body forcing term due to the gravitationally unstable mass density ρ, with V representing the gravitational potential that can be obtained solving the Poisson equation

$$\nabla^2 V = 4\pi G \rho. \tag{2.3}$$

In general, the rheology of a continuum can be expressed in terms of a constitutive law for the Cauchy stress tensor $\boldsymbol{\tau}$ as follows:

$$\boldsymbol{\tau} = -p\boldsymbol{I} + \boldsymbol{D}(\dot{\boldsymbol{\varepsilon}}^{\mathrm{d}}), \tag{2.4}$$

where $\boldsymbol{I}$ is the identity tensor, $p = \operatorname{Tr}(\boldsymbol{\tau})/3$ is the pressure (Tr is the trace operator), $\boldsymbol{D}(\dot{\boldsymbol{\varepsilon}}^{\mathrm{d}})$ is the deviatoric part of the stress tensor and $\dot{\boldsymbol{\varepsilon}}^{\mathrm{d}}$ is the deviatoric strain-rate. Microphysical analysis of polycrystalline silicates leads to the conclusion that mantle flow is likely to be governed by a non-linear constitutive law (Ranalli, 1995) according to which the deviatoric part of the stress is a non-linear function of $\boldsymbol{D}$:

$$\dot{\boldsymbol{\varepsilon}}^{\mathrm{d}} = A(\boldsymbol{D} : \boldsymbol{D})^{(n-1)/2} \boldsymbol{D},$$

where the symbol ':' denotes the double-dot product of tensors, i.e. $\boldsymbol{D} : \boldsymbol{D} = D_{ij} D_{ij}$, A is a function of spatial variables and the stress exponent n is a material constant (for olivine, for example, $n = 4$). Mantle flow models that incorporate such non-linear rheology have been considered in the literature within the framework of 2-D simulations in Cartesian geometry (Christensen, 1984; Malevsky & Yuen, 1992) and 3-D spherical geometry (Christensen & Harder, 1991; Čadek et al., 1993). In addition, a Maxwell viscoelastic rheology, traditionally employed for modeling the post-glacial rebound (e.g. Martinec, 2000), has also been considered in models of mantle convection (Harder, 1991). However, as we mentioned above, we will assume that the mantle can be modeled using a simple linear viscous (or Newtonian) rheology. Although this assumption may

be debatable, simple Newtonian flow has been used during the past two decades and has proven to be successful in explaining important geophysical observables. For such a flow, the stress exponent is $n = 1$ and the deviatoric part of the stress takes the following form:

$$\boldsymbol{D}(\dot{\boldsymbol{\varepsilon}}^{\mathrm{d}}) = 2\eta\dot{\boldsymbol{\varepsilon}}^{\mathrm{d}},$$

where η is the shear viscosity. The deviatoric strain-rate is

$$\dot{\boldsymbol{\varepsilon}}^{\mathrm{d}} = \dot{\boldsymbol{\varepsilon}} - \frac{1}{3}\mathrm{Tr}(\dot{\boldsymbol{\varepsilon}}),$$

where

$$\dot{\boldsymbol{\varepsilon}} = \frac{1}{2}(\mathrm{grad}\,\boldsymbol{u} + \mathrm{grad}\,{}^{t}\boldsymbol{u}) \tag{2.5}$$

is the strain-rate, with the superscript ^{t} denoting the operation of transposition.

Since the density perturbations that excite mantle flow are much smaller than the ambient hydrostatic density, it is common practice to express density, pressure and gravitational potential in terms of first-order perturbations from their reference hydrostatic values. Thus, denoting with (r, ϑ, φ) the radius, co-latitude and longitude of a spherical coordinate system, we can write:

$$\begin{aligned}
\rho(r,\vartheta,\varphi) &= \rho_0(r) + \delta\rho(r,\vartheta,\varphi),\\
p(r,\vartheta,\varphi) &= p_0(r) + \delta p(r,\vartheta,\varphi),\\
V(r,\vartheta,\varphi) &= V_0(r) + \delta V(r,\vartheta,\varphi).
\end{aligned}$$

In eq. (2.1), the time derivative of the density is ignored since mantle flow velocities are negligible with respect to the speed of sound (e.g. Landau & Lifshitz, 1987). Moreover, as anticipated before, in our treatment we will assume that the flow is incompressible. The density distribution of the reference state is then considered constant ($\rho_0 = \mathrm{const}$) and eq. (2.1) reduces to:

$$\mathrm{div}\,\boldsymbol{u} = 0. \tag{2.6}$$

An immediate consequence of eq. (2.6) is that the deviatoric strain-rate and the strain-rate coincide because $\mathrm{Tr}(\dot{\boldsymbol{\varepsilon}}) = \mathrm{div}\,\boldsymbol{u} = 0$. In the linear momentum equation (2.2), as is appropriate for mantle flow, the infinite Prandtl number approximation is applied and the inertial term (left-hand side of equation 2.2) is then neglected. In fact, the Prandtl number Pr is the non-dimensional number defined as the ratio of momentum diffusivity and thermal diffusivity. Due due to the extremely high viscosity of the mantle, Pr can be considered infinite. When Navier-Stokes equations are written in non-dimensional form along with the advection-diffusion equation for the energy conservation (e.g. Landau & Lifshitz, 1987), the inertial term is multiplied by Pr^{-1} and hence becomes negligible. Moreover, if we subtract the reference hydrostatic state and keep terms to first-order accuracy, eq. (2.2) becomes

$$\mathrm{div}\,\delta\boldsymbol{\tau} + \rho_0\,\mathrm{grad}\,\delta V + \delta\rho\,\mathrm{grad}\,V_0 = 0, \tag{2.7}$$

which is usually known as *Stokes equation* and where $\delta\boldsymbol{\tau}$ denotes the perturbation of the stress tensor. Similarly, eq. (2.3) can be written

$$\nabla^2 \delta V = 4\pi G \delta\rho. \tag{2.8}$$

In eq. (2.7), the buoyancy force that drives convection through lateral density heterogeneities is represented by the term $\delta\rho \operatorname{grad} V_0$, while the term $\rho_0 \operatorname{grad} \delta V$ accounts for the self-gravitation of the Earth. According to the latter mechanism, the free-surface of the planet tends to line up with the equipotential arising because of the density anomaly $\delta\rho$ and to create then an additional surface anomaly similar but definitely smaller than that due to the flow-induced boundary deformations. In fact, in geoid computations, self-gravitation can cause changes of approximately 10% (Forte & Peltier, 1991).

In the following, eqs (2.7) and (2.8) will be solved for the flow $\boldsymbol{u}$, the non-hydrostatic pressure δp and the perturbed potential δV. Thus, in order not to overwhelm the notation, the latter two variables will be simply denoted by the symbols p and V, respectively, along with the perturbed stress tensor for which the symbol $\boldsymbol{\tau}$ will be used.

2.2 Boundary conditions

Equations (2.6), (2.7) and (2.8) are to be satisfied within the mantle volume, which we will indicate by $\mathcal{B}$. On the boundary $\partial\mathcal{B} = \partial\mathcal{B}^{\mathrm{a}} \cup \partial\mathcal{B}^{\mathrm{c}}$, where $\partial\mathcal{B}^{\mathrm{a}}$ and $\partial\mathcal{B}^{\mathrm{c}}$ denote the Earth's surface and the core-mantle boundary, respectively, suitable boundary conditions must supplement eqs (2.6), (2.7) and (2.8).

Let us start with the boundary conditions for the mass conservation and Stokes equations. When modeling the Earth, the most typical interface encountered is the contact boundary between two different materials with no flow passing through. Such a boundary is usually called *chemical* to emphasize the fact that the regions existing on either side have a distinct chemical composition. Several types of boundary conditions can be used (for a thorough description, see for instance Thoraval & Richards (1997)). A natural choice is to consider $\partial\mathcal{B}$ as being stress-free. In spherical geometry, this condition is expressed mathematically by requiring that the traction vector vanishes on $\partial\mathcal{B}$:

$$\boldsymbol{\tau} \cdot \boldsymbol{e}_r = 0, \tag{2.9}$$

where $\boldsymbol{e}_r$ is the radial unit vector. In this case, there is a net mass flux through the boundary, which means that $\partial\mathcal{B}^{\mathrm{a}}$ and $\partial\mathcal{B}^{\mathrm{c}}$ are not fixed and can deform under the action exerted by internal forces, which in turn define topographic undulations. However, solving partial differential equations in a domain with changing boundaries is a difficult problem from a numerical point of view. This is the reason why eq. (2.9) is generally replaced by considering *fixed, impermeable and free-slip* boundaries, as follows:

$$\boldsymbol{u} \cdot \boldsymbol{e}_r = 0, \tag{2.10}$$

$$\boldsymbol{\tau} \cdot \boldsymbol{e}_r - ((\boldsymbol{\tau} \cdot \boldsymbol{e}_r) \cdot \boldsymbol{e}_r)\boldsymbol{e}_r = 0. \tag{2.11}$$

The impermeability condition (2.10), guarantees that there is no mass flux across $\partial\mathcal{B}$, which is then fixed, while condition (2.11) requires that shear (or tangential) stresses vanish on $\partial\mathcal{B}$. Note that the normal component of the surface traction $\tau_{rr} = (\boldsymbol{\tau} \cdot \boldsymbol{e}_r) \cdot \boldsymbol{e}_r$ does not need to be zero. It is rather interpreted like the force that produces the *dynamic topography* h of the boundary $\partial\mathcal{B}$:

$$h = -\frac{\tau_{rr}}{\Delta\rho_0\, g_0}, \tag{2.12}$$

where $\Delta\rho_0$ is the change of the reference density across $\partial\mathcal{B}$ and g_0 the reference gravitational acceleration at $\partial\mathcal{B}$. Equation (2.12) has a clear physical meaning: The surface traction τ_{rr} balances the pressure force due to the displaced topography h.

So far, we have discussed boundary conditions for eqs (2.6) and (2.7). The Poisson equation (2.8) must also be supplemented by boundary conditions, since it is not valid at points where the density is discontinuous and in the presence of surface-mass density contrasts. Surface-mass densities do not exist in the real world, but are often used to approximate thin layers of mass because they greatly simplify the mathematical treatment of certain problems. Since in eq. (2.12) h is small (see also Section 1.5) compared to the characteristic dimensions of the mantle, we can define the surface-mass density contrast induced by mantle flow at the boundary $\partial\mathcal{B}$ as:

$$\sigma^h \equiv h\,\Delta\rho_0 = -\frac{\tau_{rr}}{g_0}. \tag{2.13}$$

It can be shown (e.g. Dahlen, 1974) that, to account for density jumps and surface-mass density contrasts, respectively, at $\partial\mathcal{B}$, the gravitational potential and gravitational intensity must satisfy the following conditions:

$$[V]^+_- = 0, \tag{2.14}$$

$$[\boldsymbol{e}_r \cdot \operatorname{grad} V]^+_- + 4\pi G\sigma^h = 0, \tag{2.15}$$

where the symbol $[f]^+_-$ indicates the jump of the quantity f on $\partial\mathcal{B}$ and the super(sub)script $+$ $(-)$ denotes the evaluation of f on the external (internal) side of $\partial\mathcal{B}$. Actually, the original form of the boundary condition (2.15) that can be found in Dahlen (1974) is

$$[\boldsymbol{e}_r \cdot \operatorname{grad} V + 4\pi G\rho_0\,(\boldsymbol{e}_r \cdot \boldsymbol{d})]^+_- = 0, \tag{2.16}$$

where $[\rho_0]^+_- = \Delta\rho_0$ and $\boldsymbol{d}$ is the vector of *Lagrangian* displacement that is not known, since, using the flow velocity $\boldsymbol{u}$, we are working with *Eulerian* variables. Nevertheless, the dynamic topography h of eq. (2.12) coincides with the radial displacement $\boldsymbol{e}_r \cdot \boldsymbol{d}$ and substituting it into eq. (2.16) yields the condition (2.15).

Note that, in order to apply eqs (2.14) and (2.15), it is necessary to know the external potentials V^{a^+} and V^{c^-}, above the Earth's surface and beneath the CMB, respectively. In these regions there are no density anomalies ($\delta\rho$=0) and V simply satisfies the Laplace equation:

$$\nabla^2 V = 0. \tag{2.17}$$

The solution to eq. (2.17) can be expressed in terms of a spherical harmonic series. For a radius r larger than the Earth radius a, the potential reads as

$$V^{\mathrm{a}^+}(r,\Omega) = \sum_{jm} V_{jm}^{\mathrm{a}^+} \left(\frac{a}{r}\right)^{j+1} Y_{jm}(\Omega), \tag{2.18}$$

while at a radius smaller than the CMB radius c, we have

$$V^{\mathrm{c}^-}(r,\Omega) = \sum_{jm} V_{jm}^{\mathrm{c}^-} \left(\frac{r}{c}\right)^{j} Y_{jm}(\Omega), \tag{2.19}$$

where the symbol Ω is used to denote the angular variables (ϑ, φ).

2.3 Reduction to a system of ordinary differential equations

We show now how the continuity, Stokes and Poisson equations can be arranged to form a system of linear ordinary differential equations.

For convenience, we rewrite them together with the constitutive equation for the stress tensor $\boldsymbol{\tau}$:

$$\operatorname{div} \boldsymbol{u} = 0 \tag{2.20}$$

$$\operatorname{div} \boldsymbol{\tau} + \rho_0 \operatorname{grad} V - \boldsymbol{g}_0 \delta\rho = 0 \tag{2.21}$$

$$\boldsymbol{\tau} = -p\boldsymbol{I} + 2\eta\dot{\boldsymbol{\varepsilon}} \tag{2.22}$$

$$\nabla^2 V = 4\pi G \delta\rho, \tag{2.23}$$

where in eq. (2.21), the reference gravity acceleration $\boldsymbol{g}_0 = -g_0 \boldsymbol{e}_r = -\operatorname{grad} V_0$ has been introduced. In the following, we will refer to the set of eqs (2.20)-(2.23) with boundary conditions (2.10), (2.11), (2.14) and (2.15) as the *Stokes-Poisson boundary-value problem*.

We expand the flow $\boldsymbol{u}$ and the traction vector $\boldsymbol{T} \equiv \boldsymbol{\tau} \cdot \boldsymbol{e}_r$ in vector spherical harmonics (Appendix A.1):

$$\boldsymbol{u} = \sum_{jm} (u_{jm} \boldsymbol{S}_{jm}^{(-1)} + v_{jm} \boldsymbol{S}_{jm}^{(1)} + w_{jm} \boldsymbol{S}_{jm}^{(0)}), \tag{2.24}$$

$$\boldsymbol{T} = \sum_{jm} (\tau_{rr,jm} \boldsymbol{S}_{jm}^{(-1)} + \tau_{r\vartheta,jm} \boldsymbol{S}_{jm}^{(1)} + \tau_{r\varphi,jm} \boldsymbol{S}_{jm}^{(0)}), \tag{2.25}$$

where u_{jm} and v_{jm} are the spheroidal components and w_{jm} the toroidal component of $\boldsymbol{u}$. It is important to observe (e.g. Ricard et al., 1984), that if the viscosity in eqs (2.21)-(2.22) does not depend on Ω, the problem is greatly simplified because spheroidal and toroidal flow are independent and spherical harmonic modes are fully decoupled, with the consequence that the problem (2.20)-(2.23) can be solved independently for each harmonic degree j and order

m. For convenience, we relabel several variables, as follows:

$$y_1 \equiv u_{jm}, \tag{2.26}$$
$$y_2 \equiv v_{jm}, \tag{2.27}$$
$$y_3 \equiv \tau_{rr,jm}, \tag{2.28}$$
$$y_4 \equiv \tau_{r\vartheta,jm}, \tag{2.29}$$
$$y_7 \equiv w_{jm}, \tag{2.30}$$
$$y_8 \equiv \tau_{r\varphi,jm}. \tag{2.31}$$

Note that the new labeling is simply for convenience and y_5 and y_6 variables will be introduced shortly later. Expressing the divergence in terms of spherical harmonics (see eq. A.18), eq. (2.20) reads as

$$\frac{dy_1}{dr} = -\frac{2y_1}{r} + \frac{Jy_2}{r}, \tag{2.32}$$

where $J \equiv j(j+1)$. In Appendix B, we report the expression of the components of the strain rate tensor in spherical coordinates. Using the constitutive equation (2.22) it can be shown that

$$y_3 = -p_{jm} + 2\eta\frac{dy_1}{dr}, \tag{2.33}$$
$$\frac{dy_2}{dr} = -\frac{y_1}{r} + \frac{y_2}{r} + \frac{y_4}{\eta}, \tag{2.34}$$
$$\frac{dy_7}{dr} = \frac{y_7}{r} + \frac{y_8}{\eta} \tag{2.35}$$

In Appendix B, the spherical harmonic expansion of the divergence of the stress tensor can also be found. Using eqs (2.32) and (2.33), we have:

$$(\operatorname{div}\boldsymbol{\tau})_{r,jm} = \left(\frac{dy_3}{dr} - \frac{12\eta}{r^2}y_1 + \frac{6J\eta}{r^2}y_2 - \frac{J}{r}y_4\right)Y_{jm}, \tag{2.36}$$
$$\begin{aligned}(\operatorname{div}\boldsymbol{\tau})_{\vartheta,jm} = &\left(\frac{dy_4}{dr} + \frac{6\eta}{r^2}y_2 + \frac{2\eta(1-2J)}{r^2}y_2 + \frac{1}{r}y_3 + \frac{3}{r}y_4\right)\frac{\partial Y_{jm}}{\partial\vartheta} \\ &- \left(\frac{dy_8}{dr} - \frac{\eta(J-2)}{r^2}y_7 + \frac{3}{r}y_8\right)\frac{1}{\sin\vartheta}\frac{\partial Y_{jm}}{\partial\varphi},\end{aligned} \tag{2.37}$$
$$\begin{aligned}(\operatorname{div}\boldsymbol{\tau})_{\varphi,jm} = &\left(\frac{dy_4}{dr} + \frac{6\eta}{r^2}y_2 + \frac{2\eta(1-2J)}{r^2}y_2 + \frac{1}{r}y_3 + \frac{3}{r}y_4\right)\frac{1}{\sin\vartheta}\frac{\partial Y_{jm}}{\partial\varphi} \\ &+ \left(\frac{dy_8}{dr} - \frac{\eta(J-2)}{r^2}y_7 + \frac{3}{r}y_8\right)\frac{\partial Y_{jm}}{\partial\vartheta}.\end{aligned} \tag{2.38}$$

From eqs (2.36)-(2.38), it is evident that spheroidal and toroidal flow are decoupled. Therefore, introducing the vector of the toroidal variables $\boldsymbol{y}_{\mathrm{T}} \equiv [y_7, y_8]^t$ and using eqs (2.35), (2.37) and (2.38), we can write the following system of linear equations:

$$\frac{d\boldsymbol{y}_{\mathrm{T}}}{dr} = \boldsymbol{B}\,\boldsymbol{y}_{\mathrm{T}}, \tag{2.39}$$

where we have defined the matrix $\boldsymbol{B}$ as follows:

$$\boldsymbol{B} \equiv \begin{pmatrix} \dfrac{1}{r} & \dfrac{1}{\eta} \\ \dfrac{(J-2)\eta}{r^2} & -\dfrac{3}{r} \end{pmatrix}.$$

It is important to note that, since neither a toroidal forcing nor boundary conditions for toroidal flow are prescribed, the vector $\boldsymbol{y}_{\mathrm{T}}$ satisfies a homogeneous system with homogeneous boundary conditions for each j and m. Hence, it has only the trivial solution $\boldsymbol{y}_{\mathrm{T}} = 0$. However, although models with radial symmetric viscosity structure predict spheroidal motion only, it must be emphasized that for the real Earth, toroidal motion is definitely not negligible. In fact, the observed toroidal/spheroidal ratio is close to unity (O'Connell et al., 1991). Significant efforts have been made to generate toroidal motion either by including lateral variations in viscosity and non-Newtonian rheologies (Christensen & Harder, 1991; Čadek et al., 1993; Zhang & Christensen, 1993; Ribe, 1992; Wen & Anderson, 1997), or by imposing toroidal motion of plates as a boundary condition, regardless of the origin of plate toroidal velocities (Ricard & Vigny, 1989; Lithgow-Bertelloni & Richards, 1995).

Potential V and density anomalies $\delta\rho$ must also be expanded into spherical harmonics:

$$V = \sum_{jm} V_{jm} Y_{jm}, \tag{2.40}$$

$$\delta\rho = \sum_{jm} \delta\rho_{jm} Y_{jm}. \tag{2.41}$$

The potential V_{jm} and the gravity dV_{jm}/dr are used to introduce the following new variables:

$$y_5 \equiv r V_{jm}, \tag{2.42}$$

$$y_6 \equiv r^2 \frac{dV_{jm}}{dr} = r^2 \frac{dy_5}{dr}. \tag{2.43}$$

With these definitions, we can express the gradient of the potential in terms of vector spherical harmonics as follows:

$$\operatorname{grad} V = \sum_{jm} \left(\frac{dV_{jm}}{dr} \boldsymbol{S}^{(-1)}_{jm} + \frac{V_{jm}}{r} \boldsymbol{S}^{(1)}_{jm} \right) = \sum_{jm} \left(\frac{y_6}{r^2} \boldsymbol{S}^{(-1)}_{jm} + \frac{y_5}{r^2} \boldsymbol{S}^{(1)}_{jm} \right). \tag{2.44}$$

Equation (2.23) in spherical coordinates reads as

$$\frac{\partial^2 V}{\partial r^2} + \frac{2}{r}\frac{\partial V}{\partial r} + \frac{1}{r^2 \sin\vartheta}\frac{\partial}{\partial \vartheta}\left(\sin\frac{\partial V}{\partial \vartheta} \right) + \frac{1}{r^2 \sin\vartheta}\frac{\partial^2 V}{\partial \varphi^2} = 4\pi G \delta\rho. \tag{2.45}$$

Using the fact that spherical harmonics are eigenfunctions of the angular part of the Laplace operator, i.e.:

$$\frac{1}{\sin\vartheta}\frac{\partial}{\partial \vartheta}\left(\sin\frac{\partial Y_{jm}}{\partial \vartheta} \right) + \frac{1}{\sin\vartheta}\frac{\partial^2 Y_{jm}}{\partial \varphi^2} = -J Y_{jm}, \tag{2.46}$$

eq. (2.45) becomes:

$$\frac{\partial^2 V}{\partial r^2} + \frac{2}{r}\frac{\partial V}{\partial r} - \frac{J}{r^2}V = 4\pi G\delta\rho. \tag{2.47}$$

Using definitions (2.42) and (2.43) and eq. (2.47), we can readily show that y_5 and y_6 satisfy the following linear differential equations:

$$\frac{dy_5}{dr} = -\frac{y_5}{r} + \frac{y_6}{r}, \tag{2.48}$$

$$\frac{dy_6}{dr} = \frac{J}{r}y_5 + 4\pi G r^2 \delta\rho_{jm}. \tag{2.49}$$

Combining now eqs (2.36) and (2.44), we can write the radial component of the Stokes equation (2.21) as

$$\frac{dy_3}{dr} = \frac{12\eta}{r^2}y_1 - \frac{6\eta J}{r^2}y_2 + \frac{J}{r}y_4 - \frac{\rho_0}{r^2}y_6 + g_0\delta\rho_{jm}, \tag{2.50}$$

while, combining eqs (2.37) and (2.44), we obtain for the ϑ-component:

$$\frac{dy_4}{dr} = -\frac{6\eta}{r^2}y_1 - \frac{2\eta(1-2J)}{r^2}y_2 - \frac{y_3}{r}y_4 - \frac{3}{r}y_4 - \frac{\rho_0}{r^2}y_5. \tag{2.51}$$

By collecting the spheroidal variables, the potential and its derivative into the vector $\boldsymbol{y} \equiv [y_1, y_2, y_3, y_4, y_5, y_6]^t$, from eqs (2.32), (2.34), (2.50), (2.51), (2.48), (2.49), we can write in a compact form the following system of linear equations:

$$\frac{d\boldsymbol{y}}{dr} = \boldsymbol{A}\,\boldsymbol{y} + \boldsymbol{b}, \tag{2.52}$$

where $\boldsymbol{A}$ is the matrix of the system:

$$\boldsymbol{A} \equiv \begin{pmatrix} -\frac{2}{r} & \frac{J}{r} & 0 & 0 & 0 & 0 \\ -\frac{1}{r} & \frac{1}{r} & 0 & \frac{1}{\eta} & 0 & 0 \\ \frac{12\eta}{r^2} & -\frac{6J\eta}{r^2} & 0 & \frac{J}{r} & 0 & -\frac{\rho_0}{r^2} \\ -\frac{6\eta}{r^2} & -\frac{2\eta(1-2J)}{r^2} & -\frac{1}{r} & -\frac{3}{r} & -\frac{\rho_0}{r^2} & 0 \\ 0 & 0 & 0 & 0 & \frac{1}{r} & \frac{1}{r} \\ 0 & 0 & 0 & 0 & \frac{J}{r} & 0 \end{pmatrix}, \tag{2.53}$$

and $\boldsymbol{b}$ is the forcing vector:

$$\boldsymbol{b} = [0, 0, g_0\delta\rho_{jm}r^2, 0, 0, 4\pi G\delta\rho_{jm}r^3]^t.$$

For each degree and order j and m, the system (2.52) is equivalent to eqs (2.20)-(2.23) (with the assumption that $\eta = \eta(r)$).

2.4 Matrix propagator

If the solution to eq. (2.52) is known at an initial radius r_0, the solution corresponding to a radius $r > r_0$, enclosing a shell in which the matrix $\boldsymbol{A}$ is constant, can be obtained (Gantmacher, 1990) through the *matrix propagator* (or simply *propagator*) $\boldsymbol{P}$ as follows:

$$\boldsymbol{y}(r) = \boldsymbol{P}(r, r_0)\boldsymbol{y}(r_0) + \int_{r_0}^{r} \boldsymbol{P}(r, \xi)\boldsymbol{b}(\xi)d\xi. \tag{2.54}$$

Here $\boldsymbol{y}(r_0)$ is a known starting vector and $\boldsymbol{P}(r, r_0)$ is the propagator matrix that propagates this starting solution and the load vector $\boldsymbol{b}$ up to the new radius r. For the matrix $\boldsymbol{A}$, an analytical form of the propagator $\boldsymbol{P}$ can be obtained in two ways. One possibility is to derive first the fundamental matrix $\boldsymbol{M}(r)$ for which the solution to the homogeneous system associated with eq. (2.52) (with $\boldsymbol{b} = 0$) can be written as

$$\boldsymbol{y}(r) = \boldsymbol{M}(r)\boldsymbol{c},$$

where $\boldsymbol{c}$ is a vector of six unknown constants of integration. The matrix $\boldsymbol{M}$ can be determined analytically by looking for solutions of the homogeneous system of the following type: $y_1 = c_1 r^k$, $y_2 = c_2 r^k$, $y_3 = c_3 r^{k-1}$, $y_4 = c_4 r^{k-1}$, $y_5 = c_5 r^k$ and $y_6 = c_6 r^k$. Once $\boldsymbol{M}$ is known, it can be shown (Gilbert & Backus, 1966) that the propagator $\boldsymbol{P}$ has the following form:

$$\boldsymbol{P}(r, r_0) = \boldsymbol{M}(r)\boldsymbol{M}^{-1}(r_0),$$

where $\boldsymbol{M}^{-1}$ is the inverse of $\boldsymbol{M}$. Alternatively, as shown by Gantmacher (1990), $\boldsymbol{P}$ can be determined with the eigenvalue method:

$$\boldsymbol{P}(r, r_0) = \sum_{i=1}^{N} e^{\lambda_i (r - r_0)} \prod_{s \neq i} \frac{\lambda_s \boldsymbol{I} - \boldsymbol{A}}{\lambda_s - \lambda_i},$$

where λ_i are the N eigenvalues of $\boldsymbol{A}$ and $\boldsymbol{I}$ is the identity matrix.

Equation (2.54) can be further simplified if the continuous volumetric density perturbations $\delta\rho_{jm}(r)$ are approximated by a series of N discrete sheets of surface-mass anomaly $\delta\sigma_{jm}(r_i)$ located at fixed depths r_i. In this case, the integral in eq. (2.54) can be replaced by a summation:

$$\boldsymbol{y}(r) = \boldsymbol{P}(r, r_0)\boldsymbol{y}(r_0) + \sum_{i=1}^{N} \boldsymbol{P}(r, r_i)\boldsymbol{b}(r_i), \tag{2.55}$$

where the load vector now reads as

$$\boldsymbol{b} = [0, 0, g_0 \delta\sigma_{jm}(r_i) r_i, 0, 0, 4\pi G \delta\sigma_{jm}(r_i) r_i^2]^t.$$

Equation (2.55) is only valid within a layer where the propagator is constant. At any boundary within the mantle, continuity and force balance require that $\boldsymbol{u}$,

$\boldsymbol{\tau}$ and V are continuous. If we assume that the background reference density is constant, only one type of internal boundary can be found, namely the interface between two layers of different viscosity (but the same intrinsic density). At such boundaries, the continuity of flow, stresses and potential is implicitly guaranteed and, consequently, only $\boldsymbol{P}$ changes. To account for radial changes of viscosity, and consequent changes in the propagator, a property of the propagator matrix can be used where the solution vectors can be propagated through a series of different material layers by simply forming the product of individual layer matrices. That is, if we consider for instance two shell layers bounded by the radii (r_1, r_2) and (r_2, r_3) respectively, the propagator $\boldsymbol{P}(r_1, r_3)$ for the double layer (r_1, r_3) is given by the product $\boldsymbol{P}(r_1, r_2)\boldsymbol{P}(r_2, r_3)$.

Finally, we need to treat the boundary conditions at the Earth's surface and at the CMB. Conditions (2.10) and (2.11) require that $y_1 = y_3 = 0$ at $r = a$ and $r = c$. According to eq. (2.18), just above the Earth's surface ($r = a^+$), the potential is

$$V^{a^+}(a, \Omega) = \sum_{jm} V_{jm}^{a^+} Y_{jm}(\Omega), \tag{2.56}$$

and its derivative is

$$\frac{\partial V^{a^+}}{\partial r}(a, \Omega) = -\sum_{jm} \frac{j+1}{a} V_{jm}^{a^+} Y_{jm}(\Omega). \tag{2.57}$$

Analogously, just beneath the CMB ($r = c^-$), according to eq. (2.19), we have

$$V^{c^-}(c, \Omega) = \sum_{jm} V_{jm}^{c^-} Y_{jm}(\Omega) \tag{2.58}$$

and

$$\frac{\partial V^{c^-}}{\partial r}(c, \Omega) = \sum_{jm} \frac{j}{c} V_{jm}^{c^-} Y_{jm}(\Omega). \tag{2.59}$$

Since the potential must be continuous across $r = a$ and $r = c$ (eq. 2.14), we can simply write $V_{jm}^{a^+} = V_{jm}(a)$ and $V_{jm}^{c^-} = V_{jm}(c)$. According to eq. (2.12) and the definition (2.33), the coefficients of the surface-mass density associated with the dynamic topography are given by y_3/g_0. Hence, taking into account the condition (2.15) and the definition (2.42), the solution vector $\boldsymbol{y}$ at the surface reads

$$\boldsymbol{y}(a) = \left[0, y_2(a), y_3(a), 0, \frac{y_5(a)}{a}, -(j+1)\frac{y_5(a)}{a} + \frac{4\pi G a^2 y_3(a)}{g_0}\right]^t, \tag{2.60}$$

while at the CMB, we have

$$\boldsymbol{y}(c) = \left[0, y_2(c), y_3(c), 0, \frac{y_5(c)}{c}, j\frac{y_5(c)}{c} + \frac{4\pi G c^2 y_3(c)}{g_0}\right]^t. \tag{2.61}$$

Using eq. (2.55) with the boundary vectors (2.60) and (2.61) leads to solving a system of six equations in the six unknowns $y_2(a)$, $y_3(a)$, $y_5(a)$, $y_2(c)$, $y_3(c)$, $y_5(c)$. With this procedure, the starting solution $\boldsymbol{y}(c)$ is fully specified and can be propagated, using eq. (2.55), to any additional radius.

CHAPTER 3

Spectral finite element approach

When mantle viscosity is not simply radially distributed but exhibits lateral variations, the matrix propagator solution for individual degrees and orders is no longer applicable. To be able to treat lateral viscosity variations (LVV), we apply the finite element method to find the solution of the Stokes-Poisson problem. In this chapter we show how to reformulate the problem in a weak sense and prove that such formulation is equivalent to the traditional strong one. The resulting integral equations are parameterized using spherical harmonic functions for the angular coordinates and piecewise linear finite elements to discretize the radial coordinate. This is the reason why we call our method the *spectral finite element approach*.

3.1 Models with lateral viscosity variations

From the computational point of view, the matrix propagator technique is an extremely efficient tool. For a given viscosity stratification, it allows us to calculate the analytical solution of the Stokes-Poisson problem very quickly. This has made it the principal method that has been employed during the past two decades for the inversion of geophysical data (geoid, gravity, dynamic topography and plate motions) in terms of radial distributions of mantle viscosity (King, 1995b; Thoraval & Richards, 1997; Panasyuk & Hager, 2000). However, it is widely accepted that the Earth's mantle presents strong LVV ranging from 1 to 4 or 5 orders of magnitude (Karato & Wu, 1993; King, 1995a). In the form that has been described in Chapter 2, the propagator technique is not applicable if LVV are to be taken into account. The introduction of LVV increases the mathematical complexity of the problem because, in this case, spherical harmonic modes are coupled with each other, with the consequence that a load of a given degree and order (j, m) produces a response over the whole spectrum and not only on that particular (j, m), as is the case for models where viscosity is laterally homogeneous.

Within the framework of methods based on spherical harmonics (*spectral methods*), a convenient way to account for LVV has been proposed by Zhang & Christensen (1993) that finds its foundation in perturbation theory. After reducing the set of partial differential equations to a system of ordinary differential equations (as was done to derive eq. (2.52)), the problem of mode-coupling can be solved iteratively by adding, for each degree and order, a 'viscous-load' term to the right hand side of the linear system. This term arises from deviations of the viscosity from its radially-averaged value and contains contributions from all the harmonic modes that can be obtained from the previous iteration step. By suitably scaling the primitive variables, this technique permits the treatment of lateral viscosity contrasts up to a factor of a little over 10^3. The major advantage of Zhang and Christensen's method is probably its speed. In the presence of relatively moderate viscosity contrasts, the method is known to converge very fast and does not require particularly sophisticated computational facilities. Because of that, it represents a very attractive tool, even when inversion for viscosity structures with LVV are sought (Čadek & Fleitout, 2003). On the other hand, it is suited for treating LVV only of relatively long wavelengths and, more importantly, when the viscosity exhibits more pronounced jumps (stronger than $10^3 - 10^4$), iterations are unlikely to converge.

An alternative to the technique described above is the finite element method (FEM). Because of its ability to provide reliable solutions to problems with strong discontinuities in the driving forces and material properties, FEM has become a widespread computational tool to model convection in the Earth's interior in Cartesian and spherical geometries (Christensen, 1984; Baumgardner, 1985; King et al., 1990; Moresi & Solomatov, 1995; Zhong et al., 2000; Tan et al., 2006). Although traditionally FEM codes have been employed mostly to perform numerical experiments of time-dependent thermal convection, they have also been used to predict surface observables. For instance, Zhong & Davies (1999) modeled the long-wavelength geoid with a highly resolved 3-D viscosity structure that takes into account the presence of stiff subducted slabs in the whole mantle, while Moresi & Solomatov (1995) presented a regional fully 3-D model of the geoid over the Western Pacific subduction zone. However, especially for global problems where the whole mantle must be considered, purely FEM codes, despite their ability to guarantee high accuracy, robustness and flexibility, are known for high computational demands and are often designed to work on parallel computers, making them very inconvenient (when not impossible) to run on traditional sequential machines when a high resolution is needed. Moreover, from the computational viewpoint, the use of simplified laterally homogeneous viscosity models does not present any advantage in purely FEM codes, as is the case for spectral methods.

The spectral-finite element approach (SFE) that we are presenting represents a compromise between the purely spectral perturbation method and the purely finite element method. A similar approach has been applied to model the Earth's electromagnetic induction (Martinec, 1999) with 3-D electrical conductivity, the viscoelastic relaxation with 3-D viscosity (Martinec, 2000) and the Stokes prob-

lem for non-Newtonian rheologies (Čadek et al., 1992, 1993). Moucha et al. (2007) make use of a formulation similar to ours, but choose orthogonal trigonometric functions instead of finite elements to parameterize the radial variable. On the one hand, the use of a weak formulation - typical of the finite element approach - guarantees high flexibility, easiness to modify the code and the possibility to consider strong lateral discontinuities in viscosity that could hardly be treated with an iterative technique. The use of spherical harmonics makes the solution spectrum readily available, which is a great advantage, especially when dealing with the Earth's gravity field. Furthermore, the orthogonality properties of spherical harmonics assure extremely rapid solutions when LVV are partly or completely absent. On the other hand, as it happens with all spectrally-based methods, Gibbs oscillations (Walker, 1988) are likely to appear in the presence of sharp viscosity jumps, which then need to be smoothed, and the integrals that arise from mode-coupling have complicated expressions and demand rather long computational times. Moreover, spherical harmonics, that will be employed to parameterize the angular part of the solution, are base functions with global support. The consequence of such a property is that local lateral mesh densification is not possible, as it is with purely FEM codes. Although a better lateral resolution might be needed only locally, with the SFE approach only a global refinement is feasible.

3.2 Weak formulation of the Stokes problem

In Chapter 2, we introduced the Stokes-Poisson boundary-value problem consisting of a set of partial differential equations (eqs 2.20-2.23) subject to a set of boundary conditions (eqs 2.10, 2.11, 2.14, 2.15). This is the classical (or *strong*) formulation of the problem. Its solution, which must exist locally everywhere within the solution domain, can be generalized through an equivalent integral (or *weak*) formulation, which has the property that the solution may exist even though the strong solution does not (Křižek & Neittaanmäki, 1990). We derive first a weak formulation for the Stokes problem without self-gravitation ($\rho_0 \mathrm{grad}\, V = 0$ in eq. 2.21). In the following sections, we will add the weak form of the Poisson equation and show how the self-gravitation term can be incorporated.

Let us introduce the functional space

$$\mathcal{V} \equiv \{\boldsymbol{u} \in \mathcal{W}_1^2(\mathcal{B});\, p \in \mathcal{L}^2(\mathcal{B});\, \lambda \in \mathcal{L}^2(\partial\mathcal{B})\}. \tag{3.1}$$

Here, $\mathcal{L}^2(\mathcal{B})$ and $\mathcal{L}^2(\partial\mathcal{B})$ are the space of square integrable functions in the solution domain $\mathcal{B}$ (the mantle volume) and on its boundary $\partial\mathcal{B}$ (the Earth's surface plus the CMB), respectively, and $\mathcal{W}_1^2(\mathcal{B})$ is the Sobolev space of vector functions in $\mathcal{B}$, i.e.

$$\mathcal{W}_1^2(\mathcal{B}) \equiv \{\boldsymbol{u} \in \mathcal{L}^2(\mathcal{B}),\, \mathrm{grad}\, \boldsymbol{u} \in \mathcal{L}^2(\mathcal{B})\}.$$

In order to satisfy the incompressibility constraint (2.20) and boundary conditions (2.10) and (2.11), we use the method of *Lagrange multipliers* (in the

finite-element literature, the term *penalty formulation* (Hughes, 1987) is often used with an equivalent meaning). In fact, in expression (3.1), besides the primitive variable $\boldsymbol{u}$, the non-hydrostatic pressure p along with the new variable λ also play the role of Lagrange multipliers (Matyska, 1996).

Within the functional space $\mathcal{V}$, we introduce the *energy functional*

$$\mathscr{E}(\boldsymbol{u}, p, \lambda) \equiv \mathscr{E}_{\dot{\varepsilon}}(\boldsymbol{u}) + \mathscr{E}_p(p) + \mathscr{E}_\lambda(\lambda) \tag{3.2}$$

where

$$\mathscr{E}_{\dot{\varepsilon}}(\boldsymbol{u}) \equiv \int_{\mathcal{B}} \eta(\dot{\boldsymbol{\varepsilon}} : \dot{\boldsymbol{\varepsilon}})\, dV,$$
$$\mathscr{E}_p(p) \equiv -\int_{\mathcal{B}} p \operatorname{div} \boldsymbol{u}\, dV,$$
$$\mathscr{E}_\lambda(\lambda) \equiv -\int_{\partial\mathcal{B}} \lambda\, \boldsymbol{e}_r \cdot \boldsymbol{u}\, dS,$$

and the *forcing functional*

$$\mathscr{F}(\boldsymbol{u}) \equiv \int_{\mathcal{B}} \boldsymbol{f} \cdot \boldsymbol{u}\, dV, \tag{3.3}$$

where $\boldsymbol{f} \equiv -\boldsymbol{g}_0 \delta\rho$. Each term of the functionals (3.2) and (3.3) has a physical meaning: The term $\mathscr{E}_{\dot{\varepsilon}}$ is a measure of the dissipative energy of the system, the term $\mathscr{E}_p$ allows us to adjust the incompressibility constraint through the Lagrange multiplier p and the term $\mathscr{E}_\lambda$ enforces the boundary conditions through the Lagrange multiplier λ. The functional $\mathscr{F}$ is the power of the buoyancy forces that induce the flow.

The *Gâteaux* (or *variational*) *derivative* of a functional $F(x)$ is defined as follows (e.g. Gelfand & Fomin, 1963):

$$\delta F(x, \delta x) \equiv \frac{d}{dt} F(x + t\,\delta x)\bigg|_{t=0},$$

where δF is the *first variation* (or simply *variation*) of F and δx are so called *test functions*. Thus, denoting by $\delta\boldsymbol{u}$, δp and $\delta\lambda$ the test functions corresponding to $\boldsymbol{u}$, p and λ, respectively, the Gâteaux derivatives of the functionals (3.2) and (3.3) read

$$\begin{aligned}\delta\mathscr{E}(\boldsymbol{u}, p, \lambda, \delta\boldsymbol{u}, \delta p, \delta\lambda) =& \delta\mathscr{E}_{\dot{\varepsilon}}(\boldsymbol{u}, \delta\boldsymbol{u}) + \delta\mathscr{E}_p(\boldsymbol{u}, p, \delta\boldsymbol{u}, \delta p) \\ &+ \delta\mathscr{E}_\lambda(\boldsymbol{u}, \lambda, \delta\boldsymbol{u}, \delta\lambda),\end{aligned} \tag{3.4}$$

where

$$\delta\mathscr{E}_{\dot{\varepsilon}} = 2\int_{\mathcal{B}} \eta(\dot{\boldsymbol{\varepsilon}} : \delta\dot{\boldsymbol{\varepsilon}})\, dV, \tag{3.5}$$

$$\delta\mathscr{E}_p = -\int_{\mathcal{B}} \operatorname{div} \boldsymbol{u}\, \delta p\, dV - \int_{\mathcal{B}} p \operatorname{div} \delta\boldsymbol{u}\, dV, \tag{3.6}$$

$$\delta\mathscr{E}_\lambda = -\int_{\partial\mathcal{B}} \boldsymbol{e}_r \cdot \boldsymbol{u}\, \delta\lambda\, dS - \int_{\partial\mathcal{B}} \lambda\, \boldsymbol{e}_r \cdot \delta\boldsymbol{u}\, dS, \tag{3.7}$$

and

$$\delta\mathscr{F}(\delta\boldsymbol{u}) = \int_{\mathcal{B}} \boldsymbol{f}\cdot\delta\boldsymbol{u}\,dV. \tag{3.8}$$

The *weak formulation* of the Stokes boundary-value problem (2.20)-(2.22), (2.10) and (2.11) consists of finding $(\boldsymbol{u}, p, \lambda) \in \mathcal{V}$ so that, for every possible choice of the test-functions $(\delta\boldsymbol{u}, \delta p, \delta\lambda) \in \mathcal{V}$, the variational equality

$$\delta\mathscr{E}(\boldsymbol{u}, p, \lambda, \delta\boldsymbol{u}, \delta p, \delta\lambda) = \mathscr{F}(\delta\boldsymbol{u}) \tag{3.9}$$

is satisfied.

The existence and uniqueness of the weak formulation of the Stokes has been extensively discussed by Matyska (1996). Nevertheless, it is interesting to show here the equivalence between the weak and classical solutions. To this purpose, we will make use of the Green's theorem, which is a generalization of the well-known divergence theorem. According to this theorem (Křižek & Neittaanmäki, 1990, Theorem 2.8), if Ω is a bounded domain with Lipschitz boundary $\partial\Omega$ and $v, w \in \mathcal{W}_2^1(\Omega)$, the following identity holds (*Green's identity*):

$$\int_\Omega w\frac{\partial v}{\partial x_j}\,dV = \int_{\partial\Omega} wvn_j\,dS - \int_\Omega v\frac{\partial w}{\partial x_j}\,dV, \tag{3.10}$$

where n_j is the j-th component of the unit outward normal to $\partial\Omega$. Being the hypothesis of such a theorem fulfilled, applying the identity (3.10) to eq. (3.5) and to the second term of eq. (3.6) yields

$$\int_{\mathcal{B}} \eta(\dot{\boldsymbol{\varepsilon}} : \delta\dot{\boldsymbol{\varepsilon}})dV = \int_{\partial\mathcal{B}} \eta\,\boldsymbol{e}_r\cdot\dot{\boldsymbol{\varepsilon}}\cdot\delta\boldsymbol{u}\,dS - \int_{\mathcal{B}} \operatorname{div}(\eta\,\dot{\boldsymbol{\varepsilon}})\cdot\delta\boldsymbol{u}\,dV, \tag{3.11}$$

$$\int_{\mathcal{B}} p\operatorname{div}\delta\boldsymbol{u}\,dV = \int_{\partial\mathcal{B}} p\,\boldsymbol{e}_r\cdot\delta\boldsymbol{u}\,dS - \int_{\mathcal{B}} \operatorname{grad} p\cdot\delta\boldsymbol{u}\,dV. \tag{3.12}$$

Upon substituting eqs (3.11) and (3.12) into the variational equality (3.9), we obtain

$$\begin{aligned}\delta\mathscr{E} - \delta\mathscr{F} = &-\int_{\mathcal{B}} [-\operatorname{grad} p + \operatorname{div}(2\eta\dot{\boldsymbol{\varepsilon}}) + \boldsymbol{f}]\cdot\delta\boldsymbol{u}\,dV - \int_{\mathcal{B}} \operatorname{div}\boldsymbol{u}\,\delta p\,dV\\ &+\int_{\partial\mathcal{B}} (-p\boldsymbol{I} + 2\eta\dot{\boldsymbol{\varepsilon}})\cdot\boldsymbol{e}_r\cdot\delta\boldsymbol{u}\,dS - \int_{\partial\mathcal{B}} \lambda\boldsymbol{e}_r\cdot\delta\boldsymbol{u}\,dS\\ &-\int_{\partial\mathcal{B}} \boldsymbol{u}\cdot\boldsymbol{e}_r\,\delta\lambda\,dS,\end{aligned}$$

which, using the stress tensor $\boldsymbol{\tau}$, is equivalent to the following identity:

$$\begin{aligned}&-\int_{\mathcal{B}} (\operatorname{div}\boldsymbol{\tau} + \boldsymbol{f})\cdot\delta\boldsymbol{u}\,dV - \int_{\mathcal{B}} \operatorname{div}\boldsymbol{u}\,\delta p\,dV\\ &-\int_{\partial\mathcal{B}} \boldsymbol{u}\cdot\boldsymbol{e}_r\,\delta\lambda\,dS + \int_{\partial\mathcal{B}} (\boldsymbol{\tau}\cdot\boldsymbol{e}_r - \lambda\boldsymbol{e}_r)\cdot\delta\boldsymbol{u}\,dS = 0.\end{aligned} \tag{3.13}$$

For a function $f \in \mathcal{L}^2(\mathcal{B})$ and test functions $v \in \mathcal{C}_0^\infty(\mathcal{B})$, where $\mathcal{C}_0^\infty(\mathcal{B})$ is the space of infinitely differentiable functions with compact support in $\mathcal{B}$, the following implication holds (Křižek & Neittaanmäki, 1990):

$$\int_{\mathcal{B}} f\, v\, dV = 0 \;\; \forall v \in \mathcal{C}_0^\infty(\mathcal{B}) \Longrightarrow f = 0 \;\text{ in } \mathcal{B}. \tag{3.14}$$

A similar statement is valid for a function $g \in \mathcal{L}^2(\partial\mathcal{B})$ and test functions $v \in \mathcal{C}_0^\infty(\bar{\mathcal{B}})$, where $\bar{\mathcal{B}}$ is the closure of $\mathcal{B}$:

$$\int_{\partial\mathcal{B}} g\, v\, dS = 0 \;\; \forall v \in \mathcal{C}_0^\infty(\bar{\mathcal{B}}) \Longrightarrow g = 0 \;\text{ on } \partial\mathcal{B}. \tag{3.15}$$

Taking the test functions $(\delta\boldsymbol{u}, \delta p) \in \mathcal{C}_0^\infty(\mathcal{B})$, because of (3.14), the first two terms of eq. (3.13) yield the Stokes equation (2.21) and the incompressibility condition (2.20). Analogously, if we interpret the Lagrange multiplier λ as the radial traction acting on $\partial\mathcal{B}$, i.e.

$$\lambda \equiv \tau_{rr}\Big|_{\partial\mathcal{B}} = \boldsymbol{e}_r \cdot \boldsymbol{\tau} \cdot \boldsymbol{e}_r\Big|_{\partial\mathcal{B}}, \tag{3.16}$$

because of (3.15), the last two terms of (3.13) are equivalent to the impermeability and free-slip boundary condition (2.10) and (2.11), respectively.

We have proven that finding the solution to the classical Stokes problem is equivalent to finding the solution that satisfies the variational equation (3.9) for a suitable choice of the test functions. Later in this chapter, we show how eq. (3.9) can be discretized and reduced to a form that is convenient for implementation into a computer algorithm.

3.3 Weak formulation of the Poisson equation

So far, we have considered only the weak solution of the Stokes problem. In order to compute the gravitational potential, and hence the geoid, we will derive a weak formulation of the Poisson equation.

We consider first the simplified case in which the gravitational contribution to the potential due to boundary deformations is neglected. In this case, the boundary condition (2.15) is reduced to the continuity of the gravity:

$$[\boldsymbol{e}_r \cdot \operatorname{grad} V]_-^+ = 0. \tag{3.17}$$

Let us consider $V \in \mathcal{W}_1^2(\mathcal{B})$ and the following functionals:

$$\mathscr{G}(V) \equiv \frac{1}{2}\int_{\mathcal{B}} \operatorname{grad} V \cdot \operatorname{grad} V\, dV - \int_{\partial\mathcal{B}} \boldsymbol{e}_r \cdot \operatorname{grad} V^+\, V\, dS, \tag{3.18}$$

$$\mathscr{H}(V) \equiv 4\pi G \int_{\mathcal{B}} \delta\rho\, V\, dV, \tag{3.19}$$

where V^+ is the external potential with respect to the mantle boundary $\partial\mathcal{B}$ (see eqs 2.56-2.59). Note that the symbol $\delta\rho$ denotes density perturbations and must

not be confused with the functional variation or the test functions for which the prefix δ has also been used. Following the same strategy adopted in the previous chapter, we calculate the variational derivative of the functionals (3.18) and (3.19), obtaining

$$\delta\mathscr{G}(V,\delta V) = \int_{\mathcal{B}} \operatorname{grad} V \cdot \operatorname{grad} \delta V \, dV - \int_{\partial\mathcal{B}} \boldsymbol{e}_r \cdot \operatorname{grad} V^+ \, \delta V \, dS, \tag{3.20}$$

$$\delta\mathscr{H}(V,\delta V) = 4\pi G \int_{\mathcal{B}} \delta\rho \, \delta V \, dV. \tag{3.21}$$

The weak formulation of the Poisson equation (2.23), subject to boundary conditions (2.14) and (3.17), consists of finding $V \in \mathcal{W}_1^2(\mathcal{B})$ in such a way that, for every choice of the test functions $\delta V \in \mathcal{W}_1^2(\mathcal{B})$, the following variational equality is satisfied:

$$\delta\mathscr{G}(V,\delta V) = \delta\mathscr{H}(\delta V). \tag{3.22}$$

Since the hypotheses of the Green's theorem are fulfilled, applying the identity (3.10) to the first term of eq. (3.20) yields:

$$\int_{\mathcal{B}} \operatorname{grad} V \cdot \operatorname{grad} \delta V \, dV = \int_{\partial\mathcal{B}} \boldsymbol{e}_r \cdot \operatorname{grad} V \, \delta V \, dS - \int_{\mathcal{B}} \nabla^2 V \, \delta V \, dV. \tag{3.23}$$

Upon inserting eq. (3.23) into the equality (3.22), we obtain

$$-\int_{\mathcal{B}} (\nabla^2 V - 4\pi G\delta\rho) \, \delta V \, dV - \int_{\partial\mathcal{B}} [\boldsymbol{e}_r \cdot \operatorname{grad} V]^+_- \, \delta V \, dS = 0. \tag{3.24}$$

According to the implications (3.14) and (3.15), eq. (3.24) proves that the potential V that satisfies the identity (3.22) is a solution of the Poisson equation. We will shortly see that, although the condition (2.14) for the continuity of the potential does not appear in eq. (3.24), it will be later used explicitely (eq. 3.47).

3.4 Self-gravitation and boundary deflections

We have proven that the solution $(\boldsymbol{u}, p, \lambda)$ which satisfies the variational equality (3.9) is a solution of the Stokes problem in the non-selfgravitating case and that the solution V that satisfies eq. (3.22) is a solution of the Poisson equation, provided that the effect of boundary deflections is neglected. Through self-gravitation and deformation of boundaries, a direct coupling between the flow and the gravity potential is established. On the one hand, perturbations in the potential influence the flow through the term $\rho_0 \operatorname{grad} V$ in the Stokes equation, while on the other hand, the dynamic topography h (eq. 2.12), caused by the flow-induced tractions at the boundaries, generates additional density anomalies that contribute to the potential V via boundary condition (2.15).

Although it turns out not to be possible to find proper functionals whose variation takes into account consistently these two terms, it is a standard procedure to add directly the necessary missing terms to the functional variation itself. Self-gravitation can be included by adding to eq. (3.4) the functional

$$\delta\mathscr{E}_{sg} \equiv \int_{\mathcal{B}} \rho_0 \operatorname{grad} V \cdot \delta\boldsymbol{u}\, dV. \tag{3.25}$$

In this case, due to eq. (3.13) and implication (3.14), we have

$$-\int_{\mathcal{B}} (\operatorname{div}\boldsymbol{\tau} + \rho_0 \operatorname{grad} V - \delta\rho\boldsymbol{g}_0) \cdot \delta\boldsymbol{u}\, dV = 0,$$

which is equivalent to eq. (2.21). Furthermore, observing that $\sigma^h = \lambda/g_0$ (see eqs 2.13 and 3.16), the effect due to the deformation of the boundary $\partial\mathcal{B}$ is considered by adding the boundary integral

$$\frac{4\pi G}{g_0} \int_{\partial\mathcal{B}} \lambda\, \delta V\, dS$$

to eq. (3.20), so that because of eq. (3.24) and implication (3.15), it holds:

$$\int_{\partial\mathcal{B}} ([\boldsymbol{e}_r \cdot \operatorname{grad} V]^+_- + 4\pi G\sigma^h)\, \delta V\, dS = 0,$$

and the boundary condition (2.15) is also satisfied.

For the self-gravitating case and taking into account boundary deflections, the weak formulation of the Stokes-Poisson problem can be now summarized as follows: Find $(\boldsymbol{u}, p, \lambda) \in \mathcal{V}$ and $V \in \mathcal{W}^2_1(\mathcal{B})$ in such a way that, for a suitable choice of the test functions $(\delta\boldsymbol{u}, \delta p, \delta\lambda) \in \mathcal{V}$ and $\delta V \in \mathcal{W}^2_1(\mathcal{B})$, the following variational equalities are satisfied

$$\delta\mathscr{E}(\boldsymbol{u}, p, \lambda, V, \delta\boldsymbol{u}, \delta p, \delta\lambda, \delta V) = \delta\mathscr{F}(\delta\boldsymbol{u}), \tag{3.26a}$$
$$\delta\mathscr{G}(V, \lambda, \delta V, \delta\lambda) = \delta\mathscr{H}(\delta V), \tag{3.26b}$$

where $\delta\mathscr{E} = \delta\mathscr{E}_{\dot\varepsilon} + \delta\mathscr{E}_p + \delta\mathscr{E}_\lambda + \delta\mathscr{E}_{sg}$ and the functional variations read:

$$\delta\mathscr{E}_{\dot\varepsilon} = 2\int_{\mathcal{B}} \eta(\dot{\boldsymbol{\varepsilon}} : \delta\dot{\boldsymbol{\varepsilon}}) dV, \tag{3.27}$$

$$\delta\mathscr{E}_p = -\int_{\mathcal{B}} \operatorname{div}\boldsymbol{u}\, \delta p\, dV - \int_{\mathcal{B}} p \operatorname{div}\delta\boldsymbol{u}\, dV, \tag{3.28}$$

$$\delta\mathscr{E}_\lambda = -\int_{\partial\mathcal{B}} \boldsymbol{e}_r \cdot \boldsymbol{u}\, \delta\lambda\, dS - \int_{\partial\mathcal{B}} \lambda\, \boldsymbol{e}_r \cdot \delta\boldsymbol{u}\, dS, \tag{3.29}$$

$$\delta\mathscr{E}_{sg} = \int_{\mathcal{B}} \rho_0 \operatorname{grad} V \cdot \delta\boldsymbol{u}\, dV, \tag{3.30}$$

$$\delta\mathscr{F} = \int_{\mathcal{B}} \boldsymbol{f} \cdot \delta\boldsymbol{u}\, dV, \tag{3.31}$$

$$\begin{aligned}\delta\mathscr{G} = &\int_{\mathcal{B}} \operatorname{grad} V \cdot \operatorname{grad} \delta V \, dV + \frac{4\pi G}{g_0} \int_{\partial\mathcal{B}} \lambda \, \delta V \, dS \\ &- \int_{\partial\mathcal{B}} \boldsymbol{e}_r \cdot \operatorname{grad} V^+ \, \delta V \, dS,\end{aligned} \tag{3.32}$$

$$\delta\mathscr{H} = 4\pi G \int_{\mathcal{B}} \delta\rho \, \delta V \, dV. \tag{3.33}$$

3.5 Spherical harmonic approximation over angular coordinates

Equations (3.26) must be now parameterized. As anticipated above, we will use spherical harmonic expansions over the angular coordinates $\Omega = (\vartheta, \varphi)$. We approximate the angular dependence of the solution $(\boldsymbol{u}, p, \lambda, V)$ by a series of vector and scalar spherical harmonics, as follows:

$$\boldsymbol{u}(r,\Omega) = \sum_{jm} \left[u_{jm}(r) \boldsymbol{S}^{(-1)}_{jm}(\Omega) + v_{jm}(r) \boldsymbol{S}^{(1)}_{jm}(\Omega) + w_{jm}(r) \boldsymbol{S}^{(0)}_{jm}(\Omega) \right], \tag{3.34}$$

$$p(r,\Omega) = \sum_{jm} p_{jm}(r) Y_{jm}(\Omega), \tag{3.35}$$

$$\lambda(\Omega) = \sum_{jm} \lambda_{jm} Y_{jm}(\Omega), \tag{3.36}$$

$$V(r,\Omega) = \sum_{jm} V_{jm}(r) Y_{jm}(\Omega), \tag{3.37}$$

where the radius r is contained in the interval $[c, a]$ (where c and a are the radius of the CMB and the Earth's surface, respectively), $Y_{jm}(\Omega)$ are scalar spherical harmonics and $\boldsymbol{S}^{(\ell)}_{jm}(\Omega)$, $\ell = -1, 0, 1$ are vector spherical harmonics (Appendix A.1). Note that in eq. (3.36) there is no dependence on r because λ is only defined on the boundary.

In order to parameterize the left-hand side of eq. (3.26a), it is convenient to expand the strain-rate tensor into tensor spherical harmonics $\boldsymbol{Z}^{(\ell)}_{jm}$, $\ell = 1, \ldots, 6$ (see Appendix A.1 for their definition):

$$\begin{aligned}\dot{\boldsymbol{\varepsilon}}(r,\Omega) = \sum_{jm} \Bigg[&\frac{du_{jm}(r)}{dr} \boldsymbol{Z}^{(1)}_{jm}(\Omega) + \left(\frac{dv_{jm}(r)}{dr} - \frac{v_{jm}(r)}{r} + \frac{u_{jm}(r)}{dr} \right) \boldsymbol{Z}^{(2)}_{jm}(\Omega) \\ &+ \left(\frac{dw_{jm}(r)}{dr} - \frac{w_{jm}(r)}{r} \right) \boldsymbol{Z}^{(3)}_{jm}(\Omega) + \frac{w_{jm}(r)}{r} \boldsymbol{Z}^{(4)}_{jm}(\Omega) \\ &- \frac{1}{2rJ} (2u_{jm}(r) - J\, v_{jm}(r)) \boldsymbol{Z}^{(5)}_{jm}(\Omega) + \frac{v_{jm}(r)}{2r} \boldsymbol{Z}^{(6)}_{jm}(\Omega) \Bigg],\end{aligned} \tag{3.38}$$

where $J \equiv j(j+1)$. Test functions $\delta\boldsymbol{u}$, δp, $\delta\lambda$, δV and $\delta\dot{\boldsymbol{\varepsilon}}$ are parameterized in the same way, with the only difference that the complex conjugate version of the expansions is employed. Furthermore, density anomalies are also expanded in scalar spherical harmonics:

$$\delta\rho(r,\Omega) = \sum_{jm} \delta\rho_{jm}(r) Y_{jm}(\Omega). \tag{3.39}$$

Since in eq. (3.31) we have that $\boldsymbol{f} = -g_0 \boldsymbol{e}_r \delta\rho$, according to the definition of $\boldsymbol{S}^{(-1)}_{jm}$, we can parameterize the load in vector spherical harmonics as follows:

$$\boldsymbol{f}(r,\Omega) = -g_0 \sum_{jm} \delta\rho_{jm}(r) \boldsymbol{S}^{(-1)}_{jm}(\Omega). \tag{3.40}$$

For sake of brevity, in the following the dependences from the radius and angular variables will be omitted and always assumed to be those of eqs (3.34)-(3.40).

Let us start considering eq. (3.26a). The divergence of $\boldsymbol{u}$ and the gradient of V can be expressed as follows (Appendix A.1):

$$\operatorname{div}\boldsymbol{u} = \sum_{jm} \left(\frac{du_{jm}}{dr} + \frac{2}{r}\frac{du_{jm}}{dr} - \frac{Jv_{jm}}{r} \right) Y_{jm}, \tag{3.41}$$

$$\operatorname{grad} V = \sum_{jm} \left(\frac{dV_{jm}}{dr} \boldsymbol{S}^{(-1)}_{jm} + \frac{V_{jm}}{r} \boldsymbol{S}^{(1)}_{jm} \right). \tag{3.42}$$

For the moment, we restrict ourselves to the case in which the viscosity is only radially dependent, i.e. $\eta = \eta(r)$ (the case of fully 3-D viscosity will be treated later). In such a case, the orthogonality properties of tensor spherical harmonics (Appendix A.1) greatly simplify the treatment of the problem, ensuring the complete decoupling of spherical harmonic modes. Let us consider for instance the angular integration of the first term of eq. (3.27). According to the parameterization (3.38) of the strain-rate tensor (and the corresponding test function), this is:

$$\begin{aligned} &2\int_c^a \int_\Omega \eta \sum_{jm} \sum_{j'm'} \frac{du_{jm}}{dr} \frac{d\delta u^*_{j'm'}}{dr} \boldsymbol{Z}^{(1)}_{jm} : \boldsymbol{Z}^{(1)*}_{j'm'} \, r^2 dr d\Omega \\ &= 2\int_c^a \eta \sum_{jm} \frac{du_{jm}}{dr} \frac{d\delta u^*_{jm}}{dr} \, r^2 dr, \end{aligned}$$

where the asterisk denotes complex conjugation and the orthogonality relation (A.37) has been used. Proceeding in a similar fashion, it can be shown that the

functionals (3.27)-(3.33) take the following form:

$$\begin{aligned}\delta\mathscr{E}_{\tilde{\varepsilon}} = \sum_{jm}\int_c^a \eta\Bigg[&2\frac{du_{jm}}{dr}\frac{d\delta u^*_{jm}}{dr}\\ &+ J\left(\frac{dv_{jm}}{dr}-\frac{v_{jm}}{dr}+\frac{u_{jm}}{r}\right)\left(\frac{d\delta v^*_{jm}}{dr}-\frac{\delta v^*_{jm}}{dr}+\frac{\delta u^*_{jm}}{r}\right)\\ &+ J\left(\frac{dw_{jm}}{dr}-\frac{w_{jm}}{dr}\right)\left(\frac{d\delta w^*_{jm}}{dr}-\frac{\delta w^*_{jm}}{dr}\right)+\frac{J(J-2)}{r^2}w_{jm}\delta w^*_{jm}\\ &+\frac{1}{r^2}(2u_{jm}-Jv_{jm})(2\delta u^*_{jm}-J\delta v^*_{jm})+\frac{J(J-2)}{r^2}v_{jm}\delta v^*_{jm}\Bigg]r^2dr,\end{aligned} \tag{3.43}$$

$$\begin{aligned}\delta\mathscr{E}_p = \sum_{jm}\int_c^a \Bigg[&\left(\frac{du_{jm}}{dr}+\frac{2}{r}u_{jm}-\frac{J}{r}v_{jm}\right)\delta p^*_{jm}\\ &+p_{jm}\left(\frac{d\delta u^*_{jm}}{dr}+\frac{2}{r}\delta u^*_{jm}-\frac{J}{r}\delta v^*_{jm}\right)\Bigg]r^2dr,\end{aligned} \tag{3.44}$$

$$\begin{aligned}\delta\mathscr{E}_\lambda = \sum_{jm}\big(&a^2\,u_{jm}(a)\delta\lambda^{a*}_{jm}+c^2\,u_{jm}(c)\delta\lambda^{c*}_{jm}\\ &+a^2\,\lambda^a_{jm}\delta u^*_{jm}(a)+c^2\,\lambda^c_{jm}\delta u^*_{jm}(c)\big),\end{aligned} \tag{3.45}$$

$$\delta\mathscr{E}_{sg} = \rho_0\sum_{jm}\int_c^a\left(\frac{dV_{jm}}{dr}\delta u^*_{jm}+\frac{J}{r}V_{jm}\delta v^*_{jm}\right)r^2dr. \tag{3.46}$$

Since the total boundary $\partial\mathcal{B}$ the union of the two surfaces $\partial\mathcal{B}^a$ and $\partial\mathcal{B}^c$, in eq. (3.45) two Lagrange multipliers λ^a and λ^c have been distinguished in order to make explicit the portion of the boundary (i.e. the surface or the CMB) they refer to. The same procedure is applied to derive the angular parameterization of the functionals (3.31)-(3.33). We have:

$$\delta\mathscr{F} = -g_0\sum_{jm}\int_c^a\delta\rho_{jm}\,\delta u^*_{jm}\,r^2dr, \tag{3.47}$$

$$\begin{aligned}\delta\mathscr{G} = \sum_{jm}\int_c^a\Bigg[&\left(\frac{dV_{jm}}{dr}\frac{d\delta V^*_{jm}}{dr}+\frac{J}{r^2}V_{jm}\,\delta V^*_{jm}\right)r^2dr\\ &+\frac{4\pi G}{g_0}\left(a^2\lambda^a_{jm}\,\delta V^*_{jm}(a)+c^2\lambda^c_{jm}\,\delta V^*_{jm}(c)\right)\\ &+a\,(j+1)V_{jm}(a)\,\delta V^*_{jm}(a)+c\,jV_{jm}(c)\,\delta V^*_{jm}(c)\Bigg],\end{aligned} \tag{3.48}$$

where, in the latter two terms, the solutions (2.18) and (2.19) to the Laplace equation have been used. Finally, the angular expansion of the functional associated with the right-hand side of the Poisson equation reads:

$$\delta\mathscr{H} = 4\pi G \sum_{jm} \int_c^a \delta\rho_{jm}\, \delta V^*_{jm}\, r^2 dr. \tag{3.49}$$

3.6 Finite element approximation of the radial coordinate

In order to parameterize the radial coordinate r, we divide the closed interval $[c, a]$ into N subintervals (not necessarily equally spaced) by the nodes $c = r_1 < r_2 < \ldots < r_N < r_{N+1} = a$. The piecewise linear base functions (*finite elements*) defined by the relation $\psi_k(r_i) = \delta_{ki}$, where δ_{ki} is the Kronecker delta, can be use to construct a base of the Sobolev space $\mathcal{W}_1^2(c, a)$ (e.g., Křižek & Neittaanmäki, 1990) and represent a convenient choice for our purposes. Note that, as shown in Fig. 3.1, on the interval $r_k \leq r \leq r_{k+1}$, only two of such base functions do not vanish, namely

$$\psi_k(r) = \frac{r_{k+1} - r}{r_{k+1} - r_k} \quad \text{and} \quad \psi_{k+1}(r) = \frac{r - r_k}{r_{k+1} - r_k}. \tag{3.50}$$

Working with base functions with finite support, instead with, for instance,

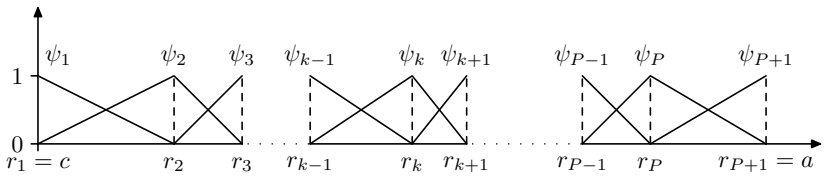

Figure 3.1: Piecewise linear finite elements that span the interval $[c, a]$. On each sub-interval $[r_k, r_{k+1}]$ only the two base functions ψ_k and ψ_{k+1} are nonzero.

orthogonal polynomials (Moucha et al., 2007), presents the advantage that, with respect to the radial coordinate, the matrix associated with the discrete system is sparse, with the consequence that a substantial saving of computer memory is possible and a large range of efficient algebraic tools are available (Barrett et al., 1994).

Since the sought solutions (u_{jm}, v_{jm}, w_{jm}, V_{jm}) are elements of the space $\mathcal{W}_1^2(c, a)$, they can be approximated by a linear combination of linear finite elements $\psi_k(r)$ as follows:

$$u_{jm}(r) = \sum_{k=1}^{N+1} u^k_{jm}\, \psi_k(r), \tag{3.51}$$

$$v_{jm}(r) = \sum_{k=1}^{N+1} v^k_{jm}\, \psi_k(r), \tag{3.52}$$

$$w_{jm}(r) = \sum_{k=1}^{N+1} w_{jm}^k \, \psi_k(r), \tag{3.53}$$

$$V_{jm}(r) = \sum_{k=1}^{N+1} V_{jm}^k \, \psi_k(r). \tag{3.54}$$

The corresponding test functions (δu_{jm}, δv_{jm}, δw_{jm}, δV_{jm}) will have clearly similar expressions. On the other hand, the coefficients of the pressure p_{jm} (and the associated test function δp_{jm}) belong to the space $\mathcal{L}^2(c,a)$ and, moreover, the perturbed density $\delta\rho$ and the (only for the moment) radially dependent viscosity η will be assumed to belong to the same space, so they can be simply approximated by piecewise constant functions $\xi_k(r)$:

$$p_{jm}(r) = \sum_{k=1}^{N} p_{jm}^k \xi^k(r), \tag{3.55}$$

$$\delta\rho_{jm}(r) = \sum_{k=1}^{N} \delta\rho_{jm}^k \xi^k(r), \tag{3.56}$$

$$\eta(r) = \sum_{k=1}^{N} \eta^k \xi^k(r), \tag{3.57}$$

where

$$\xi^k(r) = \begin{cases} 1 & \text{for } r_k \le r \le r_{k+1} \\ 0 & \text{otherwise.} \end{cases} \tag{3.58}$$

Note that, within the radial range $[c,a]$, while $N+1$ linear finite elements are possible, only N piecewise constant functions of the above type can be considered. Using the above representations, we proceed to express the functionals (3.43)-(3.49) in the finite element approximation. As an example, we carry out explicitely one integration of the radial coordinate in terms of finite elements. Considering the first term that appear under the integral sign of eq. (3.43). Using the representation (3.51) and that for the corresponding test function, we have:

$$\begin{aligned} \int_c^a \eta \frac{du_{jm}}{dr} \frac{d\delta u_{jm}^*}{dr} &= \sum_{k=1}^{N} \eta^k \int_{r_k}^{r_{k+1}} \sum_{\alpha=k}^{k+1} u_{jm}^\alpha \frac{d\psi_\alpha}{dr} \sum_{\beta=k}^{k+1} \delta u_{jm}^{\beta *} \frac{d\psi_\beta}{dr} \, r^2 dr \\ &= \sum_{k=1}^{N} \eta^k \sum_{\alpha=k}^{k+1} \sum_{\beta=k}^{k+1} I_{\alpha\beta}^{(1)} \, u_{jm}^\alpha \delta u_{jm}^{\beta *}, \end{aligned}$$

where the definite integrals $I_{\alpha\beta}^{(1)}$ can be readily computed analytically and are listed in Appendix C. The finite element representation of the complete functionals (3.43)-(3.49) can be found in a similar fashion. After some algebraic

manipulation, we obtain:

$$\begin{aligned}\delta\mathscr{E}_{\dot{\varepsilon}} = \sum_{jm}\sum_{k=1}^{N}\eta^k\sum_{\alpha=k}^{k+1}\sum_{\beta=k}^{k+1}\Big\{&2I^{(1)}_{\alpha\beta}\,u^{\alpha}_{jm}\,\delta u^{\beta*}_{jm}\\ &+J\Big[I^{(1)}_{\alpha\beta}\,v^{\alpha}_{jm}\,\delta v^{\beta*}_{jm}+I^{(3)}_{\alpha\beta}\Big(u^{\alpha}_{jm}-v^{\alpha}_{jm}\Big)\delta v^{\beta*}_{jm}\\ &+I^{(3)}_{\beta\alpha}v^{\alpha}_{jm}\Big(\delta u^{\beta*}_{jm}-\delta v^{\beta*}_{jm}\Big)+I^{(6)}_{\alpha\beta}\Big(u^{\alpha}_{jm}-v^{\alpha}_{jm}\Big)\Big(\delta u^{\beta*}_{jm}-\delta v^{\beta*}_{jm}\Big)\Big]\\ &+I^{(6)}_{\alpha\beta}\Big(2u^{\alpha}_{jm}-Jv^{\alpha}_{jm}\Big)\Big(2\delta u^{\beta*}_{jm}-J\delta v^{\beta*}_{jm}\Big)+J(J-2)I^{(6)}_{\alpha\beta}v^{\alpha}_{jm}\delta v^{\beta*}_{jm}\\ &+J\Big(I^{(1)}_{\alpha\beta}-I^{(3)}_{\alpha\beta}-I^{(3)}_{\beta\alpha}+I^{(6)}_{\alpha\beta}\Big)w^{\alpha}_{jm}\delta w^{\beta*}_{jm}+J(J-2)I^{(6)}_{\alpha\beta}w^{\alpha}_{jm}\delta w^{\beta*}_{jm}\Big\},\end{aligned} \tag{3.59}$$

$$\begin{aligned}\delta\mathscr{E}_{p} = -\sum_{jm}\sum_{k=1}^{N}\Big[&\delta p^{k*}_{jm}\sum_{\alpha=k}^{k+1}\Big(K^{(1)}_{\alpha}u^{\alpha}_{jm}+2K^{(2)}_{\alpha}u^{\alpha}_{jm}-JK^{(2)}_{\alpha}v^{\alpha}_{jm}\Big)\\ &+p^{k}_{jm}\sum_{\alpha=k}^{k+1}\Big(K^{(1)}_{\alpha}\delta u^{\alpha*}_{jm}+2K^{(2)}_{\alpha}\delta u^{\alpha*}_{jm}-JK^{(2)}_{\alpha}\delta v^{\alpha*}_{jm}\Big)\Big],\end{aligned} \tag{3.60}$$

$$\delta\mathscr{E}_{\lambda} = -\sum_{jm}\Big(a^2\,u^{N+1}_{jm}\delta\lambda^{a*}_{jm}+c^2\,u^{1}_{jm}\delta\lambda^{c*}_{jm}+a^2\,\lambda^{a}_{jm}\delta u^{N+1*}_{jm}+c^2\,\lambda^{c}_{jm}\delta u^{1*}_{jm}\Big), \tag{3.61}$$

$$\delta\mathscr{E}_{sg} = \rho_0\sum_{jm}\sum_{k=1}^{N}\sum_{\alpha=k}^{k+1}\sum_{\beta=k}^{k+1}\Big(I^{(2)}_{\alpha\beta}V^{\alpha}_{jm}\delta u^{\beta*}_{jm}+JI^{(5)}_{\alpha\beta}V^{\alpha}_{jm}\delta v^{\beta*}_{jm}\Big), \tag{3.62}$$

$$\delta\mathscr{F} = -g_0\sum_{jm}\sum_{k=1}^{N}\delta\rho^{k}_{jm}\sum_{\alpha=k}^{k+1}K^{(3)}_{\alpha}\delta u^{\alpha*}_{jm}, \tag{3.63}$$

$$\begin{aligned}\delta\mathscr{G} = \sum_{jm}\Bigg[&\sum_{k=1}^{N}\sum_{\alpha=k}^{k+1}\sum_{\beta=k}^{k+1}\Big(I^{(1)}_{\alpha\beta}V^{k}_{jm}\delta V^{\beta*}_{jm}+I^{(6)}_{\alpha\beta}V^{k}_{jm}\delta V^{\beta*}_{jm}\Big)\\ &+\Big(\frac{4\pi G}{g_0}a^2\lambda^{a}_{jm}\delta V^{k+1*}_{jm}+\frac{4\pi G}{g_0}c^2\lambda^{c}_{jm}\delta V^{1*}_{jm}\\ &-a(j+1)V^{k+1}_{jm}\delta V^{k+1*}_{jm}-cjV^{1}_{jm}\delta V^{1*}_{jm}\Big)\Bigg],\end{aligned} \tag{3.64}$$

$$\delta\mathscr{H} = 4\pi G\sum_{jm}\sum_{k=1}^{N}\delta\rho^{k}_{jm}\sum_{\alpha=k}^{k+1}K^{(3)}_{\alpha}\delta V^{\alpha*}_{jm}, \tag{3.65}$$

where the integrals $I^{(i)}_{\alpha\beta}$ and $K^{(i)}_{\alpha}$ are tabulated in Appendix C.

3.7 Spectral finite element representation of the strain-rate

The advantage of using the surface Lagrange multipliers λ^c and λ^a is not only that they help us to satisfy boundary conditions. Once its value is determined, we can readily compute the dynamic topography induced by the flow, the associated density perturbations and hence the geoid. However, if we were to use another strategy to adjust the boundary conditions (for instance, by selecting the flow vector from a different functional space), we would need to compute the surface radial tractions that cause boundary deformations from the expression of the stress tensor. Without using λ, the impermeability of $\partial\mathcal{B}$ could be obtained for example by choosing $\boldsymbol{u}$ in the space $\mathcal{W}_1^2(\mathcal{B})$ such that $\boldsymbol{u}\big|_{\partial\mathcal{B}} = 0$. Referring to Fig. 3.1, this implies that only one finite element should be present in the 1^{st} and N^{th} interval, namely ψ_2 and ψ_N, respectively. Nevertheless, it might be necessary to compute the stress or the strain-rate not only at the surface, but also inside the mantle. So far, we have shown how to parameterize over angular and radial coordinates the flow, pressure, Lagrange multipliers and gravity potential, but we still require a suitable parameterization of the strain-rate tensor, from which the parameterization of the stress clearly follows. Here we combine the tensor spherical harmonic representation (3.38) with the finite element approximations (3.51)-(3.53):

$$\dot{\boldsymbol{\varepsilon}}(r,\Omega) = \sum_{jm}\sum_{\ell=1}^{6} \dot{\varepsilon}^{\ell}_{jm}(r)\boldsymbol{Z}^{(\ell)}_{jm}(\Omega). \tag{3.66}$$

The radial dependence of the expansion coefficients $\dot{\varepsilon}^{\ell}_{jm}(r)$ has the following form:

$$\dot{\varepsilon}^{\ell}_{jm}(r) = a^{\ell}_{jm}\frac{1}{h_k} + b^{\ell}_{jm}\frac{\psi_k}{r} + c^{\ell}_{jm}\frac{\psi_{k+1}}{r}, \tag{3.67}$$

where $r_k \le r \le r_{k+1}$ and the constants a^{ℓ}_{jm}, b^{ℓ}_{jm} and c^{ℓ}_{jm} can be expressed in terms of the spectral finite element coefficients u^k_{jm}, v^k_{jm}, w^k_{jm} of the flow $\boldsymbol{u}$ as follows:

$$\boldsymbol{a}_{jm} = \begin{bmatrix} -u^k_{jm} + u^{k+1}_{jm} \\ -v^k_{jm} + v^{k+1}_{jm} \\ -w^k_{jm} + w^{k+1}_{jm} \\ 0 \\ 0 \\ 0 \end{bmatrix}, \boldsymbol{b}_{jm} = \begin{bmatrix} 0 \\ -v^k_{jm} + u^k_{jm} \\ -w^k_{jm} \\ w^k_{jm} \\ -\dfrac{u^k_{jm}}{J} + \dfrac{v^k_{jm}}{J} \\ \dfrac{v^k_{jm}}{2} \end{bmatrix}, \boldsymbol{c}_{jm} = \begin{bmatrix} 0 \\ -v^{k+1}_{jm} + u^{k+1}_{jm} \\ -w^{k+1}_{jm} \\ w^{k+1}_{jm} \\ -\dfrac{u^{k+1}_{jm}}{J} + \dfrac{v^{k+1}_{jm}}{J} \\ \dfrac{v^{k+1}_{jm}}{2} \end{bmatrix},$$

where $\boldsymbol{a}_{jm} \equiv [a^1_{jm},\ldots,a^6_{jm}]^t$, $\boldsymbol{b}_{jm} \equiv [b^1_{jm},\ldots,b^6_{jm}]^t$ and $\boldsymbol{c}_{jm} \equiv [c^1_{jm},\ldots,c^6_{jm}]^t$. Substituting eq. (3.67) into eq. (3.66), the strain-rate tensor can be expressed

as

$$\dot{\boldsymbol{\varepsilon}}(r,\Omega) = \boldsymbol{a}(\Omega)\frac{1}{h_k} + \boldsymbol{b}(\Omega)\frac{\psi_k}{r} + \boldsymbol{c}(\Omega)\frac{\psi_{k+1}}{r}, \tag{3.68}$$

where the second-order symmetric tensors $\boldsymbol{a}$, $\boldsymbol{b}$ and $\boldsymbol{c}$ are defined as

$$\boldsymbol{a}(\Omega) \equiv \sum_{jm}\sum_{\ell=1}^{6} a_{jm}^{\ell}\boldsymbol{Z}_{jm}^{(\ell)}(\Omega),$$

$$\boldsymbol{b}(\Omega) \equiv \sum_{jm}\sum_{\ell=1}^{6} b_{jm}^{\ell}\boldsymbol{Z}_{jm}^{(\ell)}(\Omega),$$

$$\boldsymbol{c}(\Omega) \equiv \sum_{jm}\sum_{\ell=1}^{6} c_{jm}^{\ell}\boldsymbol{Z}_{jm}^{(\ell)}(\Omega).$$

By means of eqs (A.21)-(A.26), the tensors $\boldsymbol{a}$, $\boldsymbol{b}$ and $\boldsymbol{c}$ can alternatively be represented in terms of six symmetric dyadics:

$$\boldsymbol{a} = a_{rr}\,\boldsymbol{e}_{rr} + a_{r\vartheta}\,\boldsymbol{e}_{r\vartheta} + a_{r\varphi}\,\boldsymbol{e}_{r\varphi} + a_{\vartheta\vartheta}\,\boldsymbol{e}_{\vartheta\vartheta} + a_{\vartheta\varphi}\,\boldsymbol{e}_{\vartheta\varphi} + a_{\varphi\varphi}\,\boldsymbol{e}_{\varphi\varphi},$$

where $\boldsymbol{e}_{ij}$, $i,j = r,\vartheta,\varphi$, denotes the symmetric part of the dyadic (or tensor) product between the two base vectors $\boldsymbol{e}_i$ and $\boldsymbol{e}_j$:

$$\boldsymbol{e}_{ij} \equiv \frac{1}{2}\left(\boldsymbol{e}_i \otimes \boldsymbol{e}_j + \boldsymbol{e}_j \otimes \boldsymbol{e}_i\right).$$

Similar relations clearly hold for tensors $\boldsymbol{b}$ and $\boldsymbol{c}$. The dyadic components of these tensors read therefore as

$$\begin{bmatrix} a_{rr} \\ a_{r\vartheta} \\ a_{r\varphi} \\ a_{\vartheta\vartheta} \\ a_{\vartheta\varphi} \\ a_{\varphi\varphi} \end{bmatrix} = \sum_{jm} \begin{bmatrix} (-u_{jm}^{k} + u_{jm}^{k+1})Y_{jm} \\ (-v_{jm}^{k} + v_{jm}^{k+1})E_{jm} + (w_{jm}^{k} - w_{jm}^{k+1})F_{jm} \\ (-v_{jm}^{k} + v_{jm}^{k+1})F_{jm} - (w_{jm}^{k} - w_{jm}^{k+1})E_{jm} \\ 0 \\ 0 \\ 0 \end{bmatrix},$$

$$\begin{bmatrix} b_{rr} \\ b_{r\vartheta} \\ b_{r\varphi} \\ b_{\vartheta\vartheta} \\ b_{\vartheta\varphi} \\ b_{\varphi\varphi} \end{bmatrix} = \sum_{jm} \begin{bmatrix} 0 \\ (-v_{jm}^{k} + u_{jm}^{k})E_{jm} + w_{jm}^{k}F_{jm} \\ (-v_{jm}^{k} + u_{jm}^{k})F_{jm} - w_{jm}^{k}E_{jm} \\ -w_{jm}^{k}H_{jm} + (u_{jm}^{k} - \dfrac{J}{2}v_{jm}^{k})Y_{jm} + \dfrac{1}{2}v_{jm}^{k}G_{jm} \\ w_{jm}^{k}G_{jm} + 2v_{jm}^{k}H_{jm} \\ w_{jm}^{k}H_{jm} + (u_{jm}^{k} - \dfrac{J}{2}v_{jm}^{k})Y_{jm} - \dfrac{1}{2}v_{jm}^{k}G_{jm} \end{bmatrix},$$

where the functions E_{jm}, F_{jm}, G_{jm} and H_{jm} depend on Ω and are defined in A.1. The dyadic components of tensor $\boldsymbol{c}$ can be obtained from those of $\boldsymbol{b}$ by replacing the finite element index k with $k+1$.

3.8 Angular integration

A crucial step in the derivation of the discrete form of variational equality (3.9) is the requirement that the viscosity be only radially dependent. For such a case, we have seen that the orthogonality of tensor spherical harmonics ensures the decoupling between different spherical harmonic modes, with the consequence that the angular integration of the functional $\delta\mathscr{E}_{\dot{\varepsilon}}$ is greatly simplified. In the presence of LVV, the analytical integration over finite elements illustrated in the previous section is still valid, however, orthogonality relations are no longer applicable and the explicit integration of the double-dot products of tensor spherical harmonics is necessary. To derive the parameterization of $\delta\mathscr{E}_{\dot{\varepsilon}}$ for the case of laterally dependent viscosity ($\eta = \eta(r, \Omega)$) is a tedious, but straightforward operation. Here, we limit ourselves to spend few words concerning how the integration over Ω can be carried out. After integrating over the radial coordinate only, which can be still done analytically, we find that $\delta\mathscr{E}_{\dot{\varepsilon}}$ is a linear combination of terms of the following kind:

$$\sum_{jm}\sum_{j'm'}\sum_{k=1}^{N}\sum_{\alpha=k}^{k+1}\sum_{\beta=k}^{k+1} I^{(q)}_{\alpha\beta} f^{\alpha}_{jm}\,\delta f^{\beta}_{j'm'} \int_{\Omega} \eta_k(\Omega)\boldsymbol{Z}^{(r)}_{jm}(\Omega) : \boldsymbol{Z}^{(s)*}_{j'm'}(\Omega)\,d\Omega, \quad (3.69)$$

where f represents one component of the flow (either u, v or w), q is the label of one finite element integral of Appendix C and r and s are the indices of two tensor spherical harmonics (see Appendix A.2 for the possible combinations of r and s). The viscosity is now assumed to be a square-integrable function not only on the radial range, but in the whole domain $\mathcal{B}$, i.e. $\eta \in \mathcal{L}^2(\mathcal{B})$. Thus, it is approximated by piecewise constant functions,

$$\eta(r, \Omega) = \eta_{kl},$$

where η_{kl} is the value of viscosity at a grid-point (r_k, Ω_l), where Ω_l is a latitude-longitude grid, $\Omega_l \equiv (\vartheta_{l_1}, \varphi_{l_2})$, with $l_1 = 1, \ldots, L_1$, $l_2 = 1, \ldots, L_2$, being L_1 and L_2 the number of ϑ- and φ-points, respectively. Under this assumption, the 2-D integration over Ω in a term like (3.69) can be performed numerically using a quadrature formula:

$$\int_{\Omega} \eta_k(\Omega)\boldsymbol{Z}^{(r)}_{jm}(\Omega) : \boldsymbol{Z}^{(s)*}_{j'm'}(\Omega)\,d\Omega \approx \sum_{l=1}^{L} w_l\,\eta_{kl}\,\boldsymbol{Z}^{(r)}_{jm}(\Omega_l) : \boldsymbol{Z}^{(s)*}_{j'm'}(\Omega_l),$$

where w_l are weight factors, $l = (l_1 - 1)L_2 + l_2$ and L is the total number of angular grid-points, $L = L_1 L_2$. The integration over longitude can be performed by fast Fourier transform (Martinec, 1989), while the integration over latitude can be obtained by the Gauss-Legendre quadrature formula (Press et al., 1992, Chapter 4).

3.9 Spectral finite element solution

We can now formulate the spectral finite element solution of the Stokes-Poisson boundary-value problem. Let us introduce the space $\mathcal{V}_h$, as follows:

$$\mathcal{V}_h \equiv \left\{ \begin{array}{l} \boldsymbol{u} = \displaystyle\sum_{j=1}^{j_{\max}} \sum_{m=-j}^{j} \sum_{k=1}^{N+1} \left[u_{jm}^k \psi_k \boldsymbol{S}_{jm}^{(-1)} + v_{jm}^k \psi_k \boldsymbol{S}_{jm}^{(1)} + w_{jm}^k \psi_k \boldsymbol{S}_{jm}^{(0)} \right] \\ p = \displaystyle\sum_{j=0}^{j_{\max}} \sum_{m=-j}^{j} \sum_{k=1}^{N} p_{jm}^k \xi_k Y_{jm} \\ \lambda = \displaystyle\sum_{j=0}^{j_{\max}} \lambda_{jm} Y_{jm} \\ V = \displaystyle\sum_{j=0}^{j_{\max}} \sum_{m=-j}^{j} \sum_{k=1}^{N+1} V_{jm}^k \psi_k Y_{jm} \end{array} \right\},$$

where $j_{\max}$ and N are finite cut-off degrees. The space $\mathcal{V}_h$ is clearly finite-dimensional and is a subspace of $\mathcal{V}$, provided that this space is extended to include also the potential $V \in \mathcal{W}_1^2(\mathcal{B})$. The *Galerkin method* for approximating the solution of the Stokes-Poisson boundary-value problem consists of finding $(\boldsymbol{u}_h, p_h, \lambda_h, V_h) \in \mathcal{V}_h$ such that, for all test functions $(\delta\boldsymbol{u}_h, \delta p_h, \delta\lambda_h, \delta V_h) \in \mathcal{V}_h$, the following equalities are satisfied:

$$\delta\mathscr{E}(\boldsymbol{u}_h, p_h, \lambda_h, V_h, \delta\boldsymbol{u}_h, \delta p_h, \delta\lambda_h, \delta V_h) = \delta\mathscr{F}(\delta\boldsymbol{u}_h), \tag{3.70a}$$

$$\delta\mathscr{G}(V_h, \lambda_h, \delta V_h, \delta\lambda_h) = \delta\mathscr{H}(\delta V_h). \tag{3.70b}$$

Through eqs (3.70), the Stokes-Poisson problem is reduced to a system of linear algebraic equations (Galerkin system). The discrete solution $(\boldsymbol{u}_h, p_h, \lambda_h, V_h)$ of such a system is what we call the *spectral-finite element* (SFE) *solution*. Proofs relative to the convergence and validation of the SFE solution will be presented in the following chapters.

As already mentioned, for 1-D viscosity structures, the system is decoupled in terms of harmonic degrees j. As a consequence, the Galerkin matrix is simply block diagonal, with each block associated to only one particular degree j. Moreover, the width of the band is limited because of the finiteness of the support of the piecewise linear or piecewise constant finite element base functions ψ_k and ξ_k. The sparsity level of the matrix (Fig. 3.2) is very high (i.e. the number of nonzero element is small compared to the number of zero elements) and the storage of a single band requires a relatively small amount of memory. The inversion of the block diagonal matrix can be performed quickly and accurately by a LU-decomposition of the compactly stored band, followed by a backsubstitution (Press et al., 1992, Chapter 2).

The mode-coupling that arises for the cases of 2-D or 3-D viscosity distributions requires a more sophisticated strategy for solving the system of equations. The matrix is no longer simply band diagonal but presents, $(j_{\max} - 1)$ banded

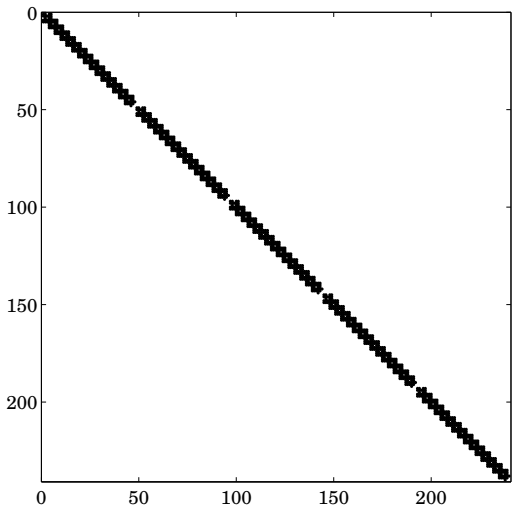

Figure 3.2: Sparsity pattern of a band-diagonal matrix arising from a problem with 1-D viscosity with $j_{\max} = 5$ and $N = 15$. The five banded blocks associated to each degree are clearly visible. Black areas denote nonzero matrix elements.

sub-diagonals and $(j_{\max} - 1)$ banded super-diagonals. Figure 3.3 shows a sparsity plot arising from a problem with 2-D axisymmetric viscosity (for the case of fully 3-D viscosity the plot is similar, with the only difference being that the sparsity is reduced due to the coupling of the spherical harmonic orders m). The larger number of diagonals increases the number of nonzero elements of the matrix. Nevertheless, because of the use of finite elements, the matrix can be still considered sparse. Hence, the use of inversion techniques that exploit sparsity is convenient. For treating problems even with a relatively low resolution ($j_{\max} \sim 30$), the few giga byte of memory usually available on an average workstation may not be sufficient and particular techniques such as the *compressed column storage method* (Barrett et al., 1994) for storing nonzero matrix elements only becomes mandatory. Furthermore, direct solvers, like that employed for the band matrix of the 1-D viscosity problem, become ineffective since they would require too long computational times. So-called *non-stationary iterative techniques* are usually employed to overcome these troubles. The Earth's mantle exhibits strong, sharp variations (radial as well as lateral) in viscosity. Because of this, the system matrix is often ill-conditioned with vastly varying element magnitudes. The rate at which an iterative method converges depends greatly on the conditionality (or spectrum) of the coefficient matrix. Hence, iterative methods usually involve a second matrix that transforms the coefficient matrix into one with a more favorable spectrum. The transformation matrix is called a *preconditioner* (e.g. Benzi, 2002). A good preconditioner improves the convergence of the iterations sufficiently to overcome the extra cost of applying it and, where necessary, of constructing it. Indeed, without the preconditioner, the it-

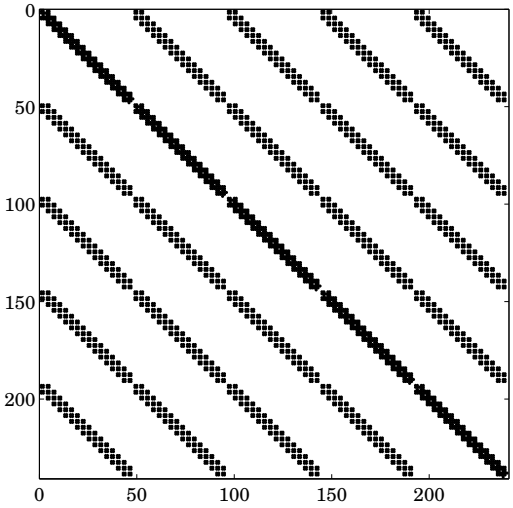

Figure 3.3: Sparsity pattern of a multi-band diagonal matrix arising from a problem with a 2-D viscosity with $j_{\max} = 5$ and $N = 15$. Beside the principal band diagonal, four banded sub- and super-diagonals appear because of mode-coupling. Black areas denote nonzero matrix elements.

erative method may even fail to converge. For the computations involving LVV that will be presented in the following, we adopted the *preconditioned conjugate gradient method* (e.g. Saad, 2003). The choice of the preconditioner greatly depends on the nature of the coefficients matrix. Among different possibilities that involve special factorizations of the original matrix, we found the use of the principal diagonal of the matrix a natural and convenient choice. In this way, the convergence of the iterations for problems that involve LVV, is facilitated by the use as a preconditioner of the matrix associated with the problem without LVV.

3.10 Layered convection

We have built our numerical model assuming that convection in the Earth's interior involves the mantle as a whole, a single layer that extends from the surface to the CMB. In this respect, we speak of *whole layer* mantle convection. Indeed, as it will be shown in the following chapter, these types of one-layer models (even without LVV) are quite successful in fitting the long-wavelength geoid (e.g. Panasyuk & Hager, 2000). Their drawback is that they generally fail when a fit to the surface dynamic topography is sought as the predicted amplitudes of this quantity ($\sim \pm 2$ km) are too large when compared to observations (e.g. Hager & Clayton, 1989; Ricard et al., 1993; Forte et al., 1993). One way to overcome this problem is to consider *layered convection*. If we assumed that the seismic discontinuity at 670 km depth represents an actual chemical barrier for

the flow, convection in the upper and lower mantle would take place separately. However, clear tomographic images of subducting slabs that penetrate into the lower mantle (van der Hilst et al., 1997) disprove this picture. A compromise between the two extreme pictures of whole layer and fully layered convection, that is also supported by geochemists (Hofmann, 1997), is that of some form of *partial layering* (Thoraval et al., 1995; Čadek & Fleitout, 1999).

A convenient way that allows us to model either fully or partially layered convection has been introduced by Le Stunff & Ricard (1997). They propose a physical mechanism according to which mass anomalies that hinder the flow can be generated at the transition zone opposing vertical advection of material through it. In a first approximation, this can be modeled by simply adding to the density anomalies $\delta\rho$ responsible for mantle buoyancy a contribution proportional to the radial flow:

$$\delta\rho' = \delta\rho + \gamma\, \boldsymbol{e}_r \cdot \boldsymbol{u},$$

where $\gamma = \gamma(r)$ is a radially dependent coefficient, with dimensions kg s m^{-4}, that controls the amplitude of the local layering effect. When $\gamma = 0$, the problem is that of whole layer convection, while when $\gamma = \delta(r - r_0)$, vertical flow at $r = r_0$ vanishes and two distinct convection layers are created. The partially layered case is obtained for constant values of γ. The effect caused by the modified density anomaly $\delta\rho'$ can be easily incorporated in the weak formulation by adding to eq. (3.4) the following functional:

$$\delta\mathscr{E}_\gamma \equiv -g_0 \int_{\mathcal{B}} \gamma\, u_r\, \boldsymbol{e}_r \cdot \delta\boldsymbol{u}\, dV. \tag{3.71}$$

Using piecewise constant functions to approximate the radial dependence of γ, the spectral finite element discretization of eq. (3.71) is readily obtained:

$$\delta\mathscr{E}_\gamma = -g_0 \sum_{jm} \sum_{k=1}^{N} \gamma^k \sum_{\alpha=k}^{k+1} \sum_{\beta=k}^{k+1} I^{(4)}_{\alpha\beta} u^\alpha_{jm}\, \delta u^{\beta *}_{jm}. \tag{3.72}$$

CHAPTER 4

Radially symmetric viscosity models

The methods developed in the previous chapters are here applied to solve the Stokes-Poisson problem in the presence of radially symmetric viscosity distributions. After introducing the Green's functions formalism, we show how the matrix propagator technique is used to validate the numerical SFE solution. Finally, using the standard approach of exploring the parameter space, we present a simple inversion of the long-wavelength geoid in terms of a three-layer mantle viscosity, showing that a good fit to the geoid can be obtained.

4.1 Green's functions formalism

Testing directly the effects of different radial (or 1-D) viscosity distributions on the geoid using the load provided by a tomographic model can be rather intricate. A very instructive way to analyze the behavior of the mantle in response to simple internal loads is to construct *Green's functions*. These are particularly useful in practical applications where, as in our case, one wants to solve a partial differential equation (PDE) in a certain bounded domain. In this respect, Green's functions can be seen as the analogue of the more general *fundamental solutions* described by the theory of PDE when problems are posed on all of space.

Given a linear differential operator $\mathcal{L}$, a solution to the PDE

$$\mathcal{L}u(\boldsymbol{r}) = f(\boldsymbol{r})$$

can be expressed (e.g. Renardy & Rogers, 1993) as

$$u(\boldsymbol{r}) = \int_{\mathcal{B}} G(\boldsymbol{r}, \boldsymbol{r}')\, f(\boldsymbol{r}')\, d\boldsymbol{r}', \tag{4.1}$$

where u also satisfies some boundary conditions on $\partial\mathcal{B}$, $\boldsymbol{r}$ denotes the position vector in the domain $\mathcal{B}$ and $G(\boldsymbol{r}, \boldsymbol{r}')$ is the Green's function that is defined as

the solution of the problem

$$\mathcal{L}G(\boldsymbol{r},\boldsymbol{r}') = \delta(\boldsymbol{r}-\boldsymbol{r}'),$$

being $\delta(\boldsymbol{r}-\boldsymbol{r}')$ the Dirac delta function. Furthermore, G satisfies the same boundary conditions of u. Referring to our problem, the field u can be seen as a geophysical observable (geoid, topography, etc.), while f is the internal load represented by density anomaly $\delta\rho$. The spherical harmonic expansion of G reads as

$$G(\boldsymbol{r},\boldsymbol{r}') = \sum_{jm} G_{jm}(r,r')Y_{jm}(\Omega)Y^*_{jm}(\Omega'). \tag{4.2}$$

Upon expanding in spherical harmonics u and f as well and substituting into eq. (4.1), it can be easily shown that the coefficients of u are

$$u_{jm}(r) = \int_c^a G_{jm}(r,r')f_{jm}(r')\,dr'. \tag{4.3}$$

In the following, the name Green's function (or *response function* or *kernel*) will be used to indicate the coefficients G_{jm} of eq. (4.3). According to the 'shift-property' of δ, if we choose $f_{jm}(r') = \delta(r-r')$, from eq. (4.3), we have

$$G_{jm}(r,r_0) = \int_c^a G_{jm}(r,r')\,\delta(r'-r_0)\,dr', \tag{4.4}$$

where $r_0 \in [c,a]$. Therefore, eq. (4.3) simply states that the solution u_{jm} can be found by convolving the Green's function G_{jm} with the real load f_{jm}.

As an example, we determine analytically the Green's function of the gravity potential for the Poisson equation (2.23). The solution to this is given by the Newton integral:

$$V(\boldsymbol{r}) = G\int_B \frac{\delta\rho(\boldsymbol{r}')}{L}\,d^3\boldsymbol{r}'. \tag{4.5}$$

In this case, the contribution of boundary deflections is neglected. According to the *addition theorem* for spherical harmonics, we have

$$\frac{1}{L} = 4\pi r\sum_{jm}\frac{1}{2j+1}\left(\frac{r'}{r}\right)^{j+2}Y_{jm}(\Omega)Y^*_{jm}(\Omega'), \tag{4.6}$$

where we considered the source r' lying beneath the observer r, i.e. $r' < r$. Expanding $\delta\rho$ in spherical harmonics and inserting eq. (4.6) into eq. (4.5) yields the coefficients V_{jm} of the gravity potential

$$V_{jm}(r) = \frac{4\pi G r}{2j+1}\int_c^a \left(\frac{r'}{r}\right)^{j+2}\delta\rho_{jm}(r')\,dr'. \tag{4.7}$$

Comparing eqs (4.7) and (4.3) we find that the sought Green's function is

$$G_{jm}(r, r') = \frac{4\pi G r}{2j+1} \left(\frac{r'}{r}\right)^{j+2} . \tag{4.8}$$

If we further divide G_{jm} by the reference gravity g_0 and evaluate the expression at $r = a$, we obtain the Green's function of the *static* geoid (i.e. without the contributions of boundary deflections). This is plotted in Fig. 4.1 after normalizing by the factor $4\pi G a/(2j+1)g_0$. This type of figure, which will be extensively used in the following, tells us what is the amplitude of the geoid induced by an internal δ-like load only, as the depth of the load is varied through the entire mantle. The kernels do not depend on the order m and the greatest response is obtained for shallow loads. This behavior is further amplified as the harmonic degree increases because of the attenuation effect due to the term $(r'/r)^{j+2}$. As we will shortly see, the inclusion of boundary deformation will change this picture.

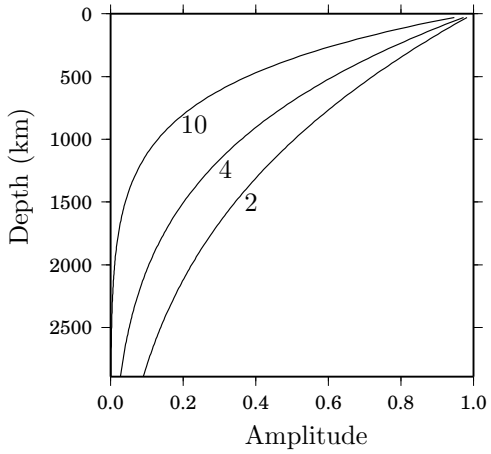

Figure 4.1: Normalized Green's functions of the static geoid for harmonic degrees $j = 2$, 4 and 10.

4.2 Validation of the SFE approach

We will now show Green's functions for 1-D viscosity models. Because of the assumption of radially symmetric viscosity, they can be obtained using the matrix propagator technique. For this reason, they not only provide a good insight into the way the mantle responds to internal loads, but they also represent a convenient tool that can be used to validate numerical solutions of the Stokes-Poisson problem. Before discussing in detail the effects of different viscosity stratifications on the geoid and topography (see next section) we show here how

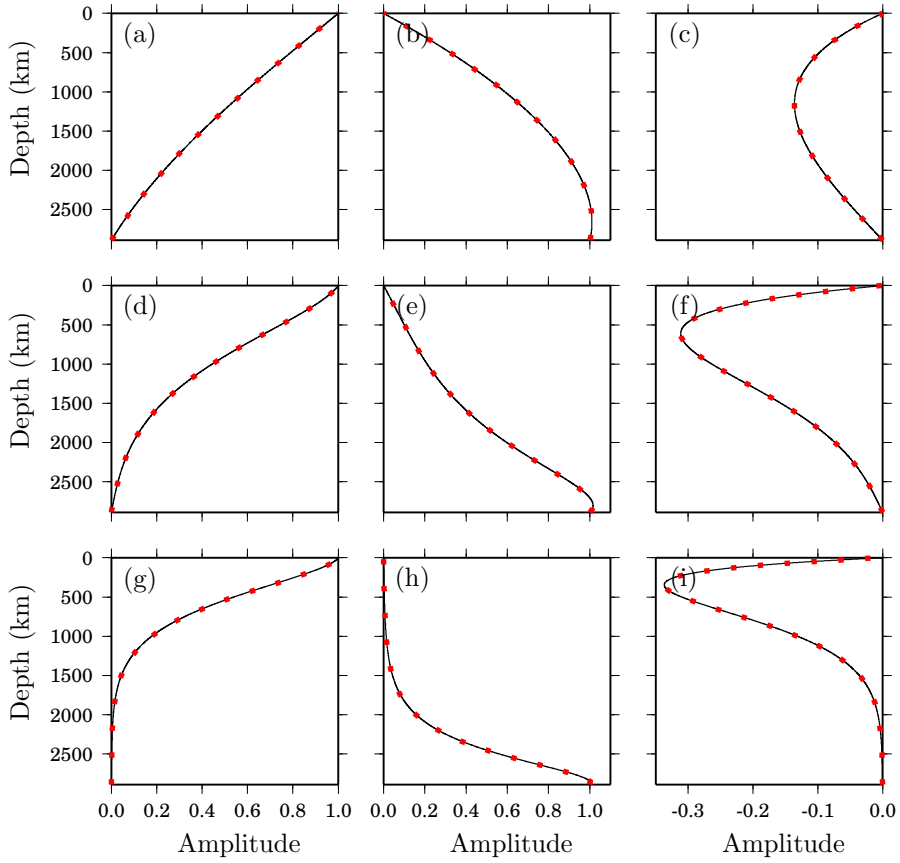

Figure 4.2: Matrix propagator solution (black lines) versus SFE solution (red squares) for isoviscous mantle. Green's functions of surface dynamic topography (panels a, d, g), CMB dynamic topography (panels b, e, h) and geoid (panels c, f, i) are plotted for degree $j = 2$ (panels a, b, c), $j = 8$ (panels d, e, f) and $j = 16$ (panels g, h, i).

the SFE solution presented in Chapter 3 has been tested against the matrix propagator solution by comparing the kernels resulting from an isoviscous and a two-viscosity layers mantle.

Figure 4.2 shows the comparison between the kernels of dynamic surface topography, CMB topography and geoid obtained via matrix propagator (black lines) and SFE technique (red squares) in the case of a isoviscous mantle and for different harmonic degrees of load/response (j = 2, 8, 16). Surface and CMB topography kernels are normalized by their own value at the Earth's surface and at the CMB, respectively. Geoid normalization is the same as described in the previous section. The load prescribed is a δ-like load of unitary amplitude. As it is evident from the figure, the agreement between the two solutions is very

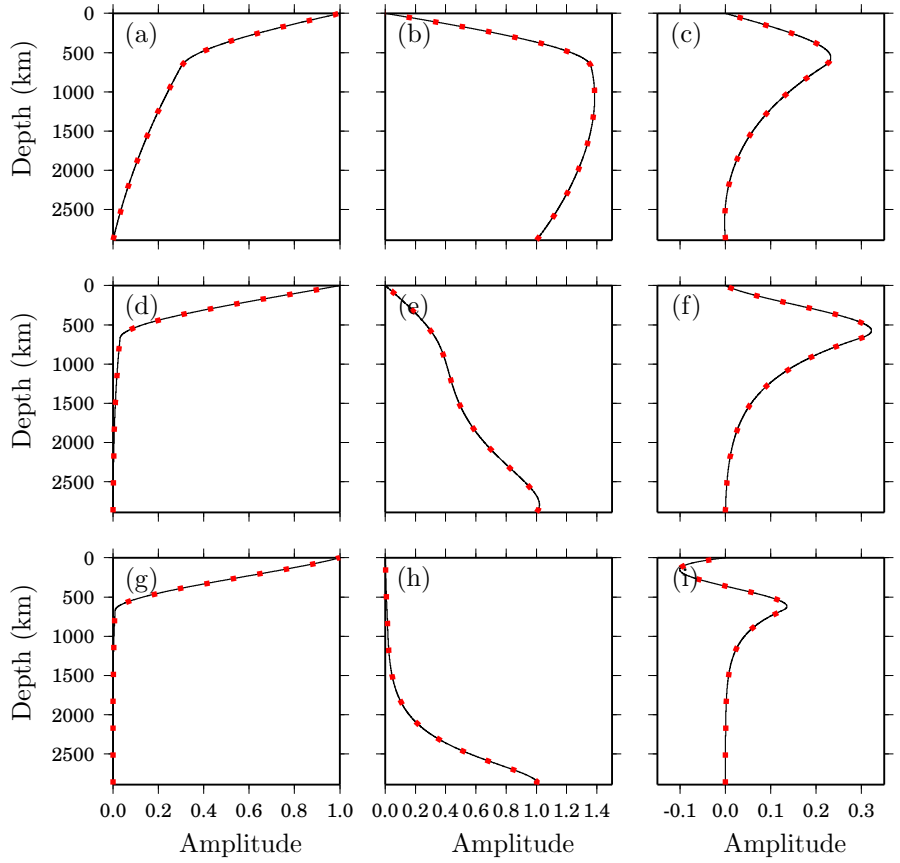

Figure 4.3: As in Fig. 4.2 but for a two-layer mantle, where the lower mantle is 100-times more viscous than the upper.

good. Such a good agreement is maintained for the case of a model consisting of two layers, with the lower mantle being 100-times more viscous than the upper mantle ($\eta_{\rm lm}/\eta_{\rm um} = 100$) as shown in Fig. 4.3.

In both Figures 4.2 and 4.3, the number of finite elements employed to plot the SFE solution is 80. Nevertheless, it is interesting to show how the SFE solution converges to the matrix propagator solution as the number of finite elements is increased. In Fig. 4.4, we show the convergency test for the geoid kernel of degree $j = 16$ with $\eta_{\rm lm}/\eta_{\rm um} = 100$ (Fig. 4.3i). The numerical solution converges quite rapidly to the analytical one. We start with 5 finite elements and increase their number up to 60 with which the two curves are practically indistinguishable.

In Chapter 5 we develop a semi-analytical solution of the Stokes problem that allows us to validate the SFE solution for an axisymmetric distribution of

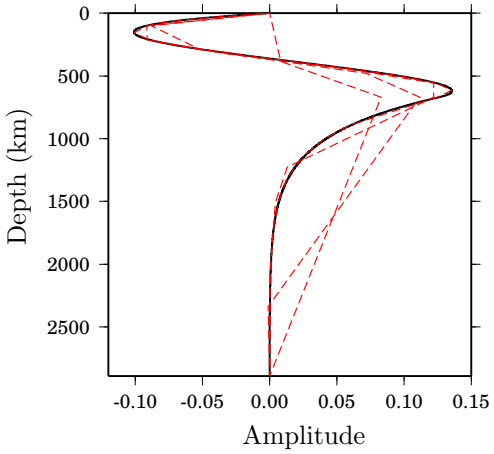

Figure 4.4: Convergency of the SFE solution (red dashed line) to the matrix propagator solution (black solid line) as the number N of finite elements is increased. The geoid Green's function of degree 16 with $\eta_{\rm lm}/\eta_{\rm um} = 100$ is shown. The SFE solution is plotted for N =5, 10, 20 and 60.

viscosity. For now, in the light of what we showed above, our numerical solution for the case of 1-D viscosity can be considered correct and in the following we will abandon the matrix propagator and base our results exclusively on a code that implements the SFE approach.

4.3 Green's functions for different Earth models

We present now topography and geoid Green's functions for a few simple viscosity models. It is by no means the purpose of this section to give an exhaustive description of the kernels under the many possible combinations of mantle viscosity stratification. For this we refer, for instance, to Hager & Clayton (1989) or Corrieu et al. (1995), who discussed a large variety of kernels and thoroughly investigated the effects of layered convection, astenospheric viscosity, viscosity of the D$''$ region and compressibility. Here, we will limit ourselves to considering a three-layer mantle stratification consisting of a lithosphere of viscosity $\eta_{\rm lith}$ (top 100 km), an upper mantle of viscosity $\eta_{\rm um}$ (from 100 km depth to the transition zone at 670 km depth) and a lower mantle of viscosity $\eta_{\rm lm}$ (from 670 km depth to the CMB).

Before analyzing in detail the Green's functions, it is important to point out that the geoid is only sensitive to relative radial variations of viscosity. In fact, if we look at the system matrix (2.53), we notice that the spheroidal flow and shear stress (variables y_1, y_2 and y_4, respectively) depend on the viscosity η, while the radial stress, gravitational potential and gravitational intensity (variables y_3, y_5 and y_6, respectively) do not. The geoid and dynamic topography of the surface

Model	$\eta_{\rm lith}$	$\eta_{\rm um}$	$\eta_{\rm lm}$
1	1	1	1
2	30	1	1
3	1	1	30
4	40	1	30

Table 4.1: Relative viscosities of 1-D models.

and CMB are related to the latter three quantities that do not depend on η. The consequence is that these observables are only sensitive to relative variations of viscosity with depth. On the other hand, if we were to compute the flow - for instance if we tried to predict plate motion (e.g. Wen & Anderson, 1997; Becker & O'Connell, 2001) - the absolute value of viscosity would also be important. As shown in Table 4.1, in our calculations we will keep fixed the upper mantle viscosity as reference ($\eta_{\rm um} = 1$) and vary the other two parameters $\eta_{\rm lith}$ and $\eta_{\rm lm}$.

Model 1 is presented in Figure 4.5. This is the simplest possible model representing whole mantle convection in a uniform viscous mantle. Normalized kernels for surface topography, CMB topography, total boundaries deformation and geoid are presented for degrees $j = 2$, $j = 4$ and $j = 8$. We prescribe a unitary negative δ-load, which can be seen as an upwelling localized at a certain depth. This explains why the value of the dynamic topography of the surface and CMB is positive (see also Fig. 1.6). For all degrees, the deformation of the upper surface decreases, while the deformation of the CMB increases as the load approaches the CMB. Loads that are close to the upper surface are not able to deform the CMB and vice versa. The lack of symmetry between the kernels of the surface and CMB deformation is due to the spherical geometry of the problem. The intensity of the load prescribed is the same everywhere, therefore, the deeper the load, the smaller is the radius at which is applied. This results in greater stresses and strain-rates at depth than at the surface. The total deformation shown in Fig. 4.5c is normalized by the applied load and measures the total mass displaced at the two boundaries. For long wavelengths ($j = 2$, 4), this mass is even larger than the loading mass that induces the flow. This proves once again the importance of considering boundary deformations when computing the gravitational potential. The geoid shown in Fig. 4.5d contains the effects of both internal loading and surface deformation. As expected, the shape of the Green's functions changes dramatically with respect to the static kernels of Fig. 4.1. When the perturbing mass is localized either at the surface or at the CMB the geoid vanishes, indicating that in these situations the mass anomaly is isostatically compensated. The low-degree geoid is also greatly influenced by mass located in the lower mantle, while, at shorter wavelengths, the importance of lower mantle loads diminishes and upper mantle mass anomalies become more important.

With a radially symmetric viscosity it is not possible to satisfactorily model

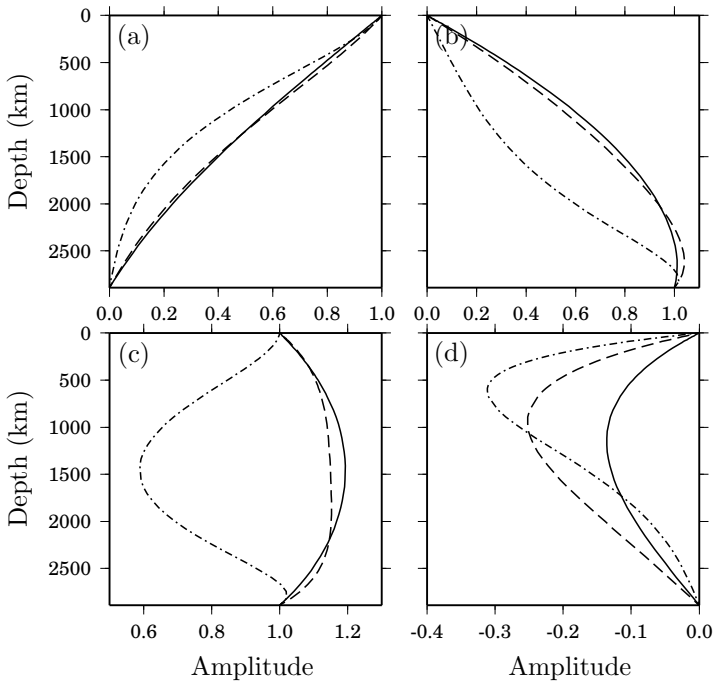

Figure 4.5: Model 1 kernels of dynamic topography of the surface (panel a), dynamic topography of the CMB (panel b), total deformation of the boundaries (panel c) and geoid (panel d), for harmonic degree $j = 2$ (solid line), $j = 4$ (dashed line) and $j = 8$ (dashed-dotted line).

the lithosphere. The lithosphere is the upper cold thermal boundary layer of mantle convection and, because of its relatively low temperature, is supposed to be stronger than the underlying mantle and to have a much higher viscosity. Locally, the stiff lithosphere behaves like an elastic layer whose viscosity is practically infinite. However, on a global scale, the lithosphere also deforms and most of this deformation is concentrated at plate boundaries where narrow regions of anomalously high temperature coincide with large lateral changes in viscosity. A uniformly viscous lithosphere can not account for these changes, so we can only try to average them (see also the next section). With Model 2 (Fig. 4.6), we test the effect of a lithosphere which is 30-times more viscous than the upper and lower mantle that have here the same viscosity. A lithosphere with a higher viscosity with respect to the mantle causes slightly greater surface deformations and smaller CMB deformations. The net effect is a reduced total mass displacement and a more negative geoid.

Assuming an adiabatic mantle, the viscosity, being pressure dependent, is expected to vary with depth according to the adiabatic gradient. Therefore, an increase in viscosity should occur at phase transitions. To approximate this

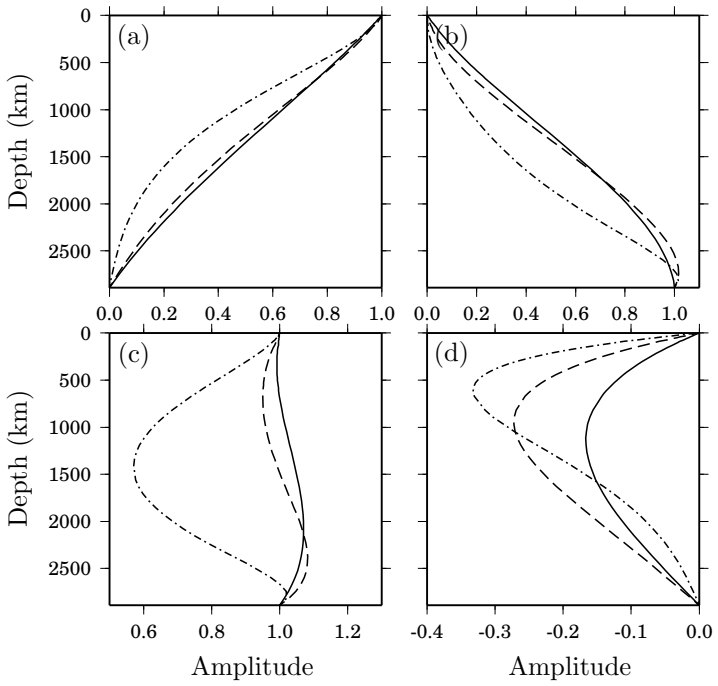

Figure 4.6: As in Fig. 4.5 but for Model 2.

effect, we show in Fig. 4.7 the Green's function for Model 3 which consists of a two layer system with a lower mantle having a viscosity 30 times higher than that of the upper mantle and lithosphere, which here have the same viscosity. The increase in lower mantle viscosity has a large effect on the Green's functions. The deformation of the upper surface is reduced in such a way that deep lower mantle anomalies have a smaller effect as the wavelength diminishes. A reverted argument is valid for the deformation of the CMB but only at long wavelengths: at degree 2 and 4, lower mantle anomalies greatly contribute to the CMB topography, while at degree 8, the Green's function is qualitatively similar to those of the previous two models. Model 3 also shows that the sign of the response function for the geoid can change across the mantle. At degree 2, it is still negative in the lower mantle, while it becomes positive in the upper mantle. At higher degrees, the geoid sign is positive everywhere.

Model 4 (Fig. 4.8) completes our brief analysis of mantle Green's functions. As we will show in the following section, the radial viscosity stratification of this model is similar to the one that proves to be successful in predicting the long wavelength geoid on the base of tomographic data. The model consists of three viscosity layers; the lower mantle has a viscosity 30-times higher than that of the upper mantle, while the lithosphere is a little stiffer with a viscosity 40-times higher than that of the upper mantle. The geoid Green's functions for

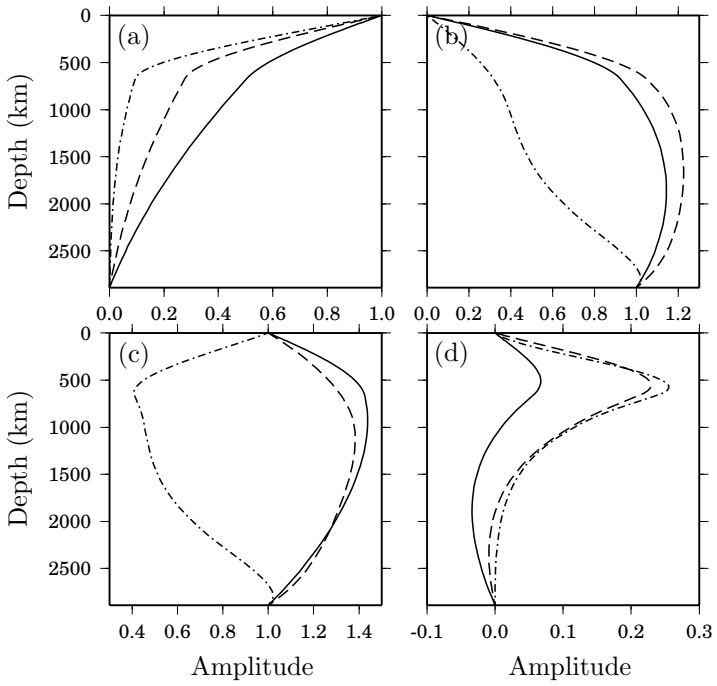

Figure 4.7: As in Fig. 4.5 but for Model 3.

this model (Fig. 4.8d) appear to be more complex than before. The presence of three distinct viscosity layers causes the degree-2 and degree-4 kernels to change sign twice within the mantle range. It is evident that at long wavelengths ($j = 2$, but also $j = 4$) the geoid is mainly influenced by lower mantle anomalies that give a negative net contribution.

4.4 A simple geoid inversion

Starting from the middle 80s until recent years, the inversion of the long-wavelength geoid in terms of radially symmetric viscosity models has received a great deal of attention (Ricard et al., 1984; Richards & Hager, 1984; Hager & Clayton, 1989; Forte & Peltier, 1991; King & Masters, 1992; King, 1995b; Thoraval & Richards, 1997; Čadek & Fleitout, 1999; Kaufmann & Lambeck, 2000). The layers whose viscosities have been inverted for range from only major mantle layers (e.g. Corrieu et al., 1995) - typically the lithosphere and upper and lower mantle - to a total of 10-15 layers, with detailed treatment of the asthenosphere and transition zone (e.g. Forte & Mitrovica, 1996). Under the approximation of 1-D viscosity, it is possible to identify several stratifications that are able to fit the observations equally well (Panasyuk & Hager, 2000). Nevertheless, a number of important results have been obtained. For instance, the best models - for

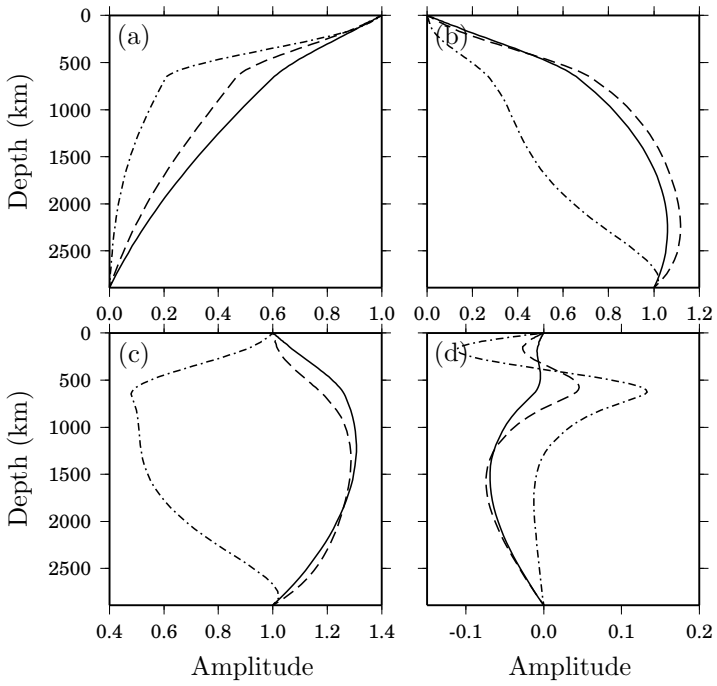

Figure 4.8: As in Fig. 4.5 but for Model 4.

which up to approximately 80-90 per cent of the degree-variance reduction of the long-wavelength geoid can be obtained - usually favour whole-layer convection with a pronounced increase in the viscosity of the lower mantle with respect to that of the upper mantle (Thoraval & Richards, 1997) and an asthenosphere (King, 1995b) or transition zone (Hager & Clayton, 1989) with a relatively low viscosity.

The topic has been extensively treated in the publications referenced above. However it is instructive to show here how it is possible to obtain a fairly good fit to the geoid with a simple inversion based on the exploration of the parameter space. We invert for the same three viscosity parameters that we used in the previous section to plot Green's functions, namely $\eta_{\rm lm}$, $\eta_{\rm um}$ and $\eta_{\rm lith}$. As mentioned above, the geoid is only sensitive to relative variations in viscosity, thus the inversion does not allow us to constrain absolute viscosity values. We explore then the parameters space considering the viscosity ratios $\eta_{\rm lm}/\eta_{\rm um}$ and $\eta_{\rm lith}/\eta_{\rm um}$ within the following ranges:

$$\begin{aligned} 1 \leq \frac{\eta_{\rm lm}}{\eta_{\rm um}} \leq 10^3, \\ 1 \leq \frac{\eta_{\rm lith}}{\eta_{\rm um}} \leq 10^3. \end{aligned} \tag{4.9}$$

The inverse problem is formulated as a search for the ratios $\eta_{\rm lm}/\eta_{\rm um}$ and $\eta_{\rm lith}/\eta_{\rm um}$ in the interval (4.9) that yield the best fit to the GRACE geoid (see Chapter 1) in the sense of an $\mathcal{L}^2$ norm (King, 1995b; Čadek & Fleitout, 1999). For the inversion, only the long-wavelength part of the geoid spectrum (from $j = 2$ to $j_{\rm max} = 10$) has been considered. The agreement between predicted and observed geoid is expressed as a percentage of the fitted data, or *variance reduction* R,

$$R = \left[1 - \frac{\displaystyle\sum_{j=2}^{10} \sum_{m=-j}^{j} \left(N_{jm}^{\rm obs} - N_{jm}^{\rm mod} \right)^2}{\displaystyle\sum_{j=2}^{10} \sum_{m=-j}^{j} \left(N_{jm}^{\rm obs} \right)^2} \right] \times 100\%, \tag{4.10}$$

where $N_{jm}^{\rm obs}$ and $N_{jm}^{\rm mod}$ denote the spherical harmonic coefficients of the observed and modeled geoid, respectively. The cut-off degree $j_{\rm max} = 10$ is chosen in accordance to the results of Le Stunff & Ricard (1995) who showed that a large part of the geoid at degrees $j \geq 10$ can be explained by lithospheric mass anomalies. To compute the model coefficients $N_{jm}^{\rm mod}$, we use the SFE approach and the S-waves *smean* tomographic model of Becker & Boschi (2002), whose velocity anomalies are converted to density anomalies according to the scaling relation of Karato (1993) (see Chapter 1). In Fig. 4.9, we show the variance reduction R as a function of the logarithmic ratios $\log_{10}(\eta_{\rm lm}/\eta_{\rm um})$ and $\log_{10}(\eta_{\rm lith}/\eta_{\rm um})$. The highest value we found ($R \sim 82\%$) turns out to be well constrained and, considering the upper mantle viscosity as reference, is obtained for the following values of viscosity parameters:

$$\eta_{\rm lm} = 40\,\eta_{\rm um} \quad \text{and} \quad \eta_{\rm lith} = 25\,\eta_{\rm um}. \tag{4.11}$$

These values are in agreement with previous studies (e.g. King, 1995b; Corrieu et al., 1995) and confirm that, in the case of radially symmetric viscosity models, a pronounced viscosity increase in the lower mantle (usually at least a factor of 30 is necessary) and a relatively weak lithosphere are needed to obtain a reasonable fit to the data. The low viscosity value for the lithosphere can be justified by arguing that the (laterally dependent) weakening of the lithosphere at plate boundaries yields an effect on the geoid equivalent to that of a (laterally uniform) globally weaker lithosphere.

Using the estimated parameters (4.11), we show in Fig. 4.10 the resulting geoid map. The similarities between observed (Fig. 1.1) and modeled geoid are evident. The geoid computed with the SFE approach correctly reproduces the characteristic lows of Antarctica, the Indian Ocean, the West Atlantic Ocean and the East Pacific Ocean, as well as the highs over Africa and those over subduction zones of the West and North Pacific and South America, although the amplitudes of these are generally greater than the observations. The model fails to reproduce the broad geoid high centered in Iceland, which is probably associated with a mantle upwelling (Marquart & Schmeling, 2004), and the geoid low over Canada that can be explained in terms of glacial isostatic adjustment (van der Wal et al., 2004).

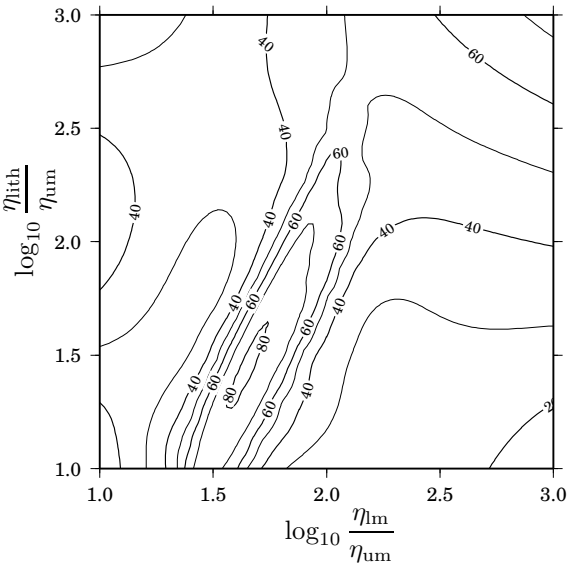

Figure 4.9: Variance reduction for the fit to the long-wavelength geoid. The region of highest reduction (more than 80%) shows that the viscosity ratios $\eta_{\rm lm}/\eta_{\rm um}$ and $\eta_{\rm lith}/\eta_{\rm um}$ are well constrained.

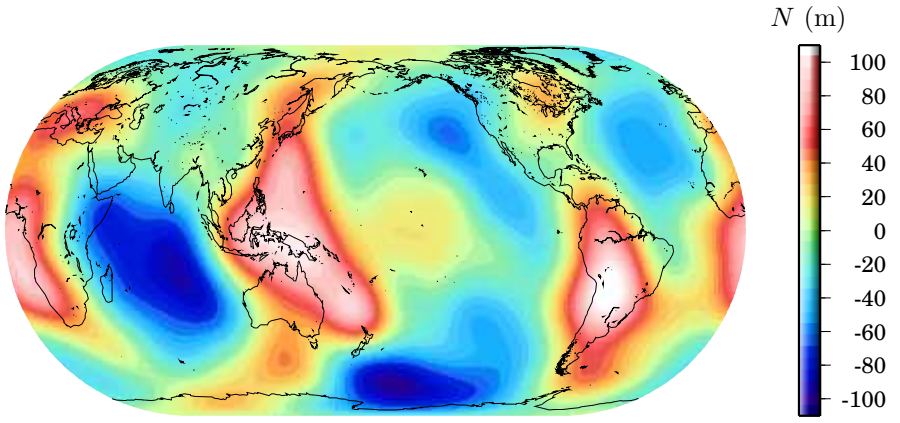

Figure 4.10: Long-wavelength geoid ($j = 2 - 10$) computed via SFE approach using a three-layer mantle viscosity.

CHAPTER 5

A semi-analytical solution for axisymmetric viscosity

We now show how to derive a semi-analytical solution for computing 2-D axisymmetric viscous Stokes flow in a model consisting of two eccentrically nested spheres of different viscosities. Numerical codes based on spectral or finite techniques for modeling mantle flow in a spherical geometry with lateral viscosity variations are becoming more and more popular. Hence, reliable examples for testing and validating such codes are extremely useful. In Chapter 4, the SFE approach was benchmarked against the matrix propagator solution for the case of radially symmetric viscosity. Here, the eccentrically nested sphere (ENS) solution is used to test the SFE approach for the case of axisymmetric viscosity.

The material contained in this chapter was published in Tosi & Martinec (2007).

5.1 Analytical solutions to the Stokes problem with LVV

In a spherical geometry, though an analytical solution to viscous Stokes flow with a radially symmetric viscosity distribution can be constructed by means of the matrix propagator technique (see Chapter 2), it is more difficult to find a 2-D viscosity structure for which an analytical or semi-analytical solution can be derived. In 2-D Cartesian geometry, Zhong (1996) and Trubitsyn et al. (2006) derived analytical solutions of the Stokes problem in the presence of LVV and Schmid & Podladchikov (2003) for the case of elliptical heterogeneities. In spherical geometry, no such solution is known. The special configuration of two eccentrically nested spheres (ENS) was first considered by D'Yakonov (1959) and more recently by Everett & Schultz (1995), Martinec (1999) and Velimsky & Martinec (2005) in order to construct a synthetic example for validating numerical algorithms of global-scale electromagnetic induction in the Earth. Martinec & Wolf (1999) successfully derived and used an ENS solution to validate a general code for modeling the Earth's viscoelastic relaxation with regards to glacial

isostatic adjustment. Our purpose here is to extend the family of these studies to the case of viscous Stokes flow with internal loading and to provide a synthetic example against which numerical solvers for 2-D and 3-D Stokes flow can be validated.

5.2 Stokes flow in a sphere with axisymmetric viscosity

The formulation of the Stokes problem has already been introduced and discussed extensively. However, we deal here with a full sphere (instead of a spherical shell) and the notation used will be slightly different from that used before. Hence, for the sake of clarity, we recall here the formulation of the boundary value problem, adapting it to the case of eccentrically nested spheres. The problem will be solved in a spherical axisymmetric geometry. Since for this configuration there is no dependence on the azimuthal coordinate φ, unless otherwise stated, it will always be understood that the field quantities are functions of the radius r and colatitude ϑ.

The Stokes equation under the approximation of infinite Prandtl number reads

$$\operatorname{div} \boldsymbol{\tau} + \boldsymbol{f} = 0 \ \text{ in } \mathcal{S}, \tag{5.1}$$

where $\mathcal{S}$ is now a full sphere, $\boldsymbol{f}$ is a forcing term expressing an internal load associated with lateral density anomalies and $\boldsymbol{\tau}$ is the stress tensor,

$$\boldsymbol{\tau} = -p\boldsymbol{I} + \eta(\operatorname{grad} \boldsymbol{u} + \operatorname{grad}{}^t \boldsymbol{u}), \tag{5.2}$$

where, as usual, p is the non-hydrostatic pressure, $\boldsymbol{I}$ the identity tensor, η the shear viscosity and $\boldsymbol{u}$ the flow velocity. Since the flow is assumed to be incompressible, the divergence-free constraint on $\boldsymbol{u}$ is to be satisfied,

$$\operatorname{div} \boldsymbol{u} = 0 \ \text{ in } \mathcal{S}. \tag{5.3}$$

Furthermore, impermeability and free-slip conditions (2.10) and (2.11) must be accomplished at the boundary $\partial\mathcal{S}$ of the sphere

$$\boldsymbol{u} \cdot \boldsymbol{e}_r = 0 \ \text{ on } \partial\mathcal{S}, \tag{5.4}$$

$$\boldsymbol{\tau} \cdot \boldsymbol{e}_r - (\boldsymbol{e}_r \cdot \boldsymbol{\tau} \cdot \boldsymbol{e}_r)\boldsymbol{e}_r = 0 \ \text{ on } \partial\mathcal{S}, \tag{5.5}$$

By computing the divergence of eq. (5.2), we obtain

$$\operatorname{div} \boldsymbol{\tau} = -\operatorname{grad} p + \operatorname{grad} \eta \cdot (\operatorname{grad} \boldsymbol{u} + \operatorname{grad}{}^t \boldsymbol{u}) + \eta \nabla^2 \boldsymbol{u} + \operatorname{grad} \operatorname{div} \boldsymbol{u}, \tag{5.6}$$

and eq. (5.1), using the divergence-free constraint (5.3), can be rewritten as

$$-\operatorname{grad} p + \operatorname{grad} \eta \cdot (\operatorname{grad} \boldsymbol{u} + \operatorname{grad}{}^t \boldsymbol{u}) + \eta \nabla^2 \boldsymbol{u} + \boldsymbol{f} = 0. \tag{5.7}$$

Making use of the differential identity $\nabla^2 = -\operatorname{rot}\operatorname{rot} + \operatorname{grad}\operatorname{div}$ and, again, of eq. (5.3), eq. (5.7) reads

$$-\operatorname{grad} p + \operatorname{grad} \eta \cdot (\operatorname{grad} \boldsymbol{u} + \operatorname{grad}{}^t \boldsymbol{u}) - \eta \operatorname{rot}\operatorname{rot} \boldsymbol{u} + \boldsymbol{f} = 0. \tag{5.8}$$

The vector $\boldsymbol{u}$ can then be decomposed as the sum of a spheroidal vector $\boldsymbol{u}_s$ and a toroidal vector $\boldsymbol{u}_t$ (e.g. Chandrasekhar, 1968):

$$\boldsymbol{u} = \boldsymbol{u}_s + \boldsymbol{u}_t. \tag{5.9}$$

Expanding $\boldsymbol{u}_s$ and $\boldsymbol{u}_t$ into spheroidal and toroidal vector spherical harmonics respectively (see Appendix A), we have

$$\boldsymbol{u}_s = \boldsymbol{u}_s(r,\vartheta) \equiv \sum_j \left[u_j(r)\boldsymbol{S}_j^{(-1)}(\vartheta) + v_j(r)\boldsymbol{S}_j^{(1)}(\vartheta) \right], \tag{5.10}$$

$$\boldsymbol{u}_t = \boldsymbol{u}_t(r,\vartheta) \equiv \sum_j w_j(r)\boldsymbol{S}_j^{(0)}(\vartheta), \tag{5.11}$$

where the summation for u_j runs from $j = 0$ to infinity, while the summation for w_j and v_j runs from $j = 1$ to infinity. Note that, because of the axisymmetric configuration of the problem, only terms having $m = 0$ occur and the index m is hence omitted.

Let us assume that the viscosity η is axisymmetric, that is $\eta = \eta(r,\vartheta)$. For this symmetry, the spheroidal flow $\boldsymbol{u}_s$ has only r and ϑ components, while the toroidal flow $\boldsymbol{u}_t$ has only a φ component. As a consequence, as shown by Martinec & Wolf (1999), the terms $\eta \operatorname{rot}\operatorname{rot}\boldsymbol{u}_s$ and $\eta \operatorname{rot}\operatorname{rot}\boldsymbol{u}_t$ (eq. 5.8) form, respectively, a spheroidal and a toroidal vector and, moreover, the assumption that the viscosity η has axisymmetric distribution guarantees that the term $\operatorname{grad}\eta\cdot(\operatorname{grad}\boldsymbol{u}_s + \operatorname{grad}{}^t\boldsymbol{u}_s)$ is spheroidal and the term $\operatorname{grad}\eta\cdot(\operatorname{grad}\boldsymbol{u}_t + \operatorname{grad}{}^t\boldsymbol{u}_t)$ toroidal. Therefore, if we additionally consider an internal forcing $\boldsymbol{f}$ with no toroidal component, which is consistent with the assumption of gravitational forcing, the linear momentum equation and the incompressibility condition can be written separately for $\boldsymbol{u}_s$ and $\boldsymbol{u}_t$:

$$-\operatorname{grad}p + \operatorname{grad}\eta\cdot(\operatorname{grad}\boldsymbol{u}_s + \operatorname{grad}{}^t\boldsymbol{u}_s) - \eta\operatorname{rot}\operatorname{rot}\boldsymbol{u}_s + \boldsymbol{f} = 0 \tag{5.12a}$$

$$\operatorname{div}\boldsymbol{u}_s = 0, \tag{5.12b}$$

and

$$\operatorname{grad}\eta\cdot(\operatorname{grad}\boldsymbol{u}_t + \operatorname{grad}{}^t\boldsymbol{u}_t) - \eta\operatorname{rot}\operatorname{rot}\boldsymbol{u}_t = 0 \tag{5.13a}$$

$$\operatorname{div}\boldsymbol{u}_t = 0. \tag{5.13b}$$

In addition, boundary conditions (5.5) imply that there is no surface toroidal forcing. Hence, the homogeneous system of equations (5.13) is supplemented by homogeneous boundary conditions and thus it has only the trivial solution $\boldsymbol{u}_t = 0$. Therefore, in the following, we will deal with the system (5.12) for the spheroidal flow $\boldsymbol{u}_s$ only, which from now on will be denoted by $\boldsymbol{u}$.

5.3 Analytical solution for a homogeneous sphere

Choice of the internal load

Let us assume that the sphere is homogeneous, i.e. $\operatorname{grad}\eta = 0$. A solution to eqs (5.12) will be expressed as the sum of two parts: the solution to the homogeneous

problem with $\boldsymbol{f} = 0$ and a particular solution with $\boldsymbol{f} \neq 0$:

$$p = p^0 + p', \tag{5.14}$$

$$\boldsymbol{u} = \boldsymbol{u}^0 + \boldsymbol{u}', \tag{5.15}$$

where the labels ^{0} and $'$ denote the homogeneous solution and a particular solution, respectively. Eq. (5.12a) can then be written as

$$-\operatorname{grad} p^0 - \operatorname{grad} p' - \eta \operatorname{rot}\operatorname{rot} \boldsymbol{u}^0 - \eta \operatorname{rot}\operatorname{rot} \boldsymbol{u}' + \boldsymbol{f} = 0. \tag{5.16}$$

The spherical harmonic representations of the field variables considered read as

$$p^0 = p^0(r,\vartheta) = \sum_j p_j^0(r) Y_j(\vartheta), \tag{5.17}$$

$$p' = p'(r,\vartheta) = \sum_j p_j'(r) Y_j(\vartheta), \tag{5.18}$$

$$\boldsymbol{u}^0 = \boldsymbol{u}^0(r,\vartheta) = \sum_j \left[u_j^0(r) \boldsymbol{S}_j^{(-1)}(\vartheta) + v_j^0 \boldsymbol{S}_j^{(1)} \right], \tag{5.19}$$

$$\boldsymbol{u}' = \boldsymbol{u}'(r,\vartheta) = \sum_j \left[u_j'(r) \boldsymbol{S}_j^{(-1)}(\vartheta) + v_j'(r) \boldsymbol{S}_j^{(1)}(\vartheta) \right]. \tag{5.20}$$

Making use of various relations for differential operators for scalar and vector spherical harmonics (see Appendix A), it can be shown that eq. (5.16) is equivalent to

$$\begin{aligned} &- \operatorname{grad} p^0 - \eta \operatorname{rot}\operatorname{rot} \boldsymbol{u}^0 - \sum_j \left[\frac{dp_j'}{dr} - \eta \frac{J}{r} \left(-\frac{u_j'}{r} + \frac{dv_j'}{dr} + \frac{v_j'}{r} \right) \right] \boldsymbol{S}_j^{(-1)} \\ &- \sum_j \left[\frac{p_j'}{r} + \eta \left(\frac{1}{r}\frac{du_j'}{dr} - \frac{d^2 v_j'}{dr^2} - \frac{2}{r}\frac{dv_j'}{dr} \right) \right] \boldsymbol{S}_j^{(1)} + \sum_j f_j \boldsymbol{S}_j^{(-1)} = 0, \end{aligned} \tag{5.21}$$

where $J \equiv j(j+1)$, and we have assumed that the forcing has a radial component only, i.e. $\boldsymbol{f} = f\, \boldsymbol{e}_r$. Because of this assumption, the radially dependent coefficient standing at $\boldsymbol{S}_j^{(1)}$ in eq. (5.21) must vanish. This requirement is satisfied when

$$p_j'(r) = \eta \left(r \frac{d^2 v_j'}{dr^2} + 2 \frac{dv_j'}{dr} - \frac{du_j'}{dr} \right). \tag{5.22}$$

Substituting (5.22) into (5.21), we obtain

$$\begin{aligned} &- \operatorname{grad} p^0 - \eta \operatorname{rot}\operatorname{rot} \boldsymbol{u}^0 - \eta \sum_j \left[\left(r \frac{d^3 v_j'}{dr^3} + 3 \frac{d^2 v_j'}{dr^2} - \frac{d^2 u_j'}{dr^2} \right) \right. \\ &\left. + \frac{J}{r} \left(\frac{u_j'}{r} - \frac{v_j'}{r} - \frac{dv_j'}{dr} \right) - f_j \right] \boldsymbol{S}_j^{(-1)} = 0. \end{aligned} \tag{5.23}$$

Therefore, if an internal load is prescribed in such a way that

$$f_j(r) = \eta \left[r\frac{d^3 v'_j}{dr^3} + 3\frac{d^2 v'_j}{dr^2} - \frac{d^2 u'_j}{dr^2} + \frac{J}{r}\left(\frac{u'_j}{r} - \frac{v'_j}{r} - \frac{dv'_j}{dr} \right) \right], \tag{5.24}$$

eq. (5.23) is reduced to the homogeneous equation of the form

$$-\mathrm{grad}\, p^0 - \eta\, \mathrm{rot}\, \mathrm{rot}\, \boldsymbol{u}^0 = 0. \tag{5.25}$$

Homogeneous solution

We now determine a homogeneous solution to eq. (5.25). First, let us apply the rotation operator to eq. (5.25), from which we obtain

$$\mathrm{rot}\, \mathrm{rot}\, \mathrm{rot}\, \boldsymbol{u}^0 = 0. \tag{5.26}$$

Since $\boldsymbol{u}^0$ is a spheroidal vector, it can be expressed as the rotation of a toroidal vector potential $\boldsymbol{A}$ (Chandrasekhar, 1968):

$$\boldsymbol{u}^0 = \mathrm{rot}\, \boldsymbol{A}. \tag{5.27}$$

Hence, eq. (5.26) can be written in terms of $\boldsymbol{A}$ as

$$\mathrm{rot}\, \mathrm{rot}\, \mathrm{rot}\, \mathrm{rot}\, \boldsymbol{A} = 0, \tag{5.28}$$

or, alternatively, being $\mathrm{div}\, \boldsymbol{A} = 0$, as the biharmonic differential equation for $\boldsymbol{A}$:

$$\nabla^4 \boldsymbol{A} = 0. \tag{5.29}$$

Since $\mathrm{div}\, \boldsymbol{A} = 0$, $\boldsymbol{A}$ must be function of the toroidal vector spherical harmonics $\boldsymbol{S}_j^{(0)}$, as these are the only ones with zero divergence. If we look for solutions to eq. (5.29) of the type $r^k \boldsymbol{S}_j^{(0)}$, it can be shown that the constant k must take one of the four values $k = j,\ j+2,\ -j-1,\ -j+1$. The fundamental solution to eq. (5.29) can then be written as follows:

$$\boldsymbol{A}(r,\vartheta) = \sum_j (A_{1,j} r^j + A_{2,j} r^{j+2} + A_{3,j} r^{-j-1} + A_{4,j} r^{-j+1}) \boldsymbol{S}_j^{(0)}(\vartheta), \tag{5.30}$$

where $A_{i,j}$ $(i = 1, \ldots, 4)$ are constants. Using eq. (A.17) for the rotation of eq. (5.30) and considering eq. (5.19), the spherical harmonic coefficients of the radial and tangential components of the velocity $\boldsymbol{u}^0$ can be expressed as

$$u_j^0(r) = -j(j+1)(A_{1,j} r^{j-1} + A_{2,j} r^{j+1} + A_{3,j} r^{-j-2} + A_{4,j} r^{-j}), \tag{5.31}$$

$$\begin{aligned} v_j^0(r) = &-(j+1) A_{1,j} r^{j-1} - (j+3) A_{2,j} r^{j+1} \\ &+ j A_{3,j} r^{-j-2} + (j-2) A_{4,j} r^{-j}. \end{aligned} \tag{5.32}$$

Taking the divergence of eq. (5.25), we readily obtain a Laplace equation for the pressure p^0:

$$\nabla^2 p^0 = 0. \tag{5.33}$$

Its solution can then be written in terms of scalar spherical harmonics:

$$p^0(r,\vartheta) = \eta \sum_j (C_{1,j} r^j + C_{2,j} r^{-j-1})\, Y_j(\vartheta), \tag{5.34}$$

where η has been introduced for normalization. Substituting the expansions (5.31), (5.32) and (5.34) into eq. (5.25), it can be shown that the constants $C_{1,j}$ and $C_{2,j}$ can be expressed in terms of $A_{2,j}$ and $A_{4,j}$ as

$$C_{1,j} = -2(j+1)(2j+3)A_{2,j}, \tag{5.35}$$
$$C_{2,j} = -2j(2j-1)A_{4,j}. \tag{5.36}$$

Hence p^0 becomes

$$p^0(r,\vartheta) = \eta \sum_j \big[-2(j+1)(2j+3)A_{2,j} r^j - 2j(2j-1)A_{4,j} r^{-j-1} \big]\, Y_j(\vartheta). \tag{5.37}$$

Particular solution

So far, we have found the explicit expression for the homogeneous solutions $\boldsymbol{u}^0$ and p^0 to eq. (5.25). To determine the complete solutions $\boldsymbol{u}$ and p, one particular solution $\boldsymbol{u}'$ and p' for forcing of the form (5.24) must be specified. We first assume that the coefficients u'_j and v'_j of the particular solutions $\boldsymbol{u}'$ have the following form

$$u'_j(r) = F_j r^k, \tag{5.38}$$
$$v'_j(r) = G_j r^k, \tag{5.39}$$

where k is a positive integer and F_j and G_j are constants that do not depend on r and control the amplitude of u'_j and v'_j, respectively. In addition, the incompressibility condition $\operatorname{div} \boldsymbol{u}' = 0$ for the particular solution $\boldsymbol{u}'$ implies that the coefficients F_j and G_j cannot be chosen independently of each other. The spherical harmonic expansion of the divergence of $\boldsymbol{u}'$ reads as (see eqs (A.18) and (A.19))

$$\operatorname{div} \boldsymbol{u}' = \sum_j \left(\frac{du'_j}{dr} + \frac{2}{r} u'_j - \frac{J}{r} v'_j \right) Y_j(\vartheta). \tag{5.40}$$

Eq. $\operatorname{div} \boldsymbol{u}' = 0$ is satisfied when

$$\frac{du'_j}{dr} + \frac{2}{r} u'_j - \frac{J}{r} v'_j = 0. \tag{5.41}$$

After substituting from eqs (5.38) and (5.39) into eq. (5.41), the divergence-free constraint on $\boldsymbol{u}'$ yields

$$G_j = F_j \frac{k+2}{J}. \tag{5.42}$$

With this choice, the forcing (5.24) that ensures the validity of the homogeneous equation (5.25) has the following coefficients:

$$f_j(r) = \eta \frac{F_j}{J} \left[k^4 + 2k^3 - (2J+1)k^2 - 2(J+1)k + J(J-2)\right] r^{k-2}. \tag{5.43}$$

Finally, eq. (5.22) yields the particular solution for the pressure

$$p'_j(r) = \eta \frac{F_j}{J} \left[k^3 + 3k^2 + (2-J)k\right] r^{k-1}. \tag{5.44}$$

5.4 Solution for two eccentrically nested spheres

In the previous section, we derived a homogeneous and a particular solution to the Stokes problem in a homogeneous sphere for a particular choice of forcing expressed by the coefficients (5.43). In this section, we will use these solutions for the case of two eccentrically nested spheres with different viscosities.

Let us consider the axisymmetric configuration of two eccentrically nested spheres shown in Fig. 5.1. A large sphere $\mathcal{S}_1$ of radius R_1 and center $\mathcal{O}_1$ contains a smaller sphere $\mathcal{S}_2$ of radius R_2, whose center $\mathcal{O}_2$ is shifted along the z-axis by a distance $\boldsymbol{d}$. We now express the solution for the two spheres in the reference frame of $\mathcal{O}_2$.

In the reference frame $\mathcal{O}_2$, the toroidal vector potential inside $\mathcal{S}_1$ (indicated by the superscript (1)), but outside $\mathcal{S}_2$, reads as

$$\begin{aligned}\boldsymbol{A}^{(1)}(r_2, \vartheta_2) = \sum_j (&A_{3,j} r_2^j + A_{4,j} r_2^{j+2} \\ &+ A_{5,j} r_2^{-j-1} + A_{6,j} r_2^{-j+1}) \boldsymbol{S}_j^{(0)}(\vartheta_2),\end{aligned} \tag{5.45}$$

where the dependence on r_2 and ϑ_2 is written explicitely to emphasize that the solution is expressed in the coordinate system $\mathcal{O}_2$. On the other hand, the toroidal vector potential inside $\mathcal{S}_2$, but outside $\mathcal{S}_1$ is

$$\boldsymbol{A}^{(2)}(r_2, \vartheta_2) = \sum_j (A_{1,j} r_2^j + A_{2,j} r_2^{j+2}) \boldsymbol{S}_j^{(0)}(\vartheta_2). \tag{5.46}$$

Note that the expression (5.46) does not contain the harmonics $r_2^{-j-1}\boldsymbol{S}_j^{(0)}$ and $r_2^{-j+1}\boldsymbol{S}_j^{(0)}$ because they are singular at the origin $\mathcal{O}_2$ where $r_2 \to 0$.

Let us confine ourselves to the case where the forcing $\boldsymbol{f}$ is concentrated only inside the inner sphere $\mathcal{S}_2$ and directed towards its center, i.e.

$$\boldsymbol{f} = \boldsymbol{f}(r_2, \vartheta_2) = f(r_2, \vartheta_2)\boldsymbol{e}_{r_2} \neq 0 \qquad \text{if } (r_2, \vartheta_2) \in \mathcal{S}_2, \tag{5.47}$$

$$\boldsymbol{f} = 0 \qquad \text{otherwise.} \tag{5.48}$$

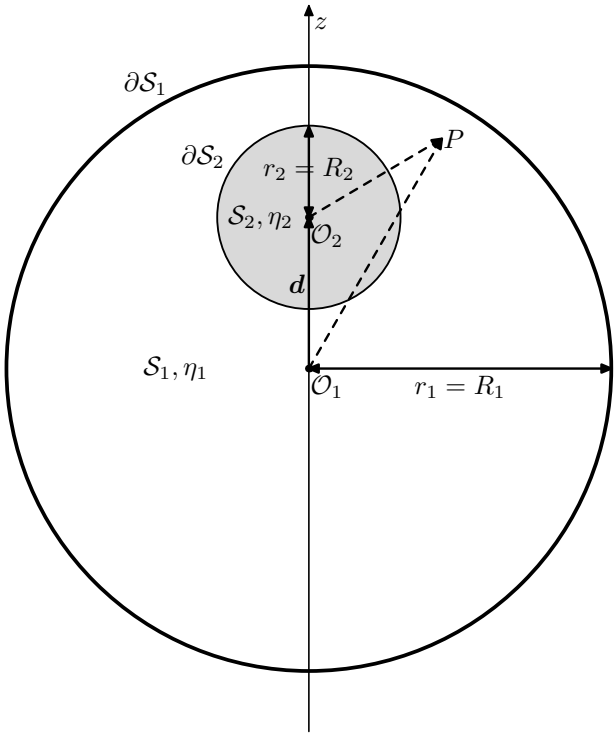

Figure 5.1: Geometry of the two eccentrically nested spheres. The outer sphere of radius R_1 and viscosity η_1 is centered at $\mathcal{O}_1$, representing the origin of a spherical coordinate system $\mathcal{O}_1(r_1, \vartheta_1, \varphi_1)$. The grey sphere $\mathcal{S}_2$ of viscosity η_2 is centered at $\mathcal{O}_2$, representing the origin of a spherical coordinate system $\mathcal{O}_2(r_2, \vartheta_2, \varphi_2)$ shifted by the vector $\boldsymbol{d}$ along the z-axis.

This assumption implies that the homogeneous solution is applied in the sphere $\mathcal{S}_1$, while both homogeneous and particular solutions are applied in the sphere $\mathcal{S}_2$. The two components of the velocity and pressure in $\mathcal{S}_1$ can then be expressed as

$$\begin{aligned} u_j^{(1)}(r_2) =& u_j^{(1)0}(r_2) \\ =& -j(j+1)(A_{3,j} r_2^{j-1} + A_{4,j} r_2^{j+1} + A_{5,j} r_2^{-j-2} + A_{6,j} r_2^{-j}), \end{aligned} \tag{5.49}$$

$$\begin{aligned} v_j^{(1)}(r_2) =& v_j^{(1)0}(r_2) \\ =& -(j+1)A_{3,j} r_2^{j-1} - (j+3)A_{4,j} r_2^{j+1} && (5.50) \\ & + jA_{5,j} r_2^{-j-2} + (j-2)A_{6,j} r_2^{-j}, && (5.51) \end{aligned}$$

$$\begin{aligned} p_j^{(1)}(r_2) =& p_j^{(1)0}(r_2) \\ =& \eta_1 \left[-2(j+1)(2j+3)A_{4,j} r_2^j - 2j(2j-1)A_{6,j} r_2^{-j-1} \right], \end{aligned} \tag{5.52}$$

while, in $\mathcal{S}_2$, it holds that

$$\begin{aligned} u_j^{(2)}(r_2) =& u_j^{(2)0}(r_2) + u_j^{(2)\prime}(r_2) \\ =& -j(j+1)(A_{1,j} r_2^{j-1} + A_{2,j} r_2^{j+1}) + F_j r_2^k, \end{aligned} \tag{5.53}$$

$$\begin{aligned} v_j^{(2)}(r_2) =& v_j^{(2)0}(r_2) + v_j^{(2)\prime}(r_2) \\ =& -(j+1)A_{1,j} r_2^{j-1} - (j+3)A_{2,j} r_2^{j+1} + F_j \frac{k+2}{J} r_2^k, \end{aligned} \tag{5.54}$$

$$\begin{aligned} p_j^{(2)}(r_2) =& p_j^{(2)0}(r_2) + p_j^{(2)\prime}(r_2) \\ =& \eta_2 \left[-2(j+1)(2j+3)A_{2,j} r_2^j + \frac{F_j}{J}(k^3 + 3k^2 + (2-J)k) r_2^{k-1} \right]. \end{aligned} \tag{5.55}$$

We additionally need an expression for the radial $\tau_{rr,j}$ and tangential $\tau_{r\vartheta,j}$ components of the stress vector $\boldsymbol{e}_r \cdot \boldsymbol{\tau}$. They can be expressed as follows:

$$\begin{aligned} \tau_{rr,j}^{(1)}(r_2) =& -p_j^{(1)0} + 2\eta_1 \frac{du_j^{(1)0}}{dr_2} \\ =& -2\eta_1 [j(j^2-1)A_{3,j} r_2^{j-2} + (j+1)(j^2-j-3)A_{4,j} r_2^j \\ & - j(j+1)(j+2)A_{5,j} r_2^{-j-3} - j(j^2+3j-1)A_{6,j} r_2^{-j-1}], \end{aligned} \tag{5.56}$$

$$\begin{aligned} \tau_{r\vartheta,j}^{(1)}(r_2) =& \eta_1 \left(\frac{dv_j^{(1)0}}{dr_2} - \frac{v_j^{(1)0}}{r_2} + \frac{u_j^{(1)0}}{r_2} \right) \\ =& -2\eta_1 [(j^2-1)A_{3,j} r_2^{j-2} + j(j+2)A_{4,j} r_2^j \\ & + j(j+2)A_{5,j} r_2^{-j-3} + (j^2-1)A_{6,j} r_2^{-j-1}], \end{aligned} \tag{5.57}$$

$$\begin{aligned} \tau_{rr,j}^{(2)}(r_2) =& -p_j^{(2)0} - p_j^{(2)\prime} + 2\eta_2 \left(\frac{du_j^{(2)0}}{dr_2} + \frac{du_j^{(2)\prime}}{dr_2} \right) \\ =& -2\eta_2 \Big[j(j^2-1)A_{1,j} r_2^{j-2} + (j+1)(j^2-j-3)A_{2,j} r_2^j \\ & + \frac{F_j}{2J}(k^3 + 3k^2 + (2-3J)k) r_2^{k-1} \Big], \end{aligned} \tag{5.58}$$

$$\begin{aligned}\tau^{(2)}_{r\vartheta,j}(r_2) =&\eta_2\left(\frac{dv_j^{(2)0}}{dr_2}+\frac{dv_j^{(2)\prime}}{dr_2}-\frac{v_j^{(2)0}}{r_2}-\frac{v_j^{(2)\prime}}{r_2}+\frac{u_j^{(2)0}}{r_2}+\frac{u_j^{(2)\prime}}{r_2}\right)\\ =&-2\eta_2\Big[(j^2-1)A_{1,j}r_2^{j-2}+j(j+2)A_{2,j}r_2^j\\ &-\frac{F_j}{2J}(k^2+k-2+J)r_2^{k-1}\Big].\end{aligned} \tag{5.59}$$

To find the solution for the axisymmetric configuration consisting of the sphere $\mathcal{S}_2$ embedded in $\mathcal{S}_1$, it is necessary to connect continuously the above solutions derived separately for the two spheres (eqs 5.49-5.58) at the interface $r_2 = R_2$. For this purpose, we first require the continuity of the velocity $\boldsymbol{u}$ at $r_2 = R_2$, i.e., for every degree j it holds $u_j^{(1)}(R_2) = u_j^{(2)}(R_2)$ and $v_j^{(1)}(R_2) = v_j^{(2)}(R_2)$. From eqs (5.49) and (5.53), the first condition reads as

$$\begin{aligned}&A_{3,j}R_2^{j-1}+A_{4,j}R_2^{j+1}+A_{5,j}R_2^{-j-2}+A_{6,j}R_2^{-j}\\ &=A_{1,j}R_2^{j-1}+A_{2,j}R_2^{j+1}-\frac{F_j}{J}R_2^k\end{aligned} \tag{5.60}$$

and from eqs (5.67) and (5.54), the second condition takes the form

$$\begin{aligned}&(j+1)A_{3,j}R_2^{j-1}+(j+3)A_{4,j}R_2^{j+1}-jA_{5,j}R_2^{-j-2}-(j-2)A_{6,j}R_2^{-j}\\ &=(j+1)A_{1,j}R_2^{j-1}+(j+3)A_{2,j}R_2^{j+1}-F_j\frac{k+2}{J}R_2^k.\end{aligned} \tag{5.61}$$

Second, the stress vector $\boldsymbol{e}_r\cdot\boldsymbol{\tau}$ must also be continuous at $r_2 = R_2$, i.e. $\tau^{(1)}_{rr,j}(R_2) = \tau^{(2)}_{rr,j}(R_2)$ and $\tau^{(1)}_{r\vartheta,j}(R_2) = \tau^{(2)}_{r\vartheta,j}(R_2)$. Hence, from eqs (5.56) and (5.58), we obtain

$$\begin{aligned}&\eta_1\Big[j(j^2-1)A_{3,j}R_2^{j-2}+(j+1)(j^2-j-3)A_{4,j}R_2^j-\\ &\quad j(j+1)(j+2)A_{5,j}R_2^{-j-3}-j(j^2+3j-1)A_{6,j}R_2^{-j-1}\Big]\\ &=\eta_2\Big[j(j^2-1)A_{1,j}R_2^{j-2}+(j+1)(j^2-j-3)A_{2,j}R_2^j\\ &\quad+\frac{F_j}{2J}(k^3+3k^2+(2-3J)k)R_2^{k-1}\Big]\end{aligned} \tag{5.62}$$

and from eqs (5.57) and (5.59), we obtain

$$\begin{aligned}&\eta_1\Big[(j^2-1)A_{3,j}R_2^{j-2}+j(j+2)A_{4,j}R_2^j\\ &\quad+j(j+2)A_{5,j}R_2^{-j-3}+(j^2-1)A_{6,j}R_2^{-j-1}\Big]\\ &=\eta_2\left[(j^2-1)A_{1,j}R_2^{j-2}+j(j+2)A_{2,j}R_2^j-\frac{F_j}{2J}(k^2+k-2+J)R_2^{k-1}\right].\end{aligned} \tag{5.63}$$

The unknowns of our problem consist of the six j-dependent coefficients $A_{i,j}$ ($i = 1, \ldots, 6$) that fully specify the vector potentials (5.45) and (5.46). Equations (5.60)-(5.63) for each degree j represent only four conditions and the other two conditions have to be specified. They consist of the boundary conditions (5.4) and (5.5) prescribed on the surface of $\mathcal{S}_1$. However, the toroidal vector potential (5.45) is expressed in the coordinate system $\mathcal{O}_2$, while the conditions (5.4) and (5.5) are given in the coordinate system $\mathcal{O}_1$. Hence, we need to transform the solution $\boldsymbol{A}^{(1)}(r_2, \vartheta_2)$ to the system (r_1, ϑ_1) connected with sphere $\mathcal{S}_1$. For this purpose, we first notice that the toroidal vector spherical harmonics can be expressed in terms of the associated Legendre function of the first order $P_{j1}(\cos\vartheta)$ as

$$\boldsymbol{S}_j^{(0)}(\vartheta_2) = \sqrt{J} P_{j1}(\cos\vartheta_2)\boldsymbol{e}_{V_2} \tag{5.64}$$

and that $\boldsymbol{e}_{\varphi_1} = \boldsymbol{e}_{\varphi_2}$ for the case of a translation along the z-axis. Then, by making use of the transformation theorems for solid spherical harmonics (see Appendix A.3), it can be shown that, in the coordinate system $\mathcal{O}_1$, $\boldsymbol{A}^{(1)}$ takes the following form:

$$\begin{aligned}\boldsymbol{A}^{(1)}(r_1, \vartheta_1) = \sum_{j,j_1=1}^{\infty} \sqrt{\frac{J_1}{J}} \Big[& \Gamma^{1,0}_{j_1 j}(d) A_{3,j_1} r_1^{j} + \Gamma^{1,2}_{j_1 j}(d, r_1) A_{4,j_1} r_1^{j} \\ & + D^{1,0}_{j_1 j}(d) A_{5,j_1} r_1^{-j-1} + D^{1,2}_{j_1 j}(d, r_1) A_{6,j_1} r_1^{-j-1} \Big] \boldsymbol{S}_j^{(0)}(\vartheta_1),\end{aligned} \tag{5.65}$$

where $\Gamma^{m,k}_{j_1 j}$ and $D^{m,k}_{j_1 j}$ are subsets of the Clebsch-Gordan coefficients $C^{jm}_{j_1 m j_2 0}$ that are defined in Appendix A.3 (here, the indeces j and j_1 have been labeled by j_1 and j, respectively).

By taking the rotation of eq. (5.65), it follows that

$$\begin{aligned}u_j^{(1)}(r_1) = - \sum_{j_1=1}^{\infty} \sqrt{J J_1} \Big[& \Gamma^{1,0}_{j_1 j}(d) A_{3,j_1} r_1^{j-1} + \Gamma^{1,2}_{j_1 j}(d, r_1) A_{4,j_1} r_1^{j-1} \\ & + D^{1,0}_{j_1 j}(d) A_{5,j_1} r_1^{-j-2} + D^{1,2}_{j_1 j}(d, r_1) A_{6,j_1} r_1^{-j-2} \Big],\end{aligned} \tag{5.66}$$

$$\begin{aligned}v_j^{(1)}(r_1) = - \sum_{j_1=1}^{\infty} \sqrt{\frac{J_1}{J}} \Big\{ & (j+1)\Gamma^{1,0}_{j_1 j}(d) A_{3,j_1} r_1^{j-1} \\ & + \Big[(j+1)\Gamma^{1,2}_{j_1 j}(d, r_1) + \gamma^{1,2}_{j_1 j}(d, r_1) \Big] A_{4,j_1} r_1^{j-1} \\ & - j D^{1,0}_{j_1 j}(d) A_{5,j_1} r_1^{-j-2} - \Big[j D^{1,2}_{j_1 j}(d, r_1) - d^{1,2}_{j_1 j}(d, r_1) \Big] A_{6,j_1} r_1^{-j-2} \Big\},\end{aligned} \tag{5.67}$$

while the spherical harmonics of the tangential component of the stress vector are given by

$$\begin{aligned}\tau^{(1)}_{r\vartheta,j}(r_1) =&\eta_1\left(\frac{dv^{(1)}_j(r_1)}{dr_1}-\frac{v^{(1)}_j(r_1)}{r_1}+\frac{u^{(1)}_j(r_1)}{r_1}\right)\\ =&-2\eta_1\sum_{j_1=1}^{\infty}\sqrt{\frac{J_1}{J}}\Big\{(j^2-1)\Gamma^{1,0}_{j_1\,j}(d)A_{3,j_1}r_1^{j-2}\\ &+\left[\frac{1}{2}(2j+1)\gamma^{1,2}_{j_1\,j}(d,r_1)+(j^2-1)\Gamma^{1,2}_{j_1\,j}(d,r_1)\right]A_{4,j_1}r_1^{j-2}\\ &+j(j+2)D^{1,0}_{j_1\,j}(d)A_{5,j_1}r_1^{-j-3}\\ &-\left[\frac{1}{2}(2j+1)d^{1,2}_{j_1\,j}(d,r_1)-j(j+2)D^{1,2}_{j_1\,j}(d,r_1)\right]A_{6,j_1}r_1^{-j-3}\Big\}.\end{aligned} \tag{5.68}$$

The boundary condition (5.4) is equivalent to $u^{(1)}_j(R_1)=0$ for each degree j, i.e.

$$\begin{aligned}&\sum_{j_1=1}^{\infty}\sqrt{J_1}\big[\Gamma^{1,0}_{j_1\,j}(d)A_{3,j_1}R_1^{j-1}+\Gamma^{1,2}_{j_1\,j}(d,R_1)A_{4,j_1}R_1^{j-1}\\ &+D^{1,0}_{j_1\,j}(d)A_{5,j_1}R_1^{-j-2}+D^{1,2}_{j_1\,j}(d,R_1)A_{6,j_1}R_1^{-j-2}\big]=0,\end{aligned} \tag{5.69}$$

while the condition (5.5) is equivalent to $\tau^{(1)}_{r\vartheta,j}(R_1)=0$ for each degree j, i.e.

$$\begin{aligned}&\sum_{j_1=1}^{\infty}\sqrt{J_1}\Big\{(j^2-1)\Gamma^{1,0}_{j_1\,j}(d)A_{3,j_1}R_1^{j-2}\\ &+\left[\frac{1}{2}(2j+1)\gamma^{1,2}_{j_1\,j}(d,R_1)+(j^2-1)\Gamma^{1,2}_{j_1\,j}(d,R_1)\right]A_{4,j_1}R_1^{j-2}\\ &+j(j+2)D^{1,0}_{j_1\,j}(d)A_{5,j_1}R_1^{-j-3}\\ &-\left[\frac{1}{2}(2j+1)d^{1,2}_{j_1\,j}(d,R_1)-j(j+2)D^{1,2}_{j_1\,j}(d,R_1)\right]A_{6,j_1}R_1^{-j-3}\Big\}=0.\end{aligned} \tag{5.70}$$

eqs (5.60)-(5.63), together with eqs (5.69) and (5.70) form, for each degree j, a system of six linear equation for the six unknown coefficients $A_{i,j}$, providing the solution to the BVP (5.1)-(5.5) for viscous Stokes flow.

It is worth noting that, instead of free-slip boundary conditions, *no-slip* conditions (i.e. $\boldsymbol{u}=0$ on $\partial\mathcal{S}$) can also be easily treated by simply replacing eq. (5.70) with the condition $v^{(1)}_j(R_1)=0$ which is readily obtained using eq. (5.67).

5.5 Geoid computation

The ENS solution finds its most natural application as a synthetic example for testing numerical codes designed to compute surface geophysical observables,

such as the geoid, given a known internal density distribution. Therefore, for benchmark purposes, it is interesting to show how to compute this quantity for the ENS configuration.

Let us start by considering the gravitational potential due to internal anomalies. If we were to model the Earth with real parameters, eq. (5.47) should have been written as $\boldsymbol{f} = f(r_2, \vartheta_2)\, g_0 \boldsymbol{e}_{r_2}$, with g_0 denoting the reference gravity acceleration and f the actual density anomaly distribution. However, in our semi-analytical example, we set $g_0 = 1$. The gravitational potential inside the sphere $\mathcal{S}_1$, expressed in the reference frame $\mathcal{O}_2$, is given by the Newton's law

$$V^{(1)}_{\text{int}}(r_2, \vartheta_2) = G \int_0^{2\pi}\int_0^{\pi}\int_0^{R_2} \frac{f(r_2', \vartheta_2')}{L}\, r_2'^2\, \sin\vartheta_2' dr_2' d\vartheta_2' d\varphi_2', \tag{5.71}$$

where the integration is carried out over the volume of $\mathcal{S}_2$, G is the constant of gravitation, f is the density within $\mathcal{S}_2$, whose coefficients are given by eq. (5.43), (r_2', ϑ_2') indicate the position of the source of the density anomaly in $\mathcal{S}_2$ and L is the angular distance between the observation point (r_2, ϑ_2) and the source point (r_2', ϑ_2'). The inverse of the angular distance $1/L$ can be expressed by means of the addition theorem for spherical harmonics (e.g. Varshalovich et al., 1989), which, for the case $r_2 > r_2'$, reads as

$$\frac{1}{L} = \sum_j \frac{4\pi}{2j+1} \frac{r_2'}{r_2^{j+1}}\, Y_j(\vartheta_2) Y_j(\vartheta_2'). \tag{5.72}$$

Using eq. (5.72), the expansion coefficients (5.43), the orthogonality of spherical harmonics, and by performing the integration in (5.71) analytically, we obtain:

$$\begin{aligned} V^{(1)}_{\text{int}}(r_2,\vartheta_2) = {} & 8\pi^2 G \sum_j \eta_2 F_j R_2^{k+j+1} \\ & \times \frac{[k^4 + 2k^3 - (2J+1)k^2 - 2(J+1)k + J(J-2)]}{J(2j+1)(k+j)} r_2^{-j-1} Y_j(\vartheta_2). \end{aligned} \tag{5.73}$$

On the other hand, the gravitational potential $V^{(1)}_{\text{def}}$ due to the density anomalies associated with the deformation of $\partial\mathcal{S}_1$ is proportional to the traction τ_{rr} at $r_1 = R_1$. In the reference frame $\mathcal{O}_1$, it reads (e.g. Forte & Peltier, 1991)

$$V^{(1)}_{\text{def}}(R_1, \vartheta_1) = -\frac{4\pi G R_1}{g_0} \sum_j \frac{\tau^{(1)}_{rr,j}(R_1)}{2j+1} Y_j(\vartheta_1), \tag{5.74}$$

where, again, we set $g_0 = 1$. The total gravitational potential $V^{(1)}(r_1, \vartheta_1)$ is given by the sum of the contributions from each density anomaly. After transforming eq. (5.73) to the reference system $\mathcal{O}_1$ and evaluating it at the surface $r_1 = R_1$, we can write:

$$V^{(1)}(R_1, \vartheta_1) = V^{(1)}_{\text{int}}(R_1, \vartheta_1) + V^{(1)}_{\text{def}}(R_1, \vartheta_1), \tag{5.75}$$

which yields the expression for the geoid.

5.6 Comparison with SFE solution

The linear system of eqs (5.60)-(5.63), (5.69) and (5.70) is characterized by a $6j_{\max}^{\mathrm{ENS}} \times 6j_{\max}^{\mathrm{ENS}}$-matrix, where $j_{\max}^{\mathrm{ENS}}$ is the cut-off degree chosen to truncate the infinite harmonic series (5.45) and (5.46). We solve it for $A_{i,j}$ $i = 1, \ldots, 6$, $j = 1, \ldots j_{\max}^{\mathrm{ENS}}$, by Gauss-Jordan elimination (e.g. Stoer & Bulirsch, 2002). In the following, we discuss a comparison between the ENS and SFE solutions of the problem. Since we deal here with a full sphere, the SFE solution needs a small modification to be adapted to this geometry. Removing the boundary integral over the CMB (see eq. 3.29) is sufficient to satisfy the Stokes BVP in a sphere $\mathcal{S}$.

Model	R_1 (m)	R_2 (m)	d (m)	η_1 (Pa s)	η_2 (Pa s)	$j_{\max}^{\mathrm{ENS}}$	$j_{\max}^{\mathrm{SFE}}$	N_{FE}
1-D	1	0.3	0	1	50	2	2	100
2-D1	1	0.3	0.5	1	50	20	20	200
2-D2	1	0.3	0.5	1	200	20	20	350
2-D3	1	0.2	0.5	1	2000	20	40	500

Table 5.1: Description of the models employed in this work. According to different values of the viscosity contrast and to the position and size of the inner sphere, one radially-symmetric model (1-D) and three axisymmetric models (2-D1, 2-D2, 2-D3) are examined. $j_{\max}^{\mathrm{ENS}}$ denotes the cut-off degree chosen to truncate the infinite series of the ENS solutions, $j_{\max}^{\mathrm{SFE}}$ is the cut-off degree employed for the spherical harmonic expansions of the SFE solution and N_{FE} is the number of finite elements that span the radius of the SFE solution.

Four different examples are presented, which differ either by the geometrical configuration of the spheres or their viscosity (see Table 5.1). Numerical underflow or overflow may arise when computing the coupling coefficients $\Gamma_{jj_1}^{m,k}(d,r)$ and $D_{jj_1}^{m,k}(d,r)$ for radii r that are far from the unity. Thus, in our examples, we keep the radius of sphere $\mathcal{S}_1$ equal to 1 m. Moreover, since our study is related to modeling of the geoid, which is only sensitive to relative contrasts in viscosity, and not to their absolute values, we fix the viscosity of $\mathcal{S}_1$ to 1 Pa s and vary the viscosity of $\mathcal{S}_2$. In all examples shown, the flow is excited by a degree-2 load ($j = j_{\mathrm{load}} = 2$) in eq. (5.43) and the exponent k of the particular solution is chosen to be $k = 5$. The amplitude F_j that appears in the expression (5.43) of the forcing is kept equal to 10^{-3} for all of the examples considered.

To check the correctness of the ENS solution, we first analyze the simple case where the centers of the two spheres coincide and the viscosity distribution is radially symmetric. The results for an inner sphere of viscosity 50 Pa s are shown in Fig. 5.2. The distribution of the radial component of the internal forcing as seen in $\mathcal{O}_1$ is plotted in Fig. 5.2a and varies approximately between -0.08 and +0.08 N/m^3 for the particular choice of F_j, j and k that we introduced above. The flow pattern in Fig. 5.2a shows that, as expected, the material tends to sink where the density anomalies are positive (blue areas) and to rise where the

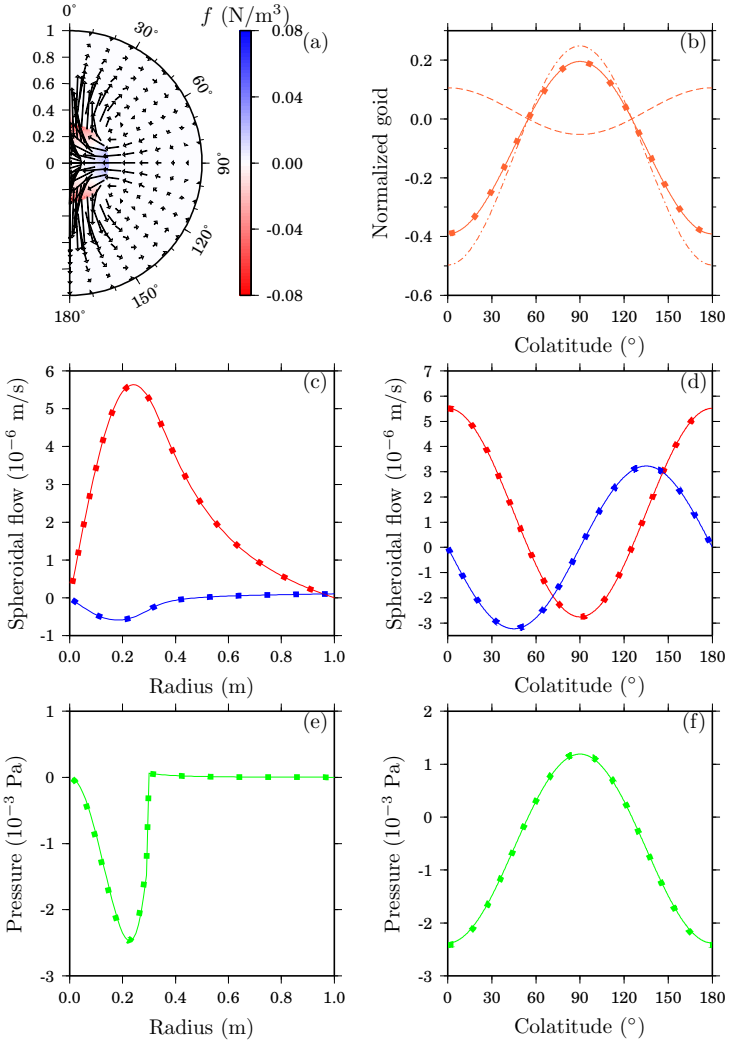

Figure 5.2: Numerical results for the 1-D model (see Table 5.1). Solid lines indicate the ENS solutions, while squares are the SFE solution. Panel a: Flow pattern and density anomaly; panel b: Total geoid (solid line for ENS and squares for SFE), geoid due to internal anomaly (dashed-dotted line) and to boundary deformation (dashed line); panel c: Radial cross sections for radial flow (in red) and tangential flow (in blue); panel d: Angular cross section for for radial flow (in red) and tangential flow (in blue); panel e: Radial cross section for pressure; panel d: Angular cross section for pressure.

anomalies are negative (red areas). In panels b, c, d, e and f of Figures 5.2-5.5, the solid line always represents the ENS solution, while the squares are the SFE solution. In Fig. 5.2b, we show the geoid that arises from the two contributions

described in section 5. Dashed-dotted line indicates the contribution due to the internal anomaly (eq. 5.73), while the dashed line indicates the contribution due to the boundary deformation (eq. 5.74), which is clearly consistent with the flow pattern of panel a. The solid line, which is obtained via ENS solution and is compared to the SFE solution (represented by squares), is the sum of these two contributions (eq. 5.75). Fig. 5.2c shows a radial cross section of the radial (red) and tangential (blue) components of the flow, for an angle of observation $\vartheta = 5°$. Fig. 5.2d illustrates an angular cross section of the same quantities for the radius $r_1 = 0.2$ m, i.e. inside the inner sphere $\mathcal{S}_2$. The bottom left and bottom right panels show, respectively, for the same values of ϑ and r_1, the radial and angular cross sections of pressure p, which exhibits its largest amplitude within the inner sphere due to the high viscosity of the latter. In all cases, the agreement between the curves is seen to be very good. Since the 1-D model is radially symmetric, the spherical harmonic modes are not coupled. Therefore, for the degree-2 load considered, the cut-off degree chosen for the infinite series of the ENS solution and for the expansions of the SFE solution are $j_{\max}^{\mathrm{ENS}} = j_{\max}^{\mathrm{SFE}} = 2$. The number of radial finite elements N_{FE} used to plot SFE solutions of Fig. 5.2 is 100.

In the subsequent examples, the inner sphere is shifted along the z-axis to create the eccentric configuration. In Table 5.1, we list the values of $j_{\max}^{\mathrm{ENS}}$, $j_{\max}^{\mathrm{SFE}}$ and N_{FE} that we have employed. In the 2-D1 model, shown in Fig. 5.3, $\mathcal{S}_2$ is shifted by 0.5 m with respect to the center of $\mathcal{S}_1$ with a viscosity contrast again of 50. In Fig. 5.3a it is interesting to note that, since the load is directed like $\boldsymbol{e}_{r_2}$ (eq. 5.47), the flow has the tendency to move towards the center of force $\mathcal{O}_2$ or away from it. It is then clear that the force has a tangential component in the coordinate system $\mathcal{O}_1$. The following panels of Fig. 5.3 show the comparison between the ENS and SFE solutions for geoid (panel b), flow (panels c and d) and pressure (panels e and f). Radial cross sections are plotted at the angle $\vartheta = 5°$, while the angular cross section at the radius $r_1 = 0.6$ m. For this configuration, the agreement between the semi-analytical ENS solution and numerical SFE solution is as good as in the 1-D model. This statement remains true also for the model 2-D2 (Fig. 5.4) where the viscosity contrast between the spheres is now 200 (i.e. $\eta_2 = 200$ Pa s). Only a larger number of finite elements for the numerical solution is necessary to achieve a good agreement.

The last model 2-D3 (Fig. 5.5) represents a somewhat extreme case when compared to the previous models. The inner sphere is smaller ($R_2 = 0.2$ m) and its viscosity higher ($\eta_2 = 2000$ Pa s). Again, radial cross sections are plotted at the angle $\vartheta = 5°$, while the angular cross section at the radius $r_1 = 0.6$ m. The two solutions still match very well.

At the end of Section 5.4 we briefly mentioned the possibility of treating no-slip boundary conditions instead of free-slip. For model 2-D3, we show in Fig. 5.6 the differences between the two cases for spheroidal flow and pressure. For all these quantities the differences between the two boundary conditions are minor. The most evident qualitative discrepancy is seen in the tangential flow which is forced to vanish at the surface in the no-slip case, while it is unconstrained in the free-slip case. Differences in the pressure field are negligible.

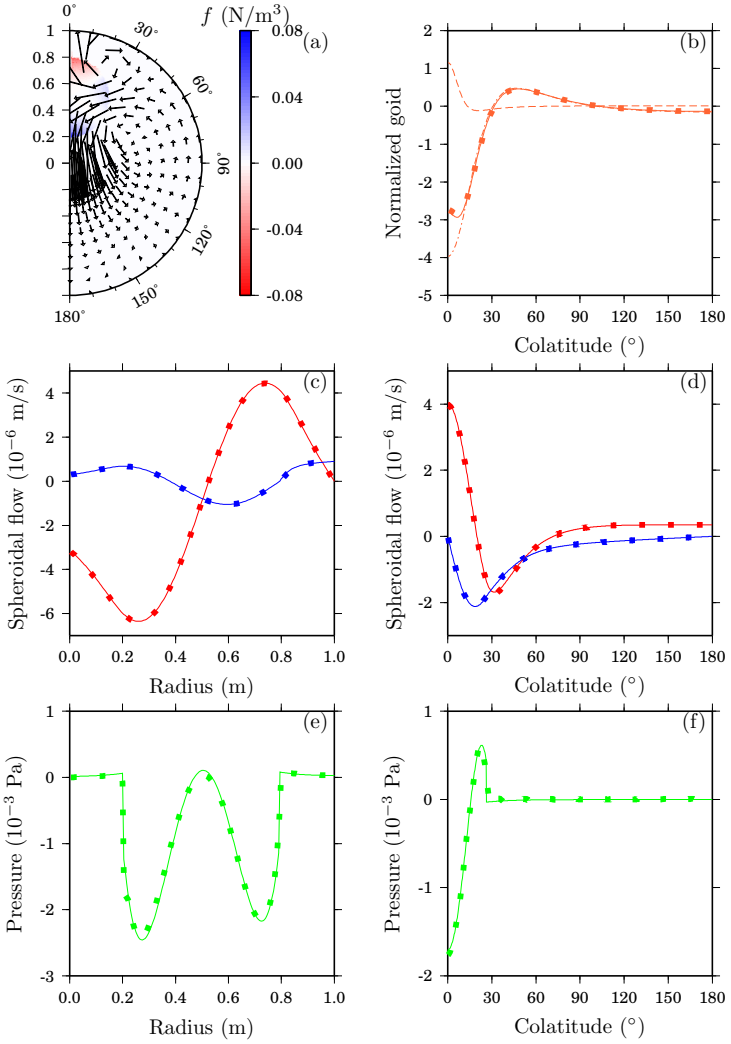

Figure 5.3: As in Fig. 5.2 but for 2-D1 model.

Finally, for the specific radial and angular cross sections plotted in the previous figures, we show in Fig. 5.7, how a refinement of the radial finite-element mesh and a higher angular cut-off degree $j_{\max}^{\mathrm{SFE}}$ can improve the SFE solution, thereby reducing the Root Mean Square (RMS) error with respect to the ENS solution. We define the RMS error difference as follows:

$$\varepsilon_{\mathrm{RMS}} = \sqrt{\frac{1}{N}\sum_{i=1}^{N}\left(Q_i^{\mathrm{ENS}} - Q_i^{\mathrm{SFE}}\right)^2}, \tag{5.76}$$

where Q_i are the field quantities (radial flow, tangential flow or pressure) com-

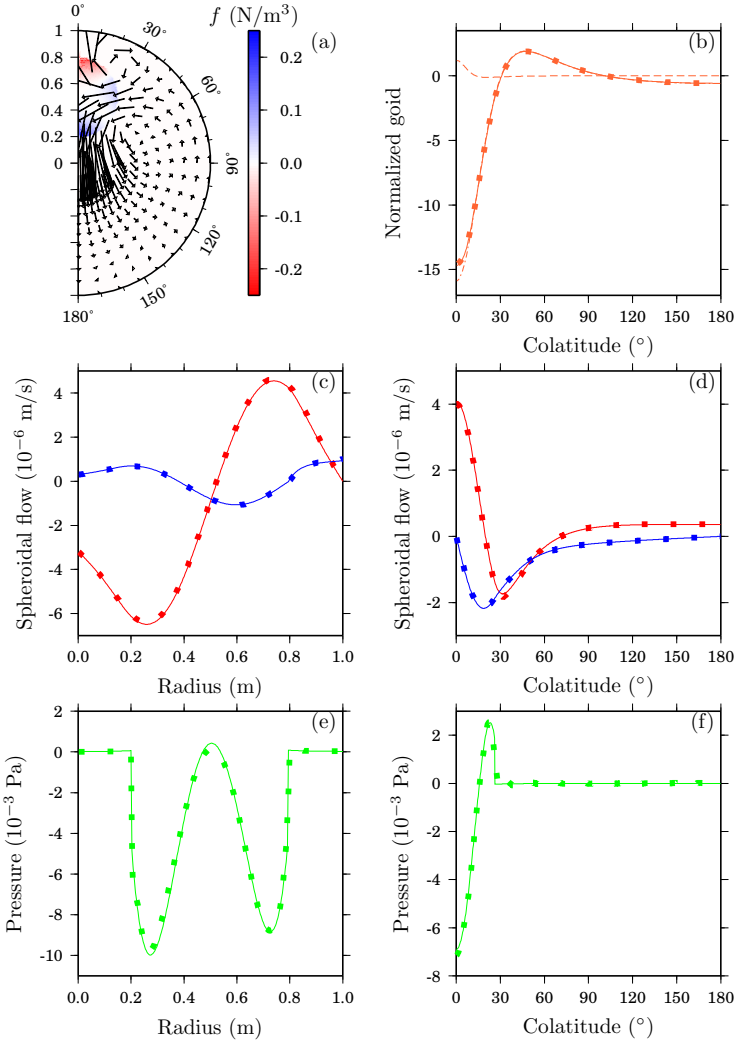

Figure 5.4: As in Fig. 5.2 but for 2-D2 model.

puted either via the ENS or SFE method and N is the number of points at which such quantities are compared. We consider in Fig. 5.7 the three axisymmetric models 2-D1, 2-D2 and 2-D3. In the left column, for the radial cross sections, we show $\varepsilon_{\mathrm{RMS}}$ as a function of the number of finite elements ($N = N_{\mathrm{FE}}$) for radial flow (panel a), tangential flow (panel c) and pressure (panel e). The increase of N_{FE} from 50 to 500 evidently shows the reduction of $\varepsilon_{\mathrm{RMS}}$ for all three variables. Because of the different functional space chosen to discretize the pressure (see Chapter 3), it is not surprising that this variable exhibits an error larger than that found for the flow. Solid, dashed and dashed-dotted lines indicate 2-D1, 2-

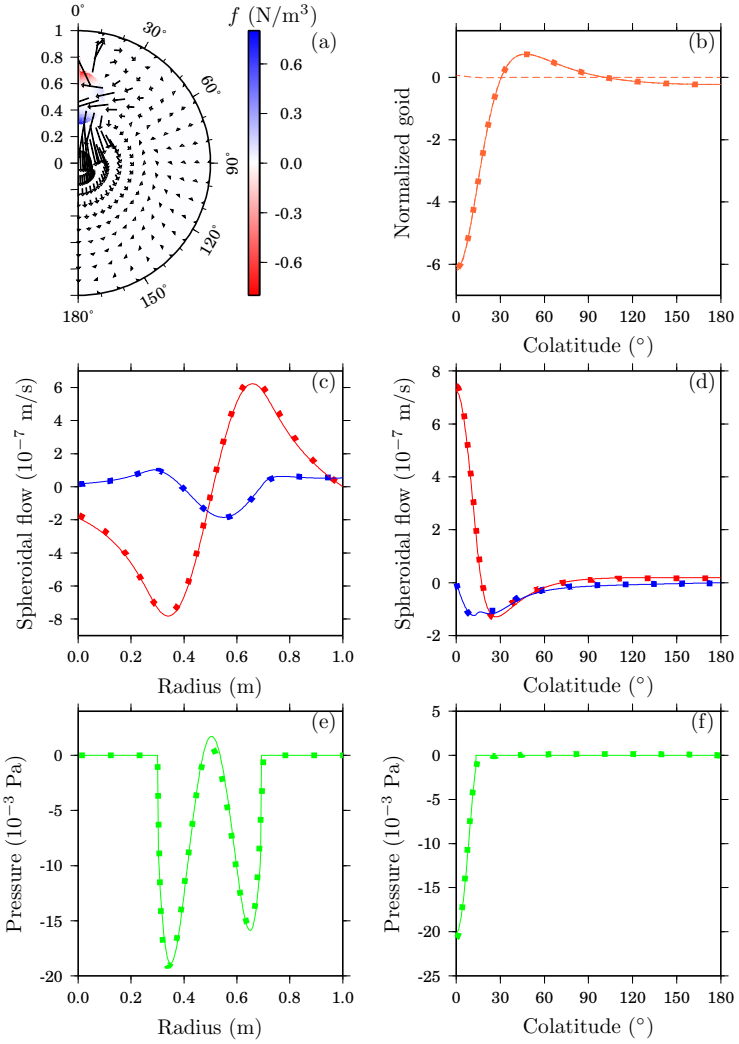

Figure 5.5: As in Fig. 5.2 but for 2-D3 model.

D2 and 2-D3 models, respectively. As expected, the error increases according to the complexity of the model considered. Similar consideration are valid for the error reduction shown in the right column, where we plot, for the angular cross sections, $\varepsilon_{\mathrm{RMS}}$ as a function of $j_{\max}^{\mathrm{SFE}}$. To perform numerically the angular integrations needed by the SFE solution, we employ the Gauss-Legendre quadrature formula (Stoer & Bulirsch, 2002). Therefore, in panels b, d and f of Fig. 5.7, N is the number of Gauss-Legendre points employed to perform such integrations. For all examples, we used $N = 720$. From $j_{\max}^{\mathrm{SFE}} = 20$, the error for radial and tangential flow improves very slightly, while the solution for pressure still seems

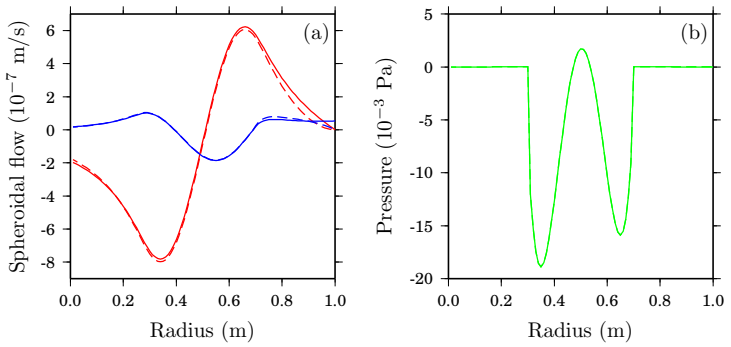

Figure 5.6: Differences between free-slip (solid lines) and no-slip (dashed lines) boundary conditions for spheroidal flow (a) and pressure (b).

to benefit from a higher cut-off degree.

5.7 Final remarks

An obvious application of the procedures described above consists in using the ENS solution for validating numerical codes that solve the Stokes problem in order to constrain mantle flow through the use of geophysical data. Nevertheless, more general convection codes, such as CitCom (e.g., Zhong et al., 2000), designed to model the time evolution of the mantle, may also benefit from the ENS solution, that could be employed to check the 'flow-part' of the solver in the presence of lateral viscosity variations.

The ENS solution has been derived in spherical geometry. Since mantle convection takes place in a spherical shell and not in a full sphere, it would have been more appropriate to derive the semi-analytical solution for a shell with a heterogeneous spherical inclusion. For this case, the BVP (5.1)-(5.5) must be supplemented by two additional boundary conditions that account for the zero radial flow and the free-slip condition that must be imposed at the core-mantle boundary. However, no matter what reference system is chosen (i.e. $\mathcal{O}_1$ or $\mathcal{O}_2$), this would lead to the situation of solving, for each degree j, an overdetermined problem consisting still of the six unknowns $A_{i,j}$ $(i = 1, \ldots, 6)$, but subject now to eight boundary conditions. This problem could be partly overcome by keeping the spherical geometry and including a liquid core with a viscosity much lower than that of the surrounding mantle. Yet in this way, while at the liquid-solid interface of the core-mantle boundary, the free-slip condition would be automatically adjusted, the continuity of the flow field would make it not feasible to satisfy the condition of zero radial flow.

Although the geometry treated here is different from that usually employed in mantle convection calculations, the ENS solution can be still considered a useful benchmark tool. To adapt the SFE code (originally designed to solve the Stokes problem in a spherical shell) to the full spherical geometry required a straightforward modification that involved solely the removal of one boundary

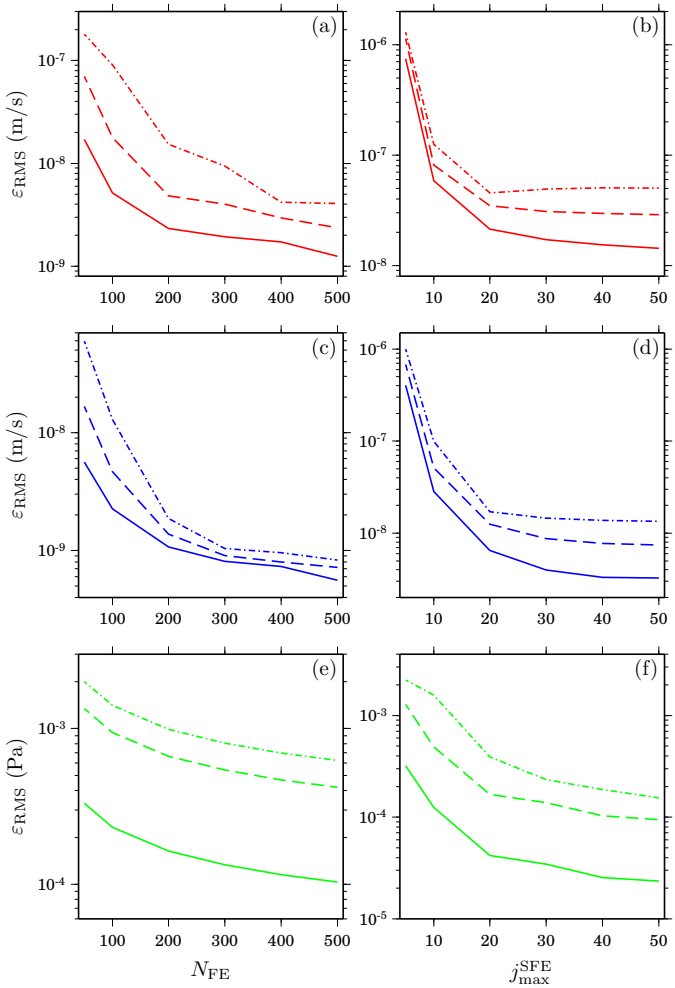

Figure 5.7: RMS error reduction for radial (panels a, c and e) and angular (panels b, d and f) cross sections for radial flow (red), tangential flow (blue) and pressure (green). Solid, dashed and dashed-dotted lines indicate 2-D1, 2-D2 and 2-D3 models respectively.

integral, and this should be the case especially for all those codes based on integral formulations. Nonetheless, the ENS solution can be generalized to treat the case of two 'off-axis' eccentrically nested spheres, thereby providing a semi-analytical solution suited to test fully 3-D Stokes solvers.

CHAPTER 6

Long-wavelength geoid and gravity over subduction zones

Using the SFE approach, we perform numerical experiments to investigate in a spherical axisymmetric geometry the effects of LVV on the low-degree geoid and gravity anomalies above a typical subduction zone. We present a systematic exploration of the parameters space, testing several combinations of density, viscosity and the geometry of a subducted slab having a realistic lateral extent ($\sim$ 100 km), with the aim of predicting the characteristic broad positive highs that the low-degree geoid and gravity exhibit over major subduction zones.

6.1 Observations and models

In Chapter 4, we showed that, at the global scale, the long-wavelength geoid can be successfully modeled in terms of a viscous flow, with radially symmetric viscosity, induced by density perturbations derived from seismic tomography. Such perturbations can be either positive, when associated with cold downwellings, or negative, if they are expression of hot upwellings. However, if instead of seismic tomography, we had employed a geodynamic tomography (see Section 1.3) that uses the present-day location of subductions as a unique source for the internal loading, the fit to the geoid would have been approximately as satisfactory (Ricard et al., 1993). In fact, according to the theory (Schubert et al., 2001), the flow in a continuum mostly heated from within, as is the Earth's mantle, is largely driven by the negative buoyancy of the cold upper boundary layer, i.e. the subducted lithosphere. The mantle heat budget can be ascribed only for 10% to the positive buoyancy of hot upwellings (Sleep, 1990). Therefore, in first approximation they can be ignored. It is then not surprising that a flow model that uses the anomalous density associated solely with subductions is able to explain a large portion of the geoid. Understanding how the geoid is influenced by the characteristic features of a typical subduction, like its geometry, density and viscosity, appears then to be of great importance.

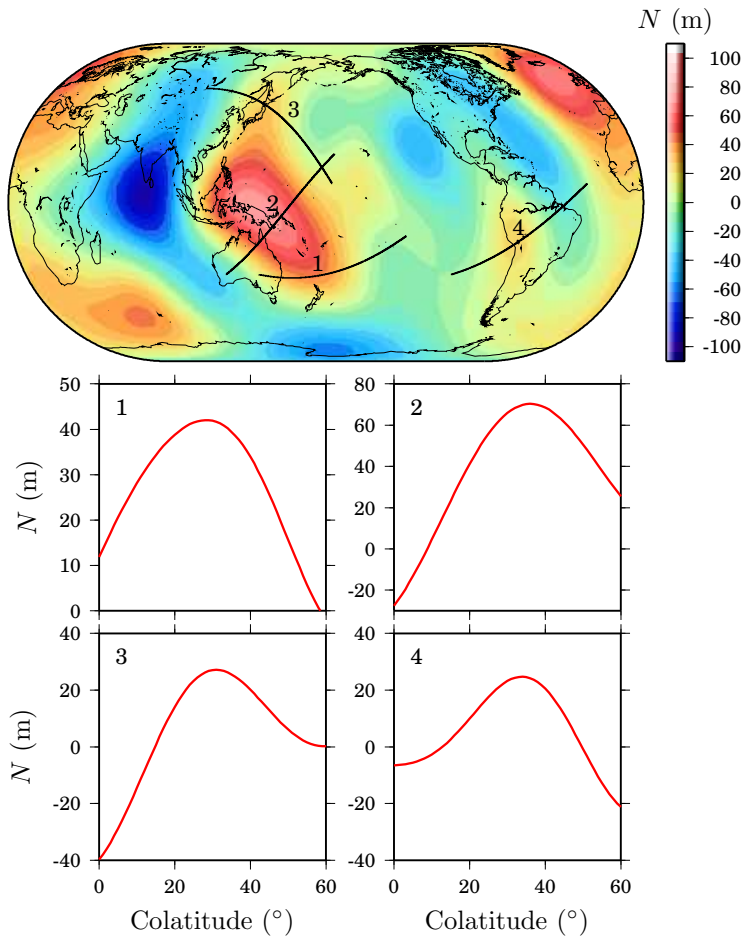

Figure 6.1: Cross sections of long-wavelength ($2 \leq j \leq 8$) GRACE-geoid anomaly Förste et al. (2006).

As we already pointed out in Chapter 1, geoid and gravity anomalies exhibit local maxima above major subduction zones. Figures 6.1 and 6.2 show cross sections of the long-wavelength ($2 \leq j \leq 8$) geoid and gravity field that are roughly perpendicular to four different convergent plate margins. Broad geoid maxima up to 60 degrees wide range from slightly more than 20 m over the subduction zones of South America and Japan up to 40 and 60 m over the Tonga and New Guinea regions, respectively, while the amplitude of the highs in the gravity signal is confined to the interval 15-20 mgal.

The problem of determining geoid highs over subducted slabs in terms of dynamic flow calculations has been extensively studied. From results obtained using incompressible flow models (e.g. Hager, 1984; King & Hager, 1994) as well

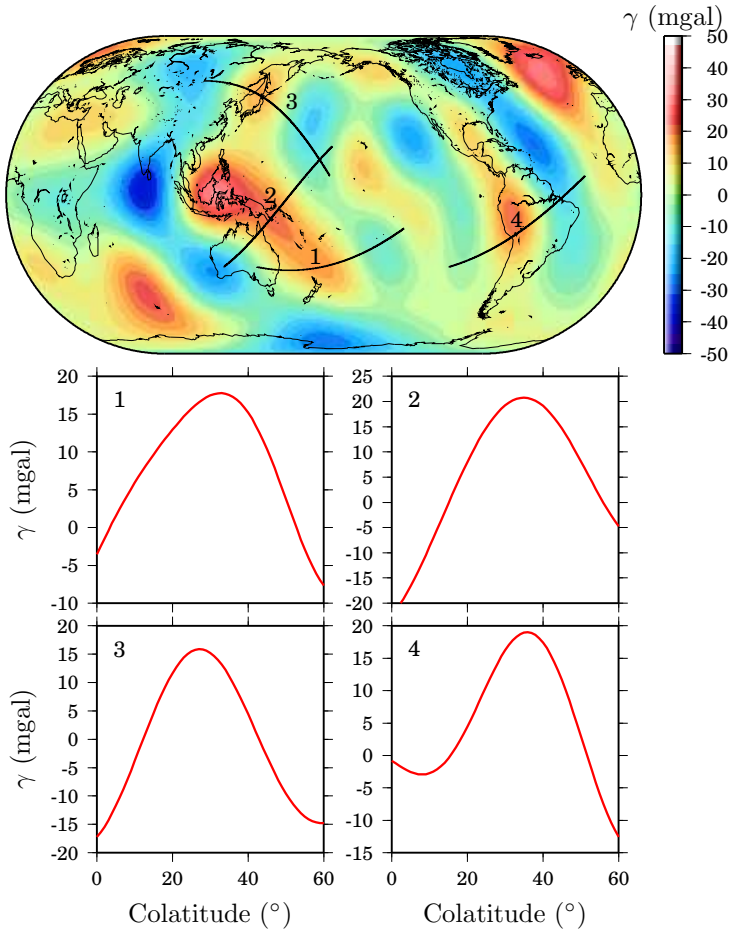

Figure 6.2: Cross sections of long-wavelength ($2 \leq j \leq 8$) GRACE-gravity anomaly Förste et al. (2006).

as those from more complex compressible models incorporating multiple phase transitions (King, 2002), there is general agreement that a viscosity increase from the upper to lower mantle ranging between a factor of 10 to 100 is required to obtain a good fit to the subduction geoid. Within the framework of the ongoing discussion concerning the role played by LVV, it is recognized that, at the global scale, LVV of long wavelengths ($j_{\max} \simeq 20$) such as those that can be inferred from seismic tomography, do not significantly affect inversions of the lowest part of the geoid spectrum ($j = 2, 3$), but can cause more significant contamination of degree 4 and above (Richards & Hager, 1989; Zhang & Christensen, 1993). Differently, regional models of subductions generally fail to predict the correct high-degree signal of the gravity field or of the dynamic topography if LVV of

sufficiently short-wavelength are not taken into account (Moresi & Gurnis, 1996; Billen & Gurnis, 2003). Our purpose here is to investigate to what extent the low-degree geoid and gravity field due to a slab with realistic spatial resolution, density and viscosity are influenced by LVV.

The resolution of both seismic and geodynamic tomography models is generally relatively low. On the one hand, seismic tomography manifest rather blurry fast regions that correlate well with the expected distribution of slabs, but do not form continuous and sharply defined channels from the lithosphere inside the mantle. On the other hand, the geodynamic model of Ricard et al. (1993) for instance, provides slab densities in spherical harmonics up to degree and order 15, corresponding to a spatial resolution of approximately 2500 km, definitely too coarse for an accurate description of a typical subducted lithosphere that has a thickness of 100 km. To overcome this lack of resolution, Zhong & Davies (1999) (the only study to our knowledge where density and LVV at a high resolution are considered when modeling the long-wavelength geoid) replaced in the upper mantle the model of Ricard et al. (1993) with better defined slabs assumed to have a thickness of 400 km and kept the original lower mantle model, consistent with the hypothesis that the presumed increase in the lower mantle viscosity is responsible for a significant thickening of the slab. However, in our study we aim at modeling a subduction zone having a realistic spatial extent. Thus, as described in detail in the following section, the slab buoyancy and viscosity structure will be constructed explicitely.

6.2 Model setting

To study the geoid associated with a typical subducted slab, we use a spherical axisymmetric mantle model. The simplification of employing such a geometry allows us to model the geoid at a global scale, including lateral variations in viscosity and density at high resolution. At the same time, we can explore the parameter space by assessing several different viscosity and density models, which in a fully three-dimensional geometry would require computational times that are definitely too long for the sequential machine on which our models have been ran.

We consider a simple mantle model consisting of three viscosity layers: lithosphere (η_{lith}) extending from the Earth's surface to 100 km depth, an upper mantle (η_{um}) from the base of the lithosphere to 670 km depth and a lower mantle (η_{lm}) from the base of the upper mantle to the core-mantle boundary. As the geoid is sensitive to relative viscosity contrasts only, in all models we keep the viscosity of the upper mantle fixed at the reference value of $\eta_{\mathrm{um}} = 10^{20}$ Pa s. At colatitude $\vartheta = 80°$, we locate the trench where a oceanic plate subducts at a constant dip angle of 50°. The thickness of the subducting plate is 100 km everywhere. In those models that include LVV, the trench is marked by a weak narrow region (approximately half-degree wide) of low viscosity, (η_{wz}), whose value is three order of magnitude lower than that of the surrounding lithosphere to ensure decoupling between the oceanic and continental plate. Furthermore,

in all models with LVV, the viscosity of the subducting plate ($\eta_{\rm slab}$) equals that of the lithosphere at every depth. As a consequence, in those models for which $\eta_{\rm lith} = \eta_{\rm lm}$, the lower mantle does not contain LVV. Table 6.1 summarizes the combinations of viscosity that have been investigated. Figure 6.3 shows as an example the 2D axisymmetric viscosity structure of model C2. For each 2D model listed in Table 6.1, we also perform a numerical experiment with a corresponding radially symmetric viscosity model by simply considering lithosphere, upper and lower mantle as laterally homogeneous.

Viscosity model	$\eta_{\rm lith/slab}$ (Pa s)	$\eta_{\rm lm}$ (Pa s)	$\rm LVV_{lm}$
A1	$5 \cdot 10^{20}$	$5 \cdot 10^{20}$	N
A2	10^{21}	$5 \cdot 10^{20}$	Y
A3	$5 \cdot 10^{21}$	$5 \cdot 10^{20}$	Y
A4	10^{22}	$5 \cdot 10^{20}$	Y
A5	$5 \cdot 10^{22}$	$5 \cdot 10^{20}$	Y
A6	10^{23}	$5 \cdot 10^{20}$	Y
B1	10^{21}	10^{21}	N
B2	$5 \cdot 10^{21}$	10^{21}	Y
B3	10^{22}	10^{21}	Y
B4	$5 \cdot 10^{22}$	10^{21}	Y
B5	10^{23}	10^{21}	Y
C1	$5 \cdot 10^{21}$	$5 \cdot 10^{21}$	N
C2	10^{22}	$5 \cdot 10^{21}$	Y
C3	$5 \cdot 10^{22}$	$5 \cdot 10^{21}$	Y
C4	10^{23}	$5 \cdot 10^{21}$	Y
D1	10^{22}	10^{22}	N
D2	$5 \cdot 10^{22}$	10^{22}	Y
D3	10^{23}	10^{22}	Y
E1	$5 \cdot 10^{22}$	$5 \cdot 10^{22}$	N
E2	10^{23}	$5 \cdot 10^{22}$	Y
F1	10^{23}	10^{23}	N

Table 6.1: Viscosity models tested in our study. The viscosity of the upper mantle is fixed ($\eta_{\rm um} = 10^{20}$). The slab and lithosphere have the same viscosity in all models. The fourth column indicate whether LVV in the lower mantle are present or not.

From Fig. 6.3, it is evident that lateral variations in viscosity are not sharp. Since colatitude ϑ is parameterized with spherical harmonics, as in all spectrally based parameterizations, Gibbs oscillations (e.g. Walker, 1988) are likely to appear in proximity of sharp discontinuities of viscosity and cannot be completely suppressed. This effect, that could induce unrealistic oscillations in the solution, can be eliminated by suitably smoothing sharp changes in viscosity. As example, Fig. 6.4 shows the reconstruction, through analysis and synthesis of Legendre

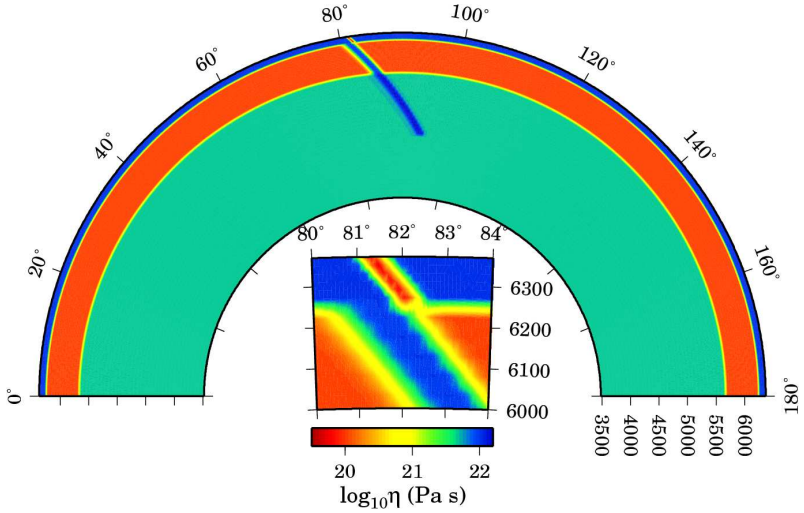

Figure 6.3: Typical viscosity structure. Here, viscosity model C2 (see Table 6.1) is shown for a slab extending to the middle lower mantle (density model 'd') along with a zoom on the trench region where a low viscosity zone is used to decouple the plates.

polynomials, of the step function (Fig. 6.4a)

$$s(\vartheta) = \begin{cases} 1 & \text{if } 0 \leq \vartheta \leq 90 \\ 0 & \text{if } 90 \leq \vartheta \leq 180. \end{cases} \tag{6.1}$$

The same procedure of analysis followed by the synthesis of Legendre polynomials is applied to the step function $s_B(\vartheta)$ smoothed with a *Butterworth filter* (Fig. 6.4b) as follows:

$$s_B(\vartheta) = \frac{1}{\sqrt{1 + \left(\frac{\vartheta}{90}\right)^{2n}}},$$

where n is an integer denoting the order of the filter; the higher is n, the closer $s_B(\vartheta)$ is to $s(\vartheta)$. It is evident that the filtering causes a dramatic reduction of the oscillations that appear on both sides of the discontinuity in the first case.

Finally, the internal load is prescribed in terms of a density anomaly (or excess mass) that occupies the slab region and extends from the base of the lithosphere into the mantle. For each viscosity model, four different density configurations are tested (see Table 6.2 and Fig. 6.5). In models 'a' an anomaly of 60 kg/m^3 extends until the base of the upper mantle, simulating a slab that does not penetrate the transition zone at 660 km depths. Models 'b' simulate a slab with the same excess mass that does penetrate the transition zone and extends until the middle lower mantle at a depth of 1750 km. In models 'c', a

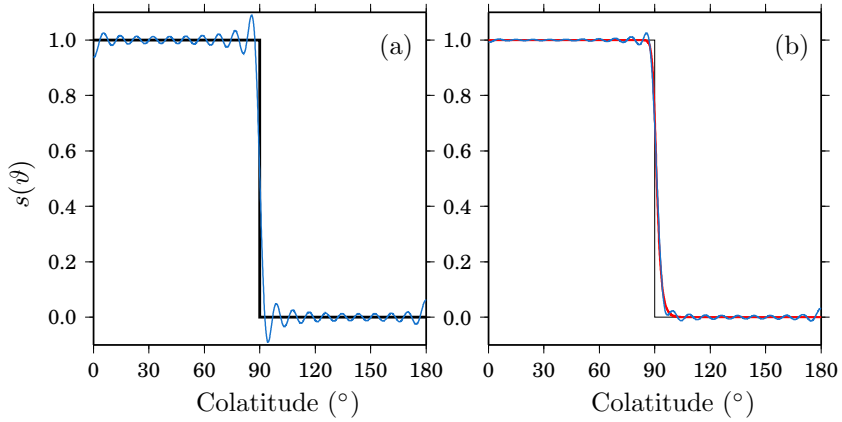

Figure 6.4: Method for smoothing sharp lateral discontinuities in viscosity. a) By analyzing the step function (black line) $s(\vartheta)$ in Legendre polynomials and performing the synthesis (blue line), Gibbs oscillations appear at the discontinuity $\vartheta = 90$. b) Analyzing the step function $s_B(\vartheta)$ smoothed with Butterworth filter (6.1) (red line) and performing its synthesis (blue line) dramatically damps Gibbs oscillations.

slab with the same density as the previous two series of models extends through the whole mantle depth until the base of the lower mantle. Finally, in models 'd' the effect of slab-thickening is considered by imposing a density in the lower mantle three-times higher than that of the slab in the upper mantle.

Density model	$\delta\rho_{0\to670}$ (kg/m^3)	$\delta\rho_{670\to\mathrm{CMB}}$ (kg/m^3)	$\delta\rho_{0\to1750}$ (kg/m^3)
a	60	0	/
b	/	/	60
c	60	60	/
d	60	180	/

Table 6.2: Density models. For each viscosity model of Table 6.1, four different density models are considered according to the slab's extent in depth or to the value of the density anomaly.

6.3 Model calculations and discussion

Using the models listed in Table 6.1, we use the SFE method to analyze 21 mantle models having axisymmetric viscosity and as many having a corresponding radially symmetric viscosity distribution. For each 42 models, we consider four different combinations of internal loading according to Table 6.2, which leads to a total of 168 tested models.

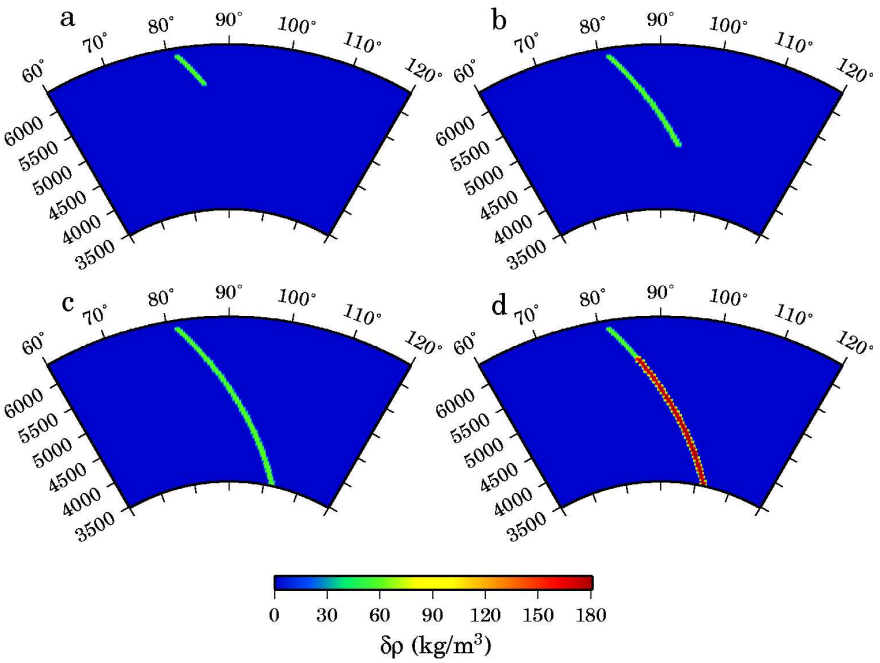

Figure 6.5: The four density configurations tested in our numerical experiments. Slab density amount to 60 kg/m^3 everywhere for models 'a', 'b' and 'c'. In density model 'd' a strong increase of the density in the lower mantle (180 kg/m^3) is considered.

In the following, we will focus our attention on the long-wavelength part of the geoid and gravity spectra by considering the mantle's response to subduction in the harmonic range $2 \leq j \leq 8$. In spite of this, the resolution of the numerical model needs to be quite high. In fact, in order to properly resolve the density and viscosity structures of a 100 km-thick subducted lithosphere, we compute the solution of the Stokes problem up to harmonic degree $j = 700$, corresponding to a spatial wavelength of approximately 60 km. Moreover, a non-uniform finite element grid is employed to discretize the radial coordinate. The spacing of the radial grid elements is 55 km in the lower mantle, 50 km in the upper mantle and 20 km in the lithosphere.

The main goal of our analysis is to investigate which mantle models are able to reproduce broad positive geoid and gravity anomalies above the subducting plate. Let us start by considering viscosity models A and B. They are characterized by a moderate increase in the viscosity of the lower mantle with respect to that of the upper mantle: half order and one order of magnitude, respectively. In Chapter 4 we showed that the best fit to the geoid in terms of a 1D viscosity distribution is obtained when the lower mantle is 40 times more viscous than the upper mantle. Furthermore, as we mentioned above, an increase of at least one order of magnitude, but more likely higher, also represents one of the main re-

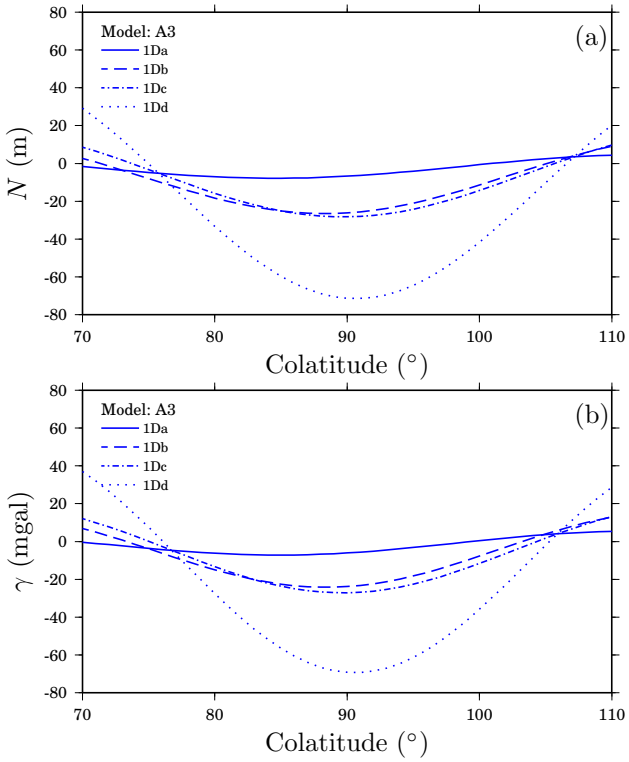

Figure 6.6: Geoid (a) and gravity anomaly (b) for 1D viscosity model A3. Density models 'a', 'b', 'c' and 'd' are specified according to the line style indicated in the legend.

sults from other studies. Thus, it is not surprising that the increase in the lower mantle viscosity that characterizes models A and B is not sufficient to ensure a satisfactory subduction geoid. As representative of viscosity models A and B, we show in Figs 6.6 and 6.7 the geoid and gravity anomalies obtained with 1D models A3 and B2 only, that are characterized by the same value of $\eta_{\rm lith}$. For the moment, LVV are not considered, since their effect will be discussed next for those models that ensure geoid and gravity highs. From these figures it is evident that, no matter what anomalous density is used, these models always result in clear negative peaks of geoid and gravity over the trench region ($\vartheta \simeq 90$). The increase of the depth to which the density anomaly extends within the mantle, and hence of the strength of the internal buoyancy, only produces a more pronounced negative signal. It is worth noting that for density models 'a', for which the slab is confined in the upper mantle, both geoid and gravity have extremely small (nearly vanishing) amplitude compared to the other three density models. Independent of the viscosity of the lithosphere, all remaining viscosity models A and B (cfr. Fig. 6.11) manifest a qualitatively similar behavior to that shown

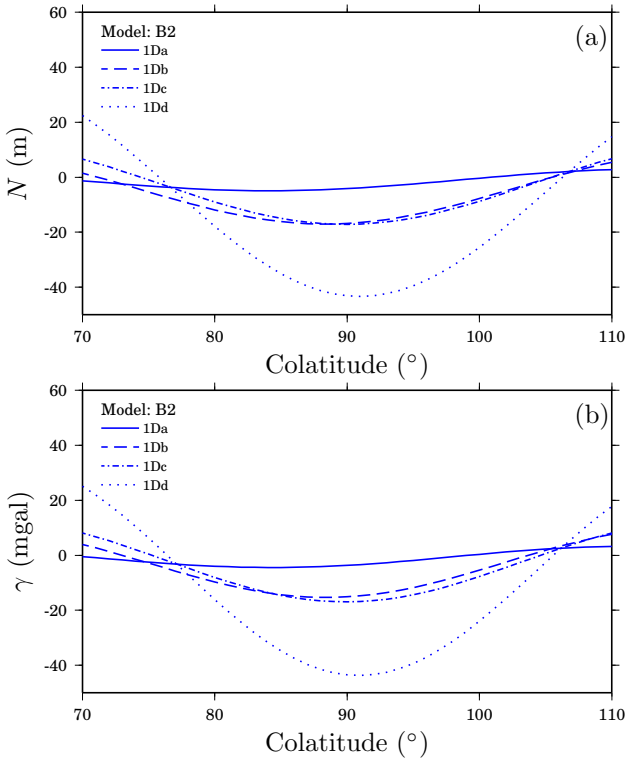

Figure 6.7: As in Fig. 6.6 but for viscosity model B2.

in Figs 6.6 and 6.7, confirming that the viscosity ratio $\eta_{\rm lm}/\eta_{\rm um}$ is responsible for the first-order effects on the geoid and gravity due to a subduction, and is crucial to obtain the correct sign for geoid and gravity anomalies. This is also evident if we compare models A3 and B2. The increase of half order of magnitude in the lower mantle viscosity that characterizes the latter reduces the geoid and gravity lows of approximately 30 m and 30 mgal, respectively, suggesting again that increasing the lower mantle viscosity is the correct way to match the observed amplitudes.

More relevant for our discussion are the subsequent viscosity models C to F, since they all induce positive signals. Let us consider for example models C2 and D1, shown in Figs 6.8 and 6.9, respectively, where both results from 1D and 2D viscosity distributions are plotted. For these two configurations, all four combinations of density give geoid and gravity highs over the trench region. In both cases however, density models 'a' present relatively small amplitudes (less than 15 m and 15 mgal for geoid and gravity, respectively) that do not show up in Figs 6.1 and 6.2. As it will be shown in the following, such behavior is a common feature of all viscosity models C to F. This suggests that the anomalous mass of a slab confined in the upper mantle is not sufficient to explain the

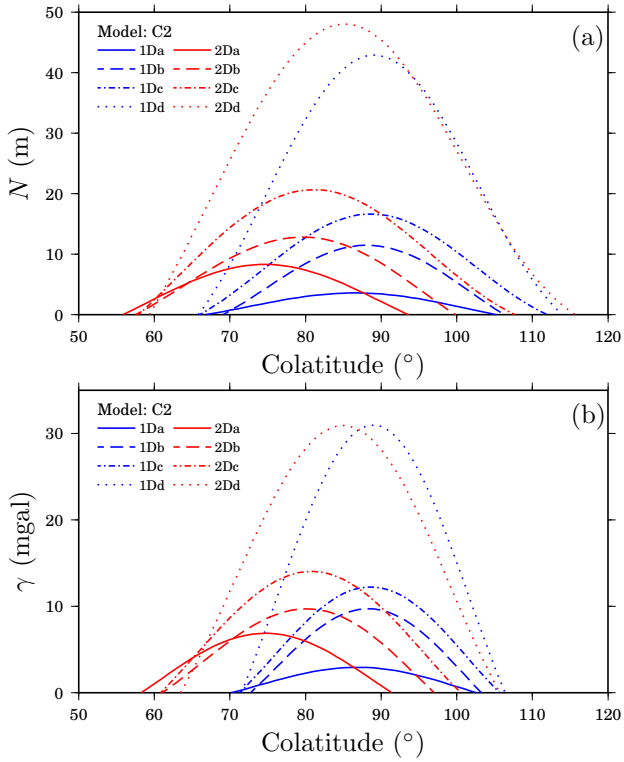

Figure 6.8: As in Fig. 6.6 but for viscosity model C2. Blue and red lines refer here to 1D and 2D viscosity, respectively.

characteristic amplitudes of geoid and gravity generally observed above major subduction zones, unless the slab is assigned an unrealistically high buoyancy in the upper mantle or a large mass anomaly is attributed to a portion of the slab that stagnates at the phase transition. On the other hand, with the exception of the geoid of models C1 and C2, all 'd' density models induce amplitudes that are generally too large with respect to the observations. A strong increase in the slab excess mass in the lower mantle, such as that proposed in the geodynamic tomography of Ricard et al. (1993) ascribed to the increased ambient viscosity of the lower mantle, seems then also not to be compatible with the typical low-degree amplitudes of geoid and gravity.

As far as the density is concerned, the most interesting features are offered by models 'b' and 'd', being the amplitudes of the gravity field they both induce in good qualitative agreement with the observations. The differences among them are moderate, even though the slab geometry is remarkably different in the two cases: slabs of models 'b' reach only a depth of 1750 km, while slabs of models 'c' reach the CMB and are characterized by an excess mass approximately 60 % higher than models 'b'. Therefore, even though our models are by no means

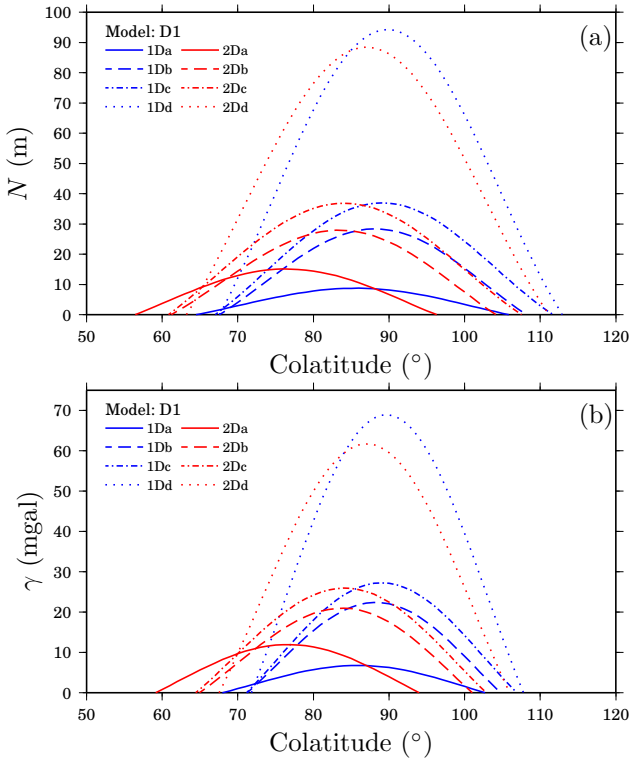

Figure 6.9: As in Fig. 6.8 but for viscosity model D1.

able to furnish indications about the depth that a slab should reach to ensure a good signal in the long-wavelength gravity field, they strongly suggest the need for the presence of well defined density anomalies in the lower mantle. It seems then to be necessary that at least a portion of the slab penetrates the 660 km discontinuity.

Another important result emerging from our calculations concerns the role played by LVV. In Figs 6.8 and 6.9, blue and red lines indicate geoid and gravity profiles obtained with radially dependent viscosity models and models containing LVV, respectively. The largest differences between 1D and 2D viscosity distributions arise in those models for which the slab is confined in the upper mantle (i.e. models 'a'). In fact, both in model C2a and model D1a, the use of LVV in the slab region approximately doubles the moderate highs that appear over the subduction zone when a 1D viscosity model is employed. However, this is not the case for the other density models. When models 'b', 'c' or 'd' are used, the differences in amplitudes of the geoid or gravity anomalies between 1D and 2D viscosity models are definitely minor, though they tend to increase as the slab is assigned more excess mass. Interestingly, the most evident effect caused by the introduction of LVV into the models is to systematically shift the geoid and

gravity profiles towards the trench region in an inversely proportional manner to the slab degree of buoyancy. On the one hand, profiles arising from 1D viscosity models all exhibit their maxima approximately at 90° colatitude, i.e. 10° away of the trench. However, for 2D viscosity models, the high viscosity assigned to the slab is able to better focus the internal loading, with profiles obtained taking LVV into account having maxima directly above the trench for 'a' models and progressively away from it for models 'b', 'c' and 'd'. This is further confirmed if we compare the typical flow pattern associated with the 1D and 2D versions of a model. In Fig. 6.10a and 6.10b, we show the flow resulting from the 1D and 2D distributions of viscosity, respectively, for viscosity model C2 and with density 'b'. When the viscosity is radially symmetric, an extremely vigorous flow cell is concentrated in the upper mantle, while in the lower mantle, due to its high viscosity, smaller velocities are observed and the slab sinks nearly vertically. By contrast, the presence of LVV helps to define a clear flow pattern in the whole mantle.

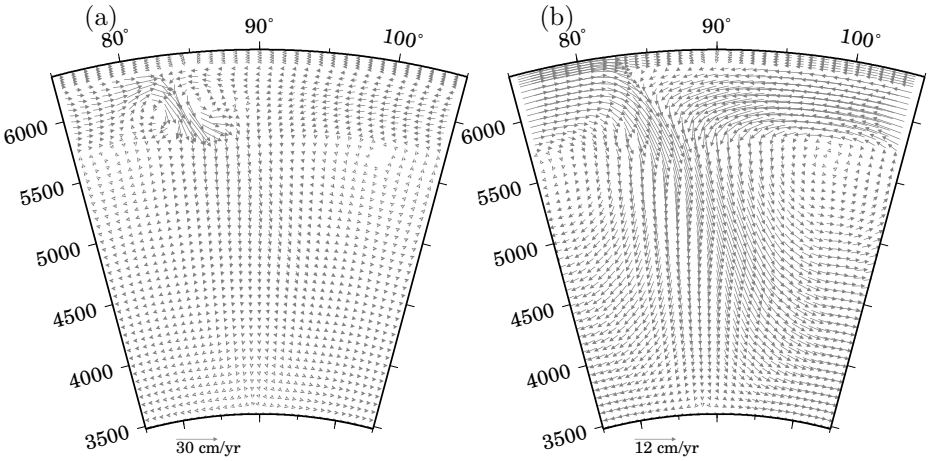

Figure 6.10: Typical flow pattern arising from 1D and 2D viscosity models (panels a and b, respectively). Viscosity model C2d is shown.

So far, we have described only a few examples taken from the numerous experiments that have been performed. Nevertheless, it is not worth listing all of the geoid and gravity profiles obtained, since, as we are going to show, their amplitudes exhibit a very regular behavior as the viscosity of the slab/lithosphere and lower mantle vary. It is then more interesting to summarize all results by plotting the highest amplitudes as a function of the density and viscosity parameters, as shown in Fig. 6.11 for the geoid only (the patterns obtained for the gravity anomalies are very similar and lead to the same conclusions). We only present results from those models that ensure a positive geoid over the subduction zone (viscosity model C to F). Fig. 6.11 shows, for the four density

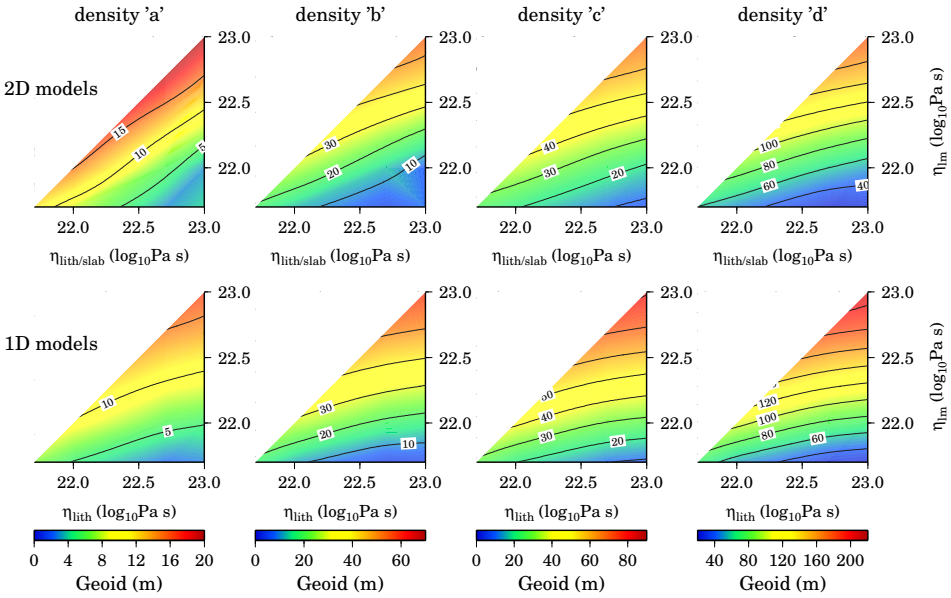

Figure 6.11: Highest geoid amplitude as a function of slab/lithosphere and lower mantle viscosity for models that produce a positive signal over the subduction zone.

models analyzed, the maximum geoid amplitude as a function of the viscosity of the lower mantle and the viscosity of the slab/lithosphere, for 2D models, or simply of the lithosphere in the case of 1D models. As we pointed out above, models 'a' always present relatively small amplitudes compared to that observed over major subduction zones (20-60 m) in the harmonic range $2 \leq j \leq 8$. For all other density models for which the slab penetrates the lower mantle, several viscosity models produce geoid highs that are comparable with the observed amplitudes. The differences between results obtained using 1D and 2D viscosity models are clearly minor and seem to indicate that, at least in the lower mantle, the presence of stiff slabs is not necessary when a fit to the long-wavelength slab geoid is sought.

Conclusions

The main goal of this work has been the development of a reliable and efficient numerical model for the solution of the present-day mantle convection problem. We have implemented a solution scheme based on a weak formulation of the coupled Stokes-Poisson problem. Although the finite element method is nowadays a standard tool in geodynamics research, here it was used for the first time in combination with a spectral parameterization based on spherical harmonics to treat viscous flow models in a spherical geometry.

The classical technique based on propagator matrices provides us with an analytical solution of the Stokes-Poisson problem in the presence of laterally homogeneous viscosity distributions. This has been derived and implemented in order to validate the spectral finite element (SFE) method. The SFE and matrix propagator solutions have been compared using Green's functions obtained from simple internal loads and a satisfactory agreement was always achieved. For the solution of problems with a radially dependent viscosity, the SFE approach has proven to be a very efficient tool. The use of spherical harmonics, along with their orthogonality properties, results in a banded sparse system matrix, whose inversion can be performed very quickly for each harmonic degree considered. Moreover, the employment of Lagrange multipliers to adjust the free-slip boundary conditions enables us to readily compute the dynamic surface deformations, and hence the geoid, thereby avoiding the traditional need to retrieve surface stresses from the flow field.

The SFE method is designed to treat lateral viscosity variations (LVV). For such a case however, the matrix propagator technique is no longer applicable. Nevertheless, the evaluation of the coupling of spherical harmonic modes arising because of LVV requires an accurate validation of the numerical solution. The lack of well documented benchmark tests in the presence of LVV motivated us to derive and implement a semi-analytical solution of the Stokes problem for a special configuration consisting of two viscous eccentrically nested spheres (ENS). After careful testing, evidence has been provided that the semi-analytical solution is correct, and that our numerical code is accurate in solving problems with 2D viscosity distributions. The ENS solution has been derived in a spherical axisymmetric geometry. Nonetheless, the possibility of deriving a similar solution in a fully 3D geometry consisting of two off-axis spheres appears to be very promising and should be taken into serious consideration for future devel-

opments. Furthermore, a test example with 3D viscosity would permit us to validate the toroidal part of the flow field that is not excited in 1D and 2D viscosity models. Scientific cooperation has been established with researchers working with different 3D finite element solvers in order to propose the ENS solution as a benchmark test for the community.

An axisymmetric viscosity model has been used to investigate the low-degree geoid signal induced by a typical subduction, with the aim of predicting the characteristic broad highs observed over major subduction zones and estimating the role played by very localized LVV. Several high resolution density and viscosity models have been systematically analyzed. On the one hand, as far as the mantle radial viscosity structure is concerned, our case study has confirmed that the viscosity contrast between upper and lower mantle is responsible for the first order effects on geoid predictions; a lower mantle at least one order of magnitude more viscous than the upper mantle is necessary to ensure a positive geoid signal of realistic amplitude. On the other hand, though LVV cause dramatic changes in the mantle flow field, they are not able to modify significantly the amplitude of the low-degree geoid, suggesting then no need to consider stiff slabs while modeling the long-wavelength geoid.

Unfortunately, although fully 3D viscosity models can be handled with our SFE method, their demands in terms of computational power, along with the lack of adequate hardware, made it not feasible to present here meaningful examples derived from them.

APPENDIX A

Spherical harmonics

This appendix summarizes the definition, normalization and orthogonality relations of scalar, vector and tensor spherical harmonic functions that have been used throughout the text. A few formulae that result from the application of differential operators on scalar and vector spherical harmonics are presented, along with the possible combinations of double-dot products of tensor spherical harmonics necessary to solve the Stokes problem in the presence of LVV. Finally, the transformation theorems for translation of scalar spherical harmonics that have been employed in Chapter 3 for deriving the eccentrically nested spheres solution are recalled.

A.1 Scalar, vector and tensor spherical harmonics

Scalar spherical harmonics

Among several different normalizations that are discussed in the literature, the angular part of scalar functions is expanded into a series of fully normalized complex *scalar spherical harmonic functions* Y_{jm} (Varshalovich et al., 1989):

$$Y_{jm}(\Omega) \equiv \sqrt{\frac{2j+1}{4\pi}\frac{(j-m)!}{(j+m)!}} P_j^m(\cos\vartheta) e^{im\varphi} = P_{jm}(\cos\vartheta) e^{im\varphi}, \tag{A.1}$$

where $P_{jm}(\cos\vartheta)$ are the normalized version of the *associated Legendre polynomials*

$$P_j^m(\cos\vartheta) = (-1)^m (1-\cos^2\vartheta)^{m/2} \frac{d^m}{d(\cos^m\vartheta)} P_j(\cos\vartheta),$$

where $P_j(\cos\vartheta)$ are Legendre polynomials that can be defined by the *Rodriguez formula*:

$$P_j(\cos\vartheta) = \frac{1}{2^j j!} \frac{d^j}{d(\cos^j\vartheta)} (\cos^2\vartheta - 1)^j.$$

Functions Y_{jm} are eigenfunctions of the angular part of Laplace operator:

$$\frac{1}{\sin\vartheta}\frac{\partial}{\partial\vartheta}\left(\sin\frac{\partial Y_{jm}}{\partial\vartheta}\right)+\frac{1}{\sin\vartheta}\frac{\partial^2 Y_{jm}}{\partial\varphi^2}=-j(j+1)Y_{jm} \tag{A.2}$$

and are orthonormal on the unit sphere:

$$\int_\Omega Y_{jm}Y^*_{j'm'}=\delta_{jj'}\delta_{mm'}. \tag{A.3}$$

Complex conjugate spherical harmonics, denoted with an asterisk, are

$$Y^*_{jm}=(-1)^m Y_{j\,-m}.$$

Vector spherical harmonics

Similarly, following for example Phynney & Burridge (1973), vector functions can be expanded into a series of *vector spherical harmonics* $\boldsymbol{S}^{(\ell)}_{jm}$ ($j=0,1,\ldots$, $m=-j,\ldots,j$, $\ell=-1,\,0,\,1$) defined as follows:

$$\boldsymbol{S}^{(-1)}_{jm}(\Omega)\equiv Y_{jm}(\Omega)\boldsymbol{e}_r, \tag{A.4}$$

$$\boldsymbol{S}^{(1)}_{jm}(\Omega)\equiv \operatorname{grad}_\Omega Y_{jm}(\Omega), \tag{A.5}$$

$$\boldsymbol{S}^{(0)}_{jm}(\Omega)\equiv \boldsymbol{L}_\Omega Y_{jm}(\Omega), \tag{A.6}$$

where $\operatorname{grad}_\Omega$ is the angular part of the gradient operator:

$$\operatorname{grad}_\Omega\equiv \boldsymbol{e}_\vartheta\frac{\partial}{\partial\vartheta}+\boldsymbol{e}_\varphi\frac{1}{\sin\vartheta}\frac{\partial}{\partial\varphi}$$

and $\boldsymbol{L}_\Omega$ is the angular part of the angular momentum operator:

$$\boldsymbol{L}_\Omega\equiv\boldsymbol{e}_r\times\operatorname{grad}_\Omega=-\boldsymbol{e}_\vartheta\frac{1}{\sin\vartheta}\frac{\partial}{\partial\varphi}+\boldsymbol{e}_\varphi\frac{\partial}{\partial\vartheta}.$$

Vector spherical harmonics $\boldsymbol{S}^{(\ell)}_{jm}$ with $\ell=\pm1$ are called *spheroidal*, while if $\ell=0$, they are called *toroidal*. Vector spherical harmonics with $\ell=-1$ are orthonormal on the unit sphere, while if $\ell=0,\,1$ they are simply orthogonal:

$$\int_\Omega \boldsymbol{S}^{(-1)}_{jm}\cdot\left(\boldsymbol{S}^{(-1)}_{j'm'}\right)^*\,d\Omega=\delta_{jj'}\delta_{mm'}, \tag{A.7}$$

$$\int_\Omega \boldsymbol{S}^{(1)}_{jm}\cdot\left(\boldsymbol{S}^{(1)}_{j'm'}\right)^*\,d\Omega=j(j+1)\delta_{jj'}\delta_{mm'}, \tag{A.8}$$

$$\int_\Omega \boldsymbol{S}^{(0)}_{jm}\cdot\left(\boldsymbol{S}^{(0)}_{j'm'}\right)^*\,d\Omega=j(j+1)\delta_{jj'}\delta_{mm'}, \tag{A.9}$$

while if $\ell\neq\ell'$, we have

$$\int_\Omega \boldsymbol{S}^{(\ell)}_{jm}\cdot\left(\boldsymbol{S}^{(\ell')}_{j'm'}\right)^*\,d\Omega=0. \tag{A.10}$$

Furthermore, the integration of vector spherical harmonics results in the following identity:

$$\int_\Omega \boldsymbol{S}_{jm}^{(\ell)}\, d\Omega = \sqrt{\frac{4\pi}{3}}\delta_{j1}(\delta_{\ell,-1} + 2\delta_{\ell,1}),$$

where $\boldsymbol{e}_m$, $m = -1\,,0\,,1$, are cyclic covariant base vectors (Varshalovich et al., 1989, Section 1.1). Complex conjugate vector harmonics are:

$$\boldsymbol{S}_{jm}^{(\ell)*} = (-1)^{m+\ell+1}\boldsymbol{S}_{j\,-m}^{(\ell)}.$$

From definitions (A.4)-(A.6), the cross products $\boldsymbol{e}_r \times \boldsymbol{S}_{jm}^{(\ell)}$ can be derived:

$$\boldsymbol{e}_r \times \boldsymbol{S}_{jm}^{(0)} = -\boldsymbol{S}_{jm}^{(-1)}, \tag{A.11}$$

$$\boldsymbol{e}_r \times \boldsymbol{S}_{jm}^{(-1)} = 0, \tag{A.12}$$

$$\boldsymbol{e}_r \times \boldsymbol{S}_{jm}^{(1)} = \boldsymbol{S}_{jm}^{(0)}. \tag{A.13}$$

The gradient of the scalar function $f(r)Y_{jm}(\Omega)$, where f is an arbitrary differentiable function of r, can be expressed in terms of vector spherical harmonics as follows:

$$\text{grad}\,(f\,Y_{jm}) = \frac{df}{dr}\boldsymbol{S}_{jm}^{(-1)} + \frac{f}{r}\boldsymbol{S}_{jm}^{(1)}. \tag{A.14}$$

On $f\,\boldsymbol{S}_{jm}^{(\ell)}$, the rotation operator acts in the following way:

$$\text{rot}\,\left(f\,\boldsymbol{S}_{jm}^{(-1)}\right) = -\frac{f}{r}\boldsymbol{S}_{jm}^{(0)}, \tag{A.15}$$

$$\text{rot}\,\left(f\,\boldsymbol{S}_{jm}^{(1)}\right) = \left(\frac{d}{dr} + \frac{1}{r}\right) f\boldsymbol{S}_{jm}^{(0)}, \tag{A.16}$$

$$\text{rot}\,\left(f\,\boldsymbol{S}_{jm}^{(0)}\right) = -j(j+1)\frac{f}{r}\boldsymbol{S}_{jm}^{(-1)} - \left(\frac{d}{dr} + \frac{1}{r}\right) f\boldsymbol{S}_{jm}^{(1)}, \tag{A.17}$$

while the application of the divergence results in the following relations:

$$\text{div}\,\left(f\boldsymbol{S}_{jm}^{(-1)}\right) = \left(\frac{d}{dr} + \frac{1}{r}\right) fY_{jm}, \tag{A.18}$$

$$\text{div}\,\left(f\boldsymbol{S}_{jm}^{(1)}\right) = -j(j+1)\frac{f}{r}Y_{jm}, \tag{A.19}$$

$$\text{div}\,\left(f\boldsymbol{S}_{jm}^{(0)}\right) = 0. \tag{A.20}$$

Tensor spherical harmonics

Among several possibilities for defining *tensor spherical harmonics* (Regge & Wheeler, 1957; Backus, 1967; Zerilli, 1970; Phynney & Burridge, 1973), we will

make use of the those defined in Regge & Wheeler (1957) and employed by Martinec (2000), restricting ourselves to the second-order symmetric spherical tensors with trace. According to Zerilli (1970) there are six such tensors:

$$\begin{aligned}
\boldsymbol{Z}^{(1)}_{jm}(\Omega) &\equiv [\boldsymbol{e}_r\boldsymbol{e}_r\, Y_{jm}(\Omega)]_{\rm s}\,,\\
\boldsymbol{Z}^{(2)}_{jm}(\Omega) &\equiv [\boldsymbol{e}_r\nabla_\Omega\, Y_{jm}(\Omega)]_{\rm s}\,,\\
\boldsymbol{Z}^{(3)}_{jm}(\Omega) &\equiv [\boldsymbol{e}_r\boldsymbol{L}_\Omega\, Y_{jm}(\Omega)]_{\rm s}\,,\\
\boldsymbol{Z}^{(4)}_{jm}(\Omega) &\equiv [(\boldsymbol{L}_\Omega\nabla_\Omega + \boldsymbol{e}_r\boldsymbol{L}_\Omega)\, Y_{jm}(\Omega)]_{\rm s}\,,\\
\boldsymbol{Z}^{(5)}_{jm}(\Omega) &\equiv [(\nabla_\Omega\nabla_\Omega + \boldsymbol{L}_\Omega\boldsymbol{L}_\Omega)\, Y_{jm}(\Omega)]_{\rm s}\,,\\
\boldsymbol{Z}^{(6)}_{jm}(\Omega) &\equiv [(\nabla_\Omega\nabla_\Omega + 2\boldsymbol{e}_r\nabla_\Omega)\, Y_{jm}(\Omega)]_{\rm s}\,,
\end{aligned}$$

where the subscript 's' denotes the symmetric part of a second-order tensor $\boldsymbol{A}$ with trace, i.e. $[\boldsymbol{A}]_{\rm s} = (\boldsymbol{A} + \boldsymbol{A}^t)/2$. By introducing the tensor (or dyadic) products of spherical unit base vectors $\boldsymbol{e}_r$, $\boldsymbol{e}_\vartheta$ and $\boldsymbol{e}_\varphi$ and taking their symmetric part, we define the symmetric spherical tensor products

$$\boldsymbol{e}_{ij} \equiv [\boldsymbol{e}_i\boldsymbol{e}_j]_{\rm s} = \frac{1}{2}(\boldsymbol{e}_i\otimes\boldsymbol{e}_j + \boldsymbol{e}_j\otimes\boldsymbol{e}_i),$$

with $i,\, j = r,\, \vartheta,\, \varphi$. Using these products and the spherical operators grad $_\Omega$ and $\boldsymbol{L}_\Omega$, tensor spherical harmonics $\boldsymbol{Z}^{(\ell)}_{jm}$, $\ell = 1,\ldots,6$, can be written as follows:

$$\boldsymbol{Z}^{(1)}_{jm} = Y_{jm}\boldsymbol{e}_{rr}, \tag{A.21}$$

$$\boldsymbol{Z}^{(2)}_{jm} = E_{jm}\boldsymbol{e}_{r\vartheta} + F_{jm}\boldsymbol{e}_{r\varphi}, \tag{A.22}$$

$$\boldsymbol{Z}^{(3)}_{jm} = -F_{jm}\boldsymbol{e}_{r\vartheta} + E_{jm}\boldsymbol{e}_{r\varphi}, \tag{A.23}$$

$$\boldsymbol{Z}^{(4)}_{jm} = G_{jm}\boldsymbol{e}_{\vartheta\varphi} - H_{jm}(\boldsymbol{e}_{\vartheta\vartheta} - \boldsymbol{e}_{\varphi\varphi}), \tag{A.24}$$

$$\boldsymbol{Z}^{(5)}_{jm} = -j(j+1)Y_{jm}(\boldsymbol{e}_{\vartheta\vartheta} + \boldsymbol{e}_{\varphi\varphi}), \tag{A.25}$$

$$\boldsymbol{Z}^{(6)}_{jm} = G_{jm}(\boldsymbol{e}_{\vartheta\vartheta} - \boldsymbol{e}_{\varphi\varphi}) + 4H_{jm}\boldsymbol{e}_{\vartheta\varphi}, \tag{A.26}$$

where we defined

$$E_{jm} \equiv \frac{\partial Y_{jm}}{\partial\vartheta}, \tag{A.27}$$

$$F_{jm} \equiv \frac{1}{\sin\vartheta}\frac{\partial Y_{jm}}{\partial\varphi}, \tag{A.28}$$

$$G_{jm} \equiv \left(\frac{\partial^2}{\partial\vartheta^2} - \cot\vartheta\frac{\partial}{\partial\vartheta} - \frac{1}{\sin^2\vartheta}\frac{\partial^2}{\partial^2\varphi}\right) Y_{jm}, \tag{A.29}$$

$$H_{jm} \equiv \frac{\partial}{\partial\vartheta}\left(\frac{1}{\sin\vartheta}\frac{\partial Y_{jm}}{\partial\varphi}\right). \tag{A.30}$$

Orthogonality relations for tensor spherical harmonics are obtained by integrating over Ω the double dot product of tensors with different indices. When

$j \neq j'$, $m \neq m'$ and $\ell \neq \ell'$ we have:

$$\int_\Omega \boldsymbol{Z}_{jm}^{(\ell)} : \left(\boldsymbol{Z}_{j'm'}^{(\ell')}\right)^* \, d\Omega = 0, \tag{A.31}$$

otherwise, when $\ell = \ell'$, it holds

$$\int_\Omega \boldsymbol{Z}_{jm}^{(1)} : \left(\boldsymbol{Z}_{j'm'}^{(1)}\right)^* \, d\Omega = \delta_{jj'}\delta_{mm'}, \tag{A.32}$$

$$\int_\Omega \boldsymbol{Z}_{jm}^{(2)} : \left(\boldsymbol{Z}_{j'm'}^{(2)}\right)^* \, d\Omega = \frac{1}{2} j(j+1)\delta_{jj'}\delta_{mm'}, \tag{A.33}$$

$$\int_\Omega \boldsymbol{Z}_{jm}^{(3)} : \left(\boldsymbol{Z}_{j'm'}^{(3)}\right)^* \, d\Omega = \frac{1}{2} j(j+1)\delta_{jj'}\delta_{mm'}, \tag{A.34}$$

$$\int_\Omega \boldsymbol{Z}_{jm}^{(4)} : \left(\boldsymbol{Z}_{j'm'}^{(4)}\right)^* \, d\Omega = \frac{1}{2}(j-1)j(j+1)(j+2)\delta_{jj'}\delta_{mm'}, \tag{A.35}$$

$$\int_\Omega \boldsymbol{Z}_{jm}^{(5)} : \left(\boldsymbol{Z}_{j'm'}^{(5)}\right)^* \, d\Omega = 2j^2(j+1)^2\delta_{jj'}\delta_{mm'}, \tag{A.36}$$

$$\int_\Omega \boldsymbol{Z}_{jm}^{(6)} : \left(\boldsymbol{Z}_{j'm'}^{(6)}\right)^* \, d\Omega = 2(j-1)j(j+1)(j+2)\delta_{jj'}\delta_{mm'}. \tag{A.37}$$

Furthermore, from definitions (A.21)-(A.26), the scalar products $\boldsymbol{e}_r \cdot \boldsymbol{Z}_{jm}^{(\ell)}$ can be derived:

$$\boldsymbol{e}_r \cdot \boldsymbol{Z}_{jm}^{(1)} = \boldsymbol{S}_{jm}^{(-1)}, \tag{A.38}$$

$$\boldsymbol{e}_r \cdot \boldsymbol{Z}_{jm}^{(2)} = \frac{1}{2}\boldsymbol{S}_{jm}^{(1)}, \tag{A.39}$$

$$\boldsymbol{e}_r \cdot \boldsymbol{Z}_{jm}^{(3)} = \frac{1}{2}\boldsymbol{S}_{jm}^{(0)}, \tag{A.40}$$

$$\boldsymbol{e}_r \cdot \boldsymbol{Z}_{jm}^{(\ell)} = 0\,, \quad \ell \geq 4. \tag{A.41}$$

A.2 Double-dot products of tensor spherical harmonics

In the presence of lateral viscosity variations $\eta = \eta(r, \Omega)$, the orthogonality property (A.31) is no longer valid since the viscosity η which pre-multiplies the double dot product of tensors (eq. 3.27) cannot be taken out of the angular integration. These products must then be integrated numerically. Given the spherical dyadic $\boldsymbol{e}_{ij}$, the double dot product with itself is given by

$$\begin{aligned} \boldsymbol{e}_{ij} : \boldsymbol{e}_{ij} =& \frac{1}{2}(\boldsymbol{e}_i \otimes \boldsymbol{e}_j + \boldsymbol{e}_j \otimes \boldsymbol{e}_i) : \frac{1}{2}(\boldsymbol{e}_i \otimes \boldsymbol{e}_j + \boldsymbol{e}_j \otimes \boldsymbol{e}_i) \\ =& \frac{1}{4}(\boldsymbol{e}_i \otimes \boldsymbol{e}_j : \boldsymbol{e}_i \otimes \boldsymbol{e}_j + \boldsymbol{e}_i \otimes \boldsymbol{e}_j : \boldsymbol{e}_j \otimes \boldsymbol{e}_i \\ & + \boldsymbol{e}_j \otimes \boldsymbol{e}_i : \boldsymbol{e}_i \otimes \boldsymbol{e}_j + \boldsymbol{e}_j \otimes \boldsymbol{e}_i : \boldsymbol{e}_j \otimes \boldsymbol{e}_i) = \frac{1}{2}\,, \end{aligned} \tag{A.42}$$

if $i \neq j$. Otherwise, when $i = j$,

$$\boldsymbol{e}_{ii} : \boldsymbol{e}_{ii} = \boldsymbol{e}_i \otimes \boldsymbol{e}_i : \boldsymbol{e}_i \otimes \boldsymbol{e}_i = 1. \tag{A.43}$$

Among 21 possible combinations, using relations (A.42) and (A.43), it can be shown that only 12 of them do not vanish, namely:

$$\boldsymbol{Z}_{jm}^{(1)} : \left(\boldsymbol{Z}_{j'm'}^{(1)}\right)^* = Y_{jm}Y_{j'm'}^*, \tag{A.44}$$

$$\boldsymbol{Z}_{jm}^{(2)} : \left(\boldsymbol{Z}_{j'm'}^{(2)}\right)^* = \frac{1}{2}E_{jm}E_{j'm'}^* + \frac{1}{2}F_{jm}F_{j'm'}^*, \tag{A.45}$$

$$\boldsymbol{Z}_{jm}^{(2)} : \left(\boldsymbol{Z}_{j'm'}^{(3)}\right)^* = -\frac{1}{2}E_{jm}F_{j'm'}^* + \frac{1}{2}F_{jm}E_{j'm'}^*, \tag{A.46}$$

$$\boldsymbol{Z}_{jm}^{(3)} : \left(\boldsymbol{Z}_{j'm'}^{(2)}\right)^* = -\frac{1}{2}F_{jm}E_{j'm'}^* + \frac{1}{2}E_{jm}F_{j'm'}^*, \tag{A.47}$$

$$\boldsymbol{Z}_{jm}^{(3)} : \left(\boldsymbol{Z}_{j'm'}^{(3)}\right)^* = \frac{1}{2}F_{jm}F_{j'm'}^* + \frac{1}{2}E_{jm}E_{j'm'}^*, \tag{A.48}$$

$$\boldsymbol{Z}_{jm}^{(4)} : \left(\boldsymbol{Z}_{j'm'}^{(4)}\right)^* = -\frac{1}{2}G_{jm}G_{j'm'}^* + 2H_{jm}H_{j'm'}^*, \tag{A.49}$$

$$\boldsymbol{Z}_{jm}^{(4)} : \left(\boldsymbol{Z}_{j'm'}^{(6)}\right)^* = 2G_{jm}H_{j'm'}^* - 2H_{jm}G_{j'm'}^*, \tag{A.50}$$

$$\boldsymbol{Z}_{jm}^{(5)} : \left(\boldsymbol{Z}_{j'm'}^{(5)}\right)^* = 2j(j+1)j'(j'+1)Y_{jm}Y_{j'm'}^*, \tag{A.51}$$

$$\boldsymbol{Z}_{jm}^{(6)} : \left(\boldsymbol{Z}_{j'm'}^{(4)}\right)^* = 2H_{jm}G_{j'm'}^* - 2G_{jm}H_{j'm'}^*, \tag{A.52}$$

$$\boldsymbol{Z}_{jm}^{(6)} : \left(\boldsymbol{Z}_{j'm'}^{(6)}\right)^* = 2G_{jm}G_{j'm'}^* + 8H_{jm}H_{j'm'}^*. \tag{A.53}$$

While computing the products (A.44)-(A.53), it is useful to express the derivatives that appear in E_{jm}, F_{jm}, G_{jm} and H_{jm} in terms of functions Y_{jm}. The ϑ-derivative of scalar spherical harmonics can be expressed as follows (Varshalovich et al., 1989, Section 5.8):

$$\begin{aligned}\frac{\partial Y_{jm}}{\partial \vartheta} = E_{jm} =& \frac{1}{2}\sqrt{j(j+1)-m(m+1)}Y_{jm+1}e^{-i\varphi} \\ &- \frac{1}{2}\sqrt{j(j+1)-m(m-1)}Y_{jm-1}e^{i\varphi},\end{aligned} \tag{A.54}$$

while the φ-derivative is clearly

$$\frac{\partial Y_{jm}}{\partial \varphi} = i\,mY_{jm}. \tag{A.55}$$

Using relations (A.54) and (A.55), eqs (A.29) and (A.30) can be conveniently expressed in terms of scalar spherical harmonics as follows:

$$\begin{aligned}G_{jm} &= -\left(j(j+1) - \frac{2m^2}{\sin^2\vartheta}\right)Y_{jm} - 2\cot\vartheta E_{jm}, \\ H_{jm} &= im\left(-\frac{\cos\vartheta}{\sin^2\vartheta}Y_{jm} + \frac{1}{\sin\vartheta}E_{jm}\right).\end{aligned}$$

A.3 Transformation theorems for scalar spherical harmonics under translation of coordinate axis

We recall a few transformation theorems that apply to scalar spherical harmonics and are necessary for the construction of the eccentrically nested spheres solution developed in Chapter 5. For their detailed derivation and further discussions, we refer to Martinec & Wolf (1999, Appendix C) and to Varshalovich et al. (1989, Chapter 5).

Referring to Fig. 5.1, a point P is characterized by the position vector (r_1, Ω_1) with respect to the system $\mathcal{O}_1$ or by the position vector (r_2, Ω_2) with respect to the system $\mathcal{O}_2$. The theorems we present provide us with the expressions assumed by particular scalar spherical harmonics expressed in the $\mathcal{O}_1$ coordinate system, when $\mathcal{O}_1$ is translated by d along the z-axis. In the following, we will make use of the symbol $C^{jm}_{j_1 m_1 j_2 m_2}$ for indicating the Clebsch-Gordan coupling coefficients (Varshalovich et al., 1989, Chapter 8). The following transformation theorems hold:

$$r_2^j Y_{jm}(\Omega_2) = \sum_{j_1=0}^{j} \Gamma^{m,0}_{jj_1}(d) r_1^{j_1} Y_{j_1 m}(\Omega_1), \tag{A.56}$$

where

$$\Gamma^{m,0}_{jj_1}(d) \equiv (-1)^{j-j_1} \sqrt{\frac{(2j+1)!}{(2j_1+1)!(2j-2j_1)!}}\, C^{jm}_{j_1 m\, j-j_1\, 0} d^{j-j_1} \tag{A.57}$$

if $j \geq j_1$, otherwise $\Gamma^{m,0}_{jj_1}(d) = 0$;

$$r_2^{-j-1} Y_{jm}(\Omega_2) = \sum_{j_1=j}^{\infty} D^{m,0}_{jj_1}(d) r_1^{-j_1-1} Y_{j_1 m}(\Omega_1), \tag{A.58}$$

where

$$D^{m,0}_{jj_1}(d) \equiv (-1)^{j_1-j} \sqrt{\frac{(2j_1)!}{(2j)!(2j_1-2j)!}}\, C^{jm}_{j_1 m\, j_1-j\, 0} d^{j_1-j} \tag{A.59}$$

if $j_1 \geq j$, otherwise $D^{m,0}_{jj_1}(d) = 0$;

$$r_2^{j+2} Y_{jm}(\Omega_2) = \sum_{j_1=0}^{j+1} \Gamma^{m,2}_{jj_1}(d, r_1) r_1^{j_1} Y_{j_1 m}(\Omega_1), \tag{A.60}$$

where

$$\begin{aligned} \Gamma^{m,2}_{jj_1}(d, r_1) \equiv & (r_1^2 + d^2)\Gamma^{m,0}_{jj_1}(d) - 2d\sqrt{\frac{j_1^2 - m^2}{(2j_1-1)(2j_1+1)}}\Gamma^{m,0}_{j\, j_1-1}(d) \\ & - 2r_1^2 d\sqrt{\frac{(j_1+1)^2 - m^2}{(2j_1+1)(2j_1+3)}}\Gamma^{m,0}_{j\, j_1+1}(d) \end{aligned} \tag{A.61}$$

if $j \geq j_1 - 1$, otherwise $I^{m,2}_{jj_1}(d, r_1) = 0$;

$$r_2^{-j+1} Y_{jm}(\Omega_2) = \sum_{j_1=j-1}^{\infty} D^{m,2}_{jj_1}(d, r_1) r_1^{-j_1-1} Y_{j_1 m}(\Omega_1), \tag{A.62}$$

where

$$\begin{aligned} D^{m,2}_{jj_1}(d, r_1) \equiv & (r_1^2 + d^2) D^{m,0}_{jj_1}(d) - 2r_1^2 d \sqrt{\frac{j_1^2 - m^2}{(2j_1 - 1)(2j_1 + 1)}} D^{m,0}_{j\, j_1 - 1}(d) \\ & - 2d \sqrt{\frac{(j_1 + 1)^2 - m^2}{(2j_1 + 1)(2j_1 + 3)}} D^{m,0}_{j\, j_1 + 1}(d) \end{aligned} \tag{A.63}$$

if $j_1 \geq j - 1$, otherwise $D^{m,2}_{jj_1}(d, r_1) = 0$.

APPENDIX B

Divergence of the stress tensor

We report here without detailed derivation the expressions of the strain-rate and stress tensors in spherical coordinates, along with their spherical harmonic expansions. Once these expressions are known, it is possible to easily derive the spherical harmonic expansion of the divergence of the stress tensor that is employed in Chapter 2 to reduce the Stokes problem to a system of ordinary differential equations.

The spherical components of the strain-rate tensor $\dot{\boldsymbol{\varepsilon}}$ that we need are those obtained by taking the scalar product of the tensor itself and the spherical base vector $\boldsymbol{e}_r$:

$$\dot{\boldsymbol{\varepsilon}} \cdot \boldsymbol{e}_r = \dot{\varepsilon}_{rr}\boldsymbol{e}_r + \dot{\varepsilon}_{r\vartheta}\boldsymbol{e}_\vartheta + \dot{\varepsilon}_{r\varphi}\boldsymbol{e}_\varphi,$$

where

$$\dot{\varepsilon}_{rr} = \frac{\partial u_r}{\partial r}, \tag{B.1}$$

$$\dot{\varepsilon}_{r\vartheta} = \frac{1}{2}\left(\frac{\partial u_\vartheta}{\partial r} + \frac{1}{r}\frac{\partial u_r}{\partial \vartheta} - \frac{u_\vartheta}{r}\right), \tag{B.2}$$

$$\dot{\varepsilon}_{r\varphi} = \frac{1}{2}\left(\frac{\partial u_\varphi}{\partial r} + \frac{1}{r\sin\vartheta}\frac{\partial u_r}{\partial \varphi} - \frac{u_\varphi}{r}\right). \tag{B.3}$$

Note that eqs (B.1)-(B.3) are three of the six components that form the symmetric part of the gradient of vector $\boldsymbol{u}$.

Using vector spherical harmonics (see Appendix A.1) for the flow vector $\boldsymbol{u}$, the expansions of the single components read as

$$u_r = \sum_{jm} u_{jm} Y_{jm}, \tag{B.4}$$

$$u_\vartheta = \sum_{jm}\left(v_{jm}\frac{\partial Y_{jm}}{\partial \vartheta} - \frac{1}{\sin\vartheta}w_{jm}\frac{\partial Y_{jm}}{\partial \varphi}\right), \tag{B.5}$$

$$u_\varphi = \sum_{jm} \left(\frac{1}{\sin\vartheta} v_{jm} \frac{\partial Y_{jm}}{\partial \varphi} + w_{jm} \frac{\partial Y_{jm}}{\partial \vartheta} \right). \tag{B.6}$$

Upon inserting eqs (B.4)-(B.6) into eqs (B.1)-(B.3), we readily obtain the expansions for the components of the strain-rate tensor:

$$\dot{\varepsilon}_{rr} = \sum_{jm} \frac{du_{jm}}{dr} Y_{jm}, \tag{B.7}$$

$$\dot{\varepsilon}_{r\vartheta} = \frac{1}{2} \sum_{jm} \left[\left(\frac{dv_{jm}}{dr} - \frac{v_{jm}}{r} + \frac{u_{jm}}{r} \right) \frac{\partial Y_{jm}}{\partial \vartheta} + \left(\frac{w_{jm}}{r} - \frac{dw_{jm}}{dr} \right) \frac{1}{\sin\vartheta} \frac{\partial Y_{jm}}{\partial \varphi} \right], \tag{B.8}$$

$$\dot{\varepsilon}_{r\varphi} = \frac{1}{2} \sum_{jm} \left[\left(\frac{dv_{jm}}{dr} - \frac{v_{jm}}{r} + \frac{u_{jm}}{r} \right) \frac{1}{\sin\vartheta} \frac{\partial Y_{jm}}{\partial \varphi} + \left(\frac{dw_{jm}}{dr} - \frac{w_{jm}}{r} \right) \frac{\partial Y_{jm}}{\partial \vartheta} \right]. \tag{B.9}$$

Expanding also the pressure p in scalar spherical harmonics, the coefficients for the components of the stress tensor (2.22) are readily obtained using eqs (B.7)-(B.9).

In order to write the Stokes equation (2.21) in spherical coordinates, an expression for the divergence of the stress tensor is necessary. After writing $\operatorname{div} \boldsymbol{\tau}$ in the following way:

$$\operatorname{div} \boldsymbol{\tau} = -\operatorname{grad} p + \eta(\nabla^2 \boldsymbol{u} + \operatorname{grad} \operatorname{div} \boldsymbol{u}) + \frac{d\eta}{dr} \boldsymbol{e}_r \cdot (\operatorname{grad} \boldsymbol{u} + \operatorname{grad}^t \boldsymbol{u}),$$

it can be shown that the spherical components of $\operatorname{div} \boldsymbol{\tau}$ are:

$$(\operatorname{div} \boldsymbol{\tau})_r = \frac{\partial \tau_{rr}}{\partial r} - 2\eta \frac{\partial \dot{\varepsilon}_{rr}}{\partial r} + \eta (\nabla^2 \boldsymbol{u})_r + \eta \frac{\partial}{\partial r} (\operatorname{div} \boldsymbol{u}), \tag{B.10}$$

$$(\operatorname{div} \boldsymbol{\tau})_\vartheta = \frac{\partial \tau_{r\vartheta}}{\partial r} - 2\eta \frac{\partial \dot{\varepsilon}_{r\vartheta}}{\partial r} - \frac{1}{r} \frac{\partial p}{\partial \vartheta} + \eta (\nabla^2 \boldsymbol{u})_\vartheta + \frac{\eta}{r} \frac{\partial}{\partial \vartheta} (\operatorname{div} \boldsymbol{u}), \tag{B.11}$$

$$(\operatorname{div} \boldsymbol{\tau})_\varphi = \frac{\partial \tau_{r\varphi}}{\partial r} - 2\eta \frac{\partial \dot{\varepsilon}_{r\varphi}}{\partial r} - \frac{1}{r \sin\vartheta} \frac{\partial p}{\partial \varphi} + \eta (\nabla^2 \boldsymbol{u})_\varphi + \frac{\eta}{r \sin\vartheta} \frac{\partial}{\partial \varphi} (\operatorname{div} \boldsymbol{u}), \tag{B.12}$$

where the components of the spherical Laplacian are given by

$$(\nabla^2 \boldsymbol{u})_r = \nabla^2 u_r - \frac{2}{r^2} u_r - \frac{2}{r^2} \frac{\partial u_\vartheta}{\partial \vartheta} - \frac{2}{r^2} \cot\vartheta u_\vartheta - \frac{2}{r^2 \sin\vartheta} \frac{\partial u_\varphi}{\partial \varphi},$$

$$(\nabla^2 \boldsymbol{u})_\vartheta = \nabla^2 u_\vartheta - \frac{1}{r^2 \sin\vartheta} u_\vartheta + \frac{2}{r^2} \frac{\partial u_r}{\partial \vartheta} - \frac{2}{r^2} \frac{\cot\vartheta}{\sin\vartheta} \frac{\partial u_\varphi}{\partial \varphi},$$

$$(\nabla^2 \boldsymbol{u})_\varphi = \nabla^2 u_\varphi - \frac{1}{r^2 \sin\vartheta} u_\varphi + \frac{2}{r^2 \sin\vartheta} \frac{\partial u_r}{\partial \varphi} - \frac{2}{r^2} \cot\vartheta \frac{\partial u_\vartheta}{\partial \varphi}.$$

Upon inserting eqs (B.1)-(B.9) into eqs (B.10)-(B.12), we obtain the expansions required in Chapter 2 for reducing the original partial differential equations to a system of ordinary differential equations.

APPENDIX C

Integrals over finite elements

The definite integrals over finite elements that are employed in the parameterization of the radial part of the field variables can be easily computed analytically. All the necessary combinations of k and $k+1$ are:

$$
\begin{aligned}
I^{(1)}_{k,k} &= \int_{r_k}^{r_{k+1}} \frac{d\psi_k}{dr}\frac{d\psi_k}{dr} r^2 dr = \frac{1}{3h_k}(r^2_{k+1} + r_{k+1}r_k + r^2_k),\\
I^{(1)}_{k,k+1} &= \int_{r_k}^{r_{k+1}} \frac{d\psi_k}{dr}\frac{d\psi_{k+1}}{dr} r^2 dr = -I^{(1)}_{k,k} = I^{(1)}_{k+1,k},\\
I^{(1)}_{k+1,k+1} &= \int_{r_k}^{r_{k+1}} \frac{d\psi_{k+1}}{dr}\frac{d\psi_{k+1}}{dr} r^2 dr = I^{(1)}_{k,k},\\
I^{(2)}_{k,k} &= \int_{r_k}^{r_{k+1}} \psi_k \frac{d\psi_k}{dr} r^2 dr = -\frac{1}{12}(r^2_{k+1} + 2r_{k+1}r_k + 2r^2_k),\\
I^{(2)}_{k,k+1} &= \int_{r_k}^{r_{k+1}} \psi_k \frac{d\psi_{k+1}}{dr} r^2 dr = -I^{(2)}_{k,k},\\
I^{(2)}_{k+1,k+1} &= \int_{r_k}^{r_{k+1}} \psi_{k+1} \frac{d\psi_{k+1}}{dr} r^2 dr = -\frac{1}{12}(3r^2_{k+1} + 2r_{k+1}r_k + r^2_k),\\
I^{(3)}_{k,k} &= \int_{r_k}^{r_{k+1}} \psi_k \frac{d\psi_k}{dr} r dr = -\frac{1}{6}(r_{k+1} + 2r_k),\\
I^{(3)}_{k,k+1} &= \int_{r_k}^{r_{k+1}} \psi_k \frac{d\psi_{k+1}}{dr} r dr = -I^{(3)}_{k,k},\\
I^{(3)}_{k+1,k} &= \int_{r_k}^{r_{k+1}} \psi_{k+1} \frac{d\psi_k}{dr} r dr = -I^{(3)}_{k+1,k+1},\\
I^{(3)}_{k+1,k+1} &= \int_{r_k}^{r_{k+1}} \psi_{k+1} \frac{d\psi_{k+1}}{dr} r dr = \frac{1}{6}(2r_{k+1} + r_k),
\end{aligned}
$$

$$I^{(4)}_{k,k} = \int_{r_k}^{r_{k+1}} \psi_k \psi_k r^2 dr = \frac{h_k}{30}(r^2_{k+1} + 3r_{k+1}r_k + 6r^2_k),$$

$$I^{(4)}_{k,k+1} = \int_{r_k}^{r_{k+1}} \psi_k \psi_{k+1} r^2 dr = \frac{h_k}{60}(3r^2_{k+1} + 4r_{k+1}r_k + 3r^2_k),$$

$$I^{(4)}_{k+1,k+1} = \int_{r_{k+1}}^{r_{k+1}} \psi_k \psi_{k+1} r^2 dr = \frac{h_k}{30}(6r^2_{k+1} + 3r_{k+1}r_k + r^2_k),$$

$$I^{(5)}_{k,k} = \int_{r_k}^{r_{k+1}} \psi_k \psi_k r dr = \frac{h_k}{12}(r_{k+1} + 3r_k),$$

$$I^{(5)}_{k,k+1} = \int_{r_k}^{r_{k+1}} \psi_k \psi_{k+1} r dr = \frac{h_k}{12}(r_{k+1} + r_k),$$

$$I^{(5)}_{k+1,k+1} = \int_{r_k}^{r_{k+1}} \psi_k \psi_{k+1} r dr = \frac{h_k}{12}(3r_{k+1} + r_k),$$

$$I^{(6)}_{k,k} = \int_{r_k}^{r_{k+1}} \psi_k \psi_k dr = \frac{h_k}{3},$$

$$I^{(6)}_{k,k+1} = \int_{r_k}^{r_{k+1}} \psi_k \psi_{k+1} dr = \frac{1}{2} I^{(6)}_{k,k},$$

$$I^{(6)}_{k+1,k+1} = \int_{r_k}^{r_{k+1}} \psi_{k+1} \psi_{k+1} dr = I^{(6)}_{k,k},$$

$$I^{(7)}_{k,k} = \int_{r_k}^{r_{k+1}} \frac{1}{r} \psi_k \psi_k dr = \frac{1}{h_k}\left(\frac{r^2_{k+1}}{h_k} \log \frac{r_{k+1}}{r_k} - 2r_{k+1} + \frac{1}{2}(r_{k+1} + r_k)\right),$$

$$I^{(7)}_{k,k+1} = \int_{r_k}^{r_{k+1}} \frac{1}{r} \psi_k \psi_{k+1} dr = \frac{1}{h_k}\left(-\frac{r_{k+1}r_k}{h_k} \log \frac{r_{k+1}}{r_k} + \frac{1}{2}(r_{k+1} + r_k)\right),$$

$$I^{(7)}_{k+1,k+1} = \int_{r_k}^{r_{k+1}} \frac{1}{r} \psi_{k+1} \psi_{k+1} dr = \frac{1}{h_k}\left(\frac{r^2_k}{h_k} \log \frac{r_{k+1}}{r_k} - 2r_k + \frac{1}{2}(r_{k+1} + r_k)\right),$$

$$K^{(1)}_k = \int_{r_k}^{r_{k+1}} \frac{d\psi_k}{dr} r^2 dr = -\frac{1}{3}(r^2_{k+1} + r_k r_{k+1} + r^2_k),$$

$$K^{(1)}_{k+1} = \int_{r_k}^{r_{k+1}} \frac{d\psi_{k+1}}{dr} r^2 dr = -K^{(1)}_k,$$

$$K^{(2)}_k = \int_{r_k}^{r_{k+1}} \psi_k r dr = \frac{h_k}{6}(r_{k+1} + 2r_k),$$

$$K^{(2)}_{k+1} = \int_{r_k}^{r_{k+1}} \psi_{k+1} r dr = \frac{h_k}{6}(2r_{k+1} + r_k),$$

$$K^{(3)}_k = \int_{r_k}^{r_{k+1}} \psi_k r^2 dr = \frac{h_k}{12}(r^2_{k+1} + 2r_{k+1}r_k + 3r^2_k),$$

$$K^{(3)}_{k+1} = \int_{r_k}^{r_{k+1}} \psi_{k+1} r^2 dr = \frac{h_k}{12}(3r^2_{k+1} + 2r_{k+1}r_k + r^2_k),$$

Bibliography

Backus, G., 1967, Converting vector and tensor equations to scalar equations in spherical coordinates, *Geophys, J. R. astr. Soc.*, **13**, 71–101.

Barrett, R., Berry, M., Chan, T., Demmel, J., Donato, J., Dongarra, J., Eijkhout, V., Pozo, R., Romine, C., & Van der Vorst, H., 1994, *Templates for the solution of linear systems: Building blocks for iterative methods, 2nd Edition*, SIAM, Philadelphia, PA.

Baumgardner, J., 1985, Three dimensional treatment of convection flow in the Earth's mantle, *J. Stat. Phys.*, **39**, 501–511.

Becker, T. W. & Boschi, L., 2002, A comparison of tomographic and geodynamic mantle models, *Geochem. Geophys. Geosyst.*, **3**, 10.129/2001GC000168.

Becker, T. W. & O'Connell, R., 2001, Predicting plate velocities with mantle circulation models, *Geochem. Geophys. Geosyst.*, **2**, 2001GC000171.

Benzi, M., 2002, Preconditioning techniques for large linear systems: a survey, *J. Comput. Phys.*, **182**, 418–477.

Billen, M. I. & Gurnis, M., 2003, Comparison of dynamic flow models for the Central Aleutian and Tonga-Kermadec subduction zones, *Geochem. Geophys. Geosyst.*, **4**(4), 10.129/2001GC000295.

Boschi, L. & Dziewonski, A., 1999, "High" and "low" resolution images of the Earth's mantle - Implications of different approaches to tomographic modeling, *J. Geophys. Res.*, **104**, 25567–25594.

Busse, F., 1989, Fundamentals of thermal convection, in *Mantle Convection, Plate Tectonics and Global Dynamics*, edited by W. Peltier, pp. 23–95, Gordon and Breach, Newark, N.J.

Čadek, O. & Fleitout, L., 1999, A global geoid model with imposed plate velocities and partial layering, *J. Geophys. Res.*, **104**(B12), 29055–29075.

Čadek, O. & Fleitout, L., 2003, Effect of lateral viscosity variations in the top 300 km on the geoid and dynamic topography, *Geophys. J. Int.*, **152**, 566–580.

Čadek, O., Martinec, Z., & Matyska, C., 1992, Spectral variational approach to the non-Newtonian Stokes problem in a spherical shell, *Comput. Phys. Commun.*, **71**, 56–70.

Čadek, O., Ricard, Y., Martinec, Z., & Matyska, C., 1993, Comparison between Newtonian and non-Newtonian flow driven by internal loads, *Geophys. J. Int.*, **112**, 103–114.

Chandrasekhar, S., 1968, *Hydrodynamic and hydromagnetic stability*, The international series of monographs on physics, Clarendon Press, Oxford.

Christensen, U., 1984, Convection with pressure- and temperature-dependent non-Newtonian rheology, *Geophys, J. R. astr. Soc.*, **77**, 343–384.

Christensen, U. & Harder, H., 1991, 3-D convection with variable viscosity, *Geophys. J. Int.*, **104**, 213–226.

Corrieu, V., Thoraval, C., & Ricard, Y., 1995, Mantle dynamics and geoid Green functions, *Geophys. J. Int.*, **120**, 516–523.

Dahlen, F., 1974, On the static deformation of an Earth model with a fluid core, *Geophys, J. R. astr. Soc.*, **36**, 461–485.

Davies, G., 1981, Regional compensation of subducting lithosphere: Effects on geoid, gravity and topography from a preliminary model, *Earth Plant. Sci. Lett.*, **54**, 431–444.

Defraigne, P., Dehant, V., & Wahr, J., 1996, Internal loading of an inhomogeneous compressible Earth with phase boundaries, *Geophys. J. Int.*, **125**, 173–197.

Dehant, V. & Wahr, J., 1991, The response of a compressible, non-homogeneous Earth to internal loading: Theory, *J. Geomag. Geoelectr.*, **43**, 157–178.

Duncan, R. & Richards, M., 1991, Hotspots, mantle plumes, flood basalts and true polar wander, *Rev. Geophys.*, **29**, 31–50.

D'Yakonov, B., 1959, The diffraction of electromagnetic waves by a sphere located in a half-space, *Izv. Earth Sci.*, **11**, 1120–1125.

Dziewonski, A. M. & Anderson, D. L., 1981, Preliminary reference Earth model, *Phys. Earth Planet. Inter.*, **25**, 297–356.

Dziewonski, A. M., Hager, B., & O'Connell, R., 1977, Large-scale heterogeneities in the lower mantle, *J. Geophys. Res.*, **82**, 239–255.

Everett, M. & Schultz, A., 1995, Geomagnetic induction in eccentrically nested spheres, *Phys. Earth Planet. Inter.*, **92**, 189–198.

Farnetani, C. & Richards, M., 1994, Numerical investigations of mantle plume initiation model for flood basalt events, *J. Geophys. Res.*, **99**, 13813–13833.

Förste, C., Flechter, F., Schmidt, R., Knig, R., Meyer, U., Stubenvoll, R., Rothacher, M., Barthelmes, F., Neumayer, K., Biancale, R., Bruinsma, S., & Lemoine, J.-M., 2006, A mean global gravity field model from the combination of satellite mission and altimetry/gravimetry surface gravity data, *Geophys. Res. Abs.*, **8**(03462).

Forte, A., Peltier, W., Dziewonski, A., & Woodward, R., 1993, Dynamic surface topography: A new interpretation based opon mantle flow models derived from seismic tomography, *Geophys. Res. Lett.*, **20**, 1665–1666.

Forte, A. M. & Mitrovica, J. X., 1996, New inferences of mantle viscosity from joint inversion of long-wavelength mantle convection and postglacial rebound data, *Geophys. Res. Lett.*, **23**(10), 1147–1150.

Forte, A. M. & Peltier, R., 1991, Viscous flow models of global geophysical observables. 1. Forward problems, *J. Geophys. Res.*, **96**(B12), 20131–20159.

Gantmacher, F., 1990, *Matrix theory*, American Mathematical Society, 2nd edn.

Gelfand, I. & Fomin, S., 1963, *Calculus of variations*, Prentice-Hall Inc., Englewood Cliffs, N.J.

Gilbert, F. & Backus, G. E., 1966, Propagator matrices in elastic wave and vibration problems, *Geophys.*, **31**(2), 326–332.

Griffiths, R. & Campbell, I., 1990, Stirring and structure in mantle plumes, *Earth. Planet. Sci. Lett.*, **99**, 66–78.

Gurnis, M., 1990, Bounds on global dynamic topography from phanerozoic flooding of continental platfroms, *Nature*, **344**, 754–756.

Hager, B. H., 1984, Subducted slabs and the geoid: Constraints on mantle rheology and flow, *J. Geophys. Res.*, **89**, 6003–6016.

Hager, B. H. & Clayton, R., 1989, Constraints on the structure of mantle convection using seismic observations, flow models, and the geoid, in *Mantle Convection, Plate Tectonics and Global Dynamics*, edited by W. Peltier, pp. 657–763, Gordon and Breach, Newark, N.J.

Harder, H., 1991, Numerical simulation of thermal convection with Maxwellian viscoelasticity, *J. Non-Newt. Fluid Mech.*, **39**, 67–88.

Heiskanen, W. & Moritz, H., 1967, *Physical geodesy*, Freeman & co., San Francisco.

Hill, R., 1991, Starting plumes and continental breakup, *Earth. Planet. Sci. Lett.*, **104**, 398–416.

Hofmann, H., 1997, Mantle geochemistry: the message from oceanic volcanism, *Nature*, **385**, 219–229.

Hughes, T. J., 1987, *The finite element method*, Prentice-Hall Inc., Englewood Cliffs, N.J.

Jarvis, G. & McKenzie, D., 1980, Convection in a compressible fluid with infinite Prandtl number, *J. Fluid Mech.*, **96**, 515–583.

Karato, S., 1993, Importance of anelasticity in the interpretation of seismic tomography, *Geophys. Res. Lett.*, **20**, 1623–1626.

Karato, S. & Wu, P., 1993, Rheology of the upper mantle: a synthesis, *Nature*, **260**, 771–778.

Kaufmann, G. & Lambeck, K., 2000, Mantle dynamics, postglacial rebound and the radial viscosity profile, *Phys. Earth Planet. Inter.*, **121**, 301–324.

Kennett, B., 2001, *The seismic wavefield*, Cambridge University Press, Cambridge (UK).

Kido, M. & Seno, T., 1994, Dynamic topography compared with residual depth anomalies in oceans and implications for age-depth curves, *Geophys. Res. Lett.*, **21**, 717–720.

King, S., 1995, Models of mantle viscosity, in *Mineral physics and cristallography: a handbook of physical constants*, edited by T. Ahrens, pp. 227–236, AGU, Washington.

King, S. & Masters, G., 1992, An inversion for radial viscosity structure using mantle tomography, *Geophys. Res. Lett.*, **19**, 1551–1554.

King, S., Raefsky, A., & Hager, B., 1990, Conman - vectorizing a finite-element code for incompressible 2-dimensional convection in the Earth's mantle, *Phys. Earth Planet. Inter.*, **59**, 195–207.

King, S. D., 1995, Radial models of mantle viscosity: results from a genetic algorithm, *Geophys. J. Int.*, **122**, 725–734.

King, S. D., 2002, Geoid and topography over subduction zones: The effect of phase transitions, *J. Geophys. Res.*, **107**(B1).

King, S. D. & Hager, B. H., 1994, Subducted slabs and the geoid, 1. Numerical experiments with temperature dependent viscosities, *J. Geophys. Res.*, **99**, 19,843–19,852.

Křižek, M. & Neittaanmäki, P., 1990, *Finite element approximation of variational problems and applications*, Longman Scientific & Technical, J. Wiley, New York.

Landau, L. & Lifshitz, E., 1987, *Fluid mechanics*, vol. 6 of Course of theoretical physics, Butterworth Heinemann, Oxford, 2nd edn.

Le Stunff, Y. & Ricard, Y., 1995, Topography and geoid due to lithospheric mass anomalies, *Geophys. J. Int.*, **122**, 982–990.

Le Stunff, Y. & Ricard, Y., 1997, Partial advection of equidensity surfaces: A solution for the dynamic topography problem?, *J. Geophys. Res.*, **102**(B11), 24655–24667.

Lithgow-Bertelloni, C. & Richards, M., 1995, Cenozoic plate driving forces, *Geophys. Res. Lett.*, **22**, 1317–1320.

Lithgow-Bertelloni, C. & Silver, P. G., 1998, Dynamic topography, plate driving forces and the African superswell, *Nature*, **395**, 269–272.

Malevsky, A. & Yuen, D., 1992, Strongly chaotic non-Newtonian mantle convection, *Geophys. Astrophys. Fluid Dynamics*, **65**, 149–171.

Marquart, G. & Schmeling, H., 2004, A dynamic model for the Iceland plume and the North Atlantic based on tomography and gravity data, *Geophys. J. Int.*, **159**, 40–52.

Martinec, Z., 1989, Program to calculate the spectral harmonic expansion coefficients of the two scalar fields product, *Comput. Phys. Commun.*, **54**, 63–79.

Martinec, Z., 1999, Spectral-finite element approach to three-dimensional electromagnetic induction in a spherical Earth, *Geophys. J. Int.*, **136**, 229–250.

Martinec, Z., 2000, Spectral-finite element approach to three-dimensional viscoelastic relaxation in a spherical Earth, *Geophys. J. Int.*, **142**, 117–141.

Martinec, Z. & Wolf, D., 1999, Gravitational viscoelastic relaxation of eccentrically nested spheres, *Geophys. J. Int.*, **138**, 45–66.

Matyska, C., 1996, Variational principles for the momentum equation of mantle convection with Newtonian and power-law rheologies, *Geophys. J. Int.*, **126**, 281–286.

McKenzie, D., 1977, Surface deformation, gravity anomalies and convection, *Geophys. J. R. Astron. Soc.*, **48**, 211–238.

Montagner, J.-P., 1994, Can seismology tell us anything about convection in the mantle?, *Rev. Geophys.*, **32**, 115–137.

Montelli, R., Nolet, G., Dahlen, F., Masters, G., Engdahl, E., & Hung, S., 2003, Finite-frequency tomography reveals a variety of plumes in the mantle, *Science*, **303**(5656), 338–343.

Moresi, L. & Gurnis, M., 1996, Constraints on the lateral strength of slabs from three-dimensional dynamic flow models, *Earth. Planet. Sci. Lett.*, **138**, 15–28.

Moresi, L. & Solomatov, V., 1995, Numerical investigations of 2D convection with extremely large viscosity contrasts, *Phys. Fluids*, **7**, 2154–2162.

Morgan, J. W., 1970, Convection plumes in the lower mantle, *Nature*, **230**, 422–43.

Moucha, R., Forte, A., Mitrovica, J., & Daradich, A., 2007, Lateral variations in mantle rheology: implications for convection related surface observables and inferred viscosity models, *Geophys. J. Int.*, **169**, 113–135.

Nataf, H., Nakanishi, I., & Anderson, D., 1986, Measurements of mantle wave velocities and inversion for lateral heterogeneities and anisotropy, III, inversion, *J. Geophys. Res.*, **91**, 7261–7307.

Nataf, H.-C. & Ricard, Y., 1996, 3SMAC: an a priori tomographic model of the upper mantle based on geophysical modeling, *Phys. Earth Planet. Inter.*, **95**, 101–122.

O'Connell, R., Gable, C., & Hager, B., 1991, Toroidal-poloidal partitioning of lithospheric plate motion, in *Glacial isostasy, sea level and mantle rheology*, edited by R. Sabadini & E. Boschi, pp. 513–535, Kluwer Acad., Norwell, Mass.

Panasyuk, S. & Hager, B. H., 2000, Inversion for mantle viscosity profiles constrained by dynamic topography and the geoid, and their estimated errors, *Geophys. J. Int.*, **143**, 821–836.

Pari, G. & Peltier, R. W., 1998, Global surface heat flux anomalies from seismic tomography-based models of mantle flow: Implications for mantle convection, *J. Geophys. Res.*, **103**(B10), 23743–23780.

Pekeris, C. L., 1935, Thermal convection in the interior of the Earth, *Mont. Not. R. Astron. Soc. Geophys. Suppl.*, pp. 343–367.

Phynney, R. & Burridge, R., 1973, Representation of elastic-gravitational excitation of a spherical Earth model by generalized spherical harmonics, *Geophys, J. R. astr. Soc.*, **34**, 451–487.

Press, W., Teukolsky, S., Vetterling, W., & Flannery, B., 1992, *Numerical recipes in Fortran. The art of scientific computing*, Cambridge University Press, Cambridge.

Ranalli, G., 1995, *Rheology of the earth*, Chapman & Hall, London.

Regge, T. & Wheeler, J., 1957, Stability of a Schwarzschild singularity, *Phys. Rev.*, **108**, 1063–1069.

Renardy, M. & Rogers, R. C., 1993, *An introduction to partial differential equations*, Texts in Applied Mathematics, Springer.

Ribe, N. M., 1992, The dynamics of thin shells with variable viscosity and the origin of toroidal flow in the mantle, *Geophys. J. Int.*, **110**, 537–552.

Ricard, Y. & Vigny, C., 1989, Mantle dynamics with induced plate tectonics, *J. Geophys. Res.*, **94**(B12), 17543–17559.

Ricard, Y., Fleitout, L., & Froidevaux, C., 1984, Geoid heights and lithospheric stresses for a dynamic Earth, *Ann. Geophys.*, **2**(3), 267–286.

Ricard, Y., Richards, M., Lithgow-Bertelloni, C., & Stunff, Y. L., 1993, A geodynamic model of mantle density heterogeneity, *J. Geophys. Res.*, **98**(B12), 21895–21909.

Richards, M. A. & Hager, B. H., 1984, Geoid anomalies in a dynamic Earth, *J. Geophys. Res.*, **89**(B7), 5987–6002.

Richards, M. A. & Hager, B. H., 1989, Effects of lateral viscosity variations on long-wavelength geoid anomalies and topography, *J. Geophys. Res.*, **94**(B8), 10299–10313.

Ritsema, J. & van Heijst, H. J., 2000, Seismic imaging of structural heterogeneity in Earth's mantle: Evidence for large scale mantle flow, *Sci. Progr.*, **93**, 243–259.

Ritsema, J., van Heijst, H. J., & Woodhouse, J. H., 1999, Complex shear wave velocity structure imaged beneath Africa and Iceland, *Nature*, **286**, 1925–1928.

Runcorn, S., 1964, Satellite gravity measurements and a laminar viscous flow model of the Earth's mantle, *J. Geophys. Res.*, **69**(20), 4389–4394.

Runcorn, S., 1967, Flow in the mantle inferred from low degree harmonics of the geopotential, *Geophys. J. R. astr. Soc.*, **14**, 375–384.

Saad, Y., 2003, *Iterative methods for sparse linear systems*, SIAM.

Schmid, D. & Podladchikov, Y., 2003, Analytical solutions for deformable elliptical inclusions in general shear, *Geophys. J. Int.*, **155**, 269–288.

Schubert, G., Turcotte, D. L., & Olson, P., 2001, *Mantle convection in the Earth and planets*, Cambridge University Press, Cambridge.

Sleep, N., 1990, Hot spots and mantle plumes: some phenomenology, *J. Geophys. Res.*, **95**, 6715–6736.

Steinberger, B., 2000, Slabs in the lower mantle - Results of dynamic modelling compared with tomographic images and the geoid, *Phys. Earth Planet. Inter.*, **118**, 241–257.

Stoer, J. & Bulirsch, R., 2002, *Introduction to numerical analysis*, Texts in Applied Mathematics, Springer Verlag, New York.

Su, W. & Dziewonski, A., 1997, Simultaneous inversion for 3-D variations in shear and bulk velocity in the mantle, *Phys. Earth Planet. Inter.*, **100**, 135–156.

Tan, E., Choi, E., Thoutireddy, P., Gurnis, M., & Aivazis, M., 2006, Geoframework: Coupling multiple models of mantle convection within a computational framework, *Geochem. Geophys. Geosyst.*, **7**(Q06001), 10.1029/2005GC001155.

Tapley, B., Bettadpur, S., Watkins, M., & Reigber, C., 2004, The gravity recovery and climate experiment: Mission overview and early results, *Geophys. Res. Lett.*, **131**(9), 1–8, 10.129/2004GL019920.

Thoraval, C. & Richards, M. A., 1997, The geoid constraint in global geodynamics: viscosity structure, mantle heterogeneity models and boundary conditions, *Geophys. J. Int.*, **131**, 1–8.

Thoraval, C., Machetel, P., & Cazenave, A., 1994, Influence of mantle compressibility and ocean warping on dynamical models of geoid, *Geophys. J. Int.*, **117**, 566–573.

Thoraval, C., Machetel, P., & Cazenave, A., 1995, Locally layered convection inferred from dynamic models of the Earth's mantle, *Nature*, **375**, 777–780.

To, A., Romanowicz, B., Capdeville, Y., & Takeuchi, N., 2005, 3D effects of sharp boundaries at the borders of the African and Pacific superplumes: observation and modeling, *Earth. Planet. Sci. Lett.*, **233**, 137–153.

Tosi, N. & Martinec, Z., 2007, Semi-analytical solution for viscous Stokes flow in two eccentrically nested spheres, *Geophys. J. Int.*, pp. 1–16, 10.1111/j.1365-246X.2007.03482.x.

Trubitsyn, V., Baranov, A., Evseev, A., & Trubitsyn, A., 2006, Exact analytical solutions of the Stokes equation for testing the equations of mantle convection with a variable viscosity, *Izv. Earth Sci.*, **42**(7), 537–545.

van der Hilst, R., Widiyantoro, S., & Engdahl, E., 1997, Evidence of deep mantle circulation from global tomography, *Nature*, **386**, 578–584.

van der Wal, W., Schotman, H., & Vermeersen, L., 2004, Geoid heights due to a crustal low viscosity zone in glacial isostatic adjustment modeling: A sensityivity analysis for GOCE, *Geophys. Res. Lett .*, **31**, 10.1029/2003GL019139.

Varshalovich, D., Moskalev, A., & Khersonskii, V., 1989, *Quantum theory of angular momentum*, World Scientific Publ., Singapore.

Velimsky, J. & Martinec, Z., 2005, Time-domain, spherical harmonic-finite element approach to transient three-dimensional geomagnetic induction in a spherical heterogeneous Earth, *Geophys. J. Int.*, **161**, 81–101.

Walker, J. S., 1988, *Fourier analysis*, Oxford University Press, Oxford.

Wen, L. & Anderson, D. L., 1997, Present-day plate motion constraint on mantle rheology and convection, *J. Geophys. Res.*, **102**(B11), 24639–24653.

Woodhouse, J. & Dziewonski, A., 1984, Mapping the upper mantle: Three dimensional modelling of Earth structure by inversion of seismic waveform, *J. Geophys. Res.*, **89**, 5953–5986.

Zerilli, F. J., 1970, Tensor harmonics in canonical form for gravitational radiation and other applications, *J. Math. Phys.*, **111**(7), 2203–2208.

Zhang, S. & Christensen, U., 1993, Some effects of lateral viscosity variations on geoid and surface velocities induced by density anomalies in the mantle, *Geophys. J. Int.*, **114**, 531–547.

Zhong, S., 1996, Analytic solutions for Stokes' flow with lateral variations in viscosity, *Geophys. J. Int.*, **124**, 18–28.

Zhong, S. & Davies, G. F., 1999, Effects of plates and slab viscosities on the geoid, *Earth. Planet. Sci. Lett.*, **170**, 487–496.

Zhong, S., Zuber, M., Moresi, L., & Gurnis, M., 2000, Role of temperature-dependent viscosity and surface plates in spherical shell models of mantle convection, *J. Geophys. Res.*, **105**, 11063–11082.

Acknowledgments

First and foremost, I am deeply grateful to my supervisor Prof. Zdeněk Martinec for his friendship, his constant encouragement and immense patience in advising and helping me during these years.

I am thankful to my colleagues at GFZ, Veronika, Detlef, Ingo, Jan, Kevin, Rico and Volker, for making me feel welcome every day from the very first I started working in Potsdam. A special thank goes to Volker for letting all of us pleasantly join every day and drink his excellent - though German - coffee, and to Kevin for his regular tours to my office offering coffee, food as much as psychological support and for his great help with the proofreading of my English manuscripts.

I am also thankful to my colleagues at the department of geophysics in Prague, Hana, Marie, Jakub, Lada, Ondřej the 1st, Ondřej the 3rd and Radek, for making pleasant my numerous visits to the department. I reserve special thanks to Jakub for his willingness to help me with every necessity.

I want also to thank all the Italian friends that visited me so many times since I was away from Milan. Seeing you in Berlin has made it a lot of easier to accept that we can no longer meet as often as before.

My sisters and parents have been a constant presence during these years far from home, despite the distance that separated us. Thank you so much for your enormous support.

Elena, you deserve my deepest thank for your infinite patience in tolerating all the ups and downs of my life as a PhD student and for your constant loving encouragement. With the birth of Sofia, year 2007 has been without any doubt the most important of my whole life. Thank you and Sofia for making me so happy.